Experimental Study on Multi-Hole Biodiesel Pulsed Spray in Cross Airflow

by

Queenie So

A thesis
presented to the University of Waterloo
in fulfillment of the
thesis requirement for the degree of
Master of Applied Science
in
Mechanical Engineering

Waterloo, Ontario, Canada, 2013

I hereby declare that I am the sole author of this thesis. This is a true copy of the thesis, including any required final revisions, as accepted by my examiners.

I understand that my thesis may be made electronically available to the public.

Abstract

Many fuel spray characterization studies to date have been conducted in quiescent environments with single-hole fuel injectors. However, in actuality, multi-hole injectors spray into direct injection engine cylinders where significant air swirling and tumbling exist to promote fuel atomization and air-fuel mixing, which result in more efficient combustion. For this reason, researchers have begun developing correlations for fuel sprays where a jet of air acts perpendicularly to the fuel spray, also known as a cross airflow or crossflow, so as to more realistically predict fuel spray characteristics in direct injection engines. Accordingly, there is a need for a foundation of experimental data reflecting the specific conditions of fuel spray in cross airflow which can then be used for model validation and future engine design and development. In this study, fuel sprays are characterized with a commercial 8-hole fuel injector in a wind tunnel enclosure capable of cross airflows upwards of 200m/s. Particle image velocimetry was used to measure air velocities and capture pulsed spray events of biodiesel, diesel, and biodiesel-diesel blend fuels. Spray images were processed and analyzed in LaVision's DaVis and in MATLAB to calculate spray penetration length and axis deflection angle under varying cross airflow velocities, fuel injection pressures, and fuel types. Results show that strong cross airflows can decrease spray penetration by up to 44% and deflect the spray axis by up to 10.5° when compared to the same spray in a quiescent environment. Additional experiments reveal that biodiesel experiences slower spray progression when compared with diesel, resulting in shorter spray penetrations in the early phase of the spray development (up to 0.7ms after the start of injection, or ASOI). The angle between the fuel injector axis and the air jet axis plays an important role in determining the resultant spray characteristics. This angle should be considered in future correlations.

Acknowledgements

Thanks to the Ontario Research Fund and General Motors USA for supporting and giving me the opportunity to work on this project. I would like to thank my supervisor, Dr. Xianguo Li, for his guidance throughout this experience.

I would like to thank Alan Rickard at Rothsay Biodiesel for his generous biodiesel donation and Mike Idsinga at Volkswagen Waterloo for the continuous help with the common rail fuel system. I also thank Xianghui Xiao and his team at the Argonne National Laboratory for imaging the internal geometry of our diesel fuel injector.

This project would not have been possible without the dedication of the MME staff: Jason Benninger, Andy Barber, Jim Merli, Rick Forgett, Karl Janzen, Charlie Boyle, Marc Kuntz, Rob Kaptein, Rob Kramer, Fred Bakker, and Jorge Cruz. I thank all of them for their tireless efforts and helping our team meet our absurd deadlines.

Furthermore, I would like to thank all the members of our research group with whom I had the privilege to work and interact. I have made some truly amazing friends here and I am forever indebted to everyone who encouraged and motivated me over the course of my project. A special thank you goes out to Aaron Pereira, Kaushik Saha, Dr. Yi Ren, and Dr. Yongxin Wang for sharing their expertise and helping me see this project to completion.

Last but not least, I am grateful for my parents, Pauline, Brian, and all my friends and family for their love and confidence throughout my journey in graduate school.

Table of Contents

List of Tables

List of Figures

Nomenclature

List of Symbols

Latin

D	Diameter
P	Pressure
q	Momentum flux ratio, $q = (\rho_j V_j^2 / \rho_a V_a^2)$
S	Spray penetration length
t	Time
T	Temperature
V	Velocity

Greek

Δ	Difference ($\Delta P = P_{inj} - P_a$)
ρ	Density
θ	Spray cone angle
ω	Jet-Jet azimuthal angle
φ	Jet axis angle
μ	Dynamic vicosity
ϵ	Perspective error vector ($\epsilon = \left(\frac{\Delta z}{\Delta x} \cdot tan\Theta_x, \frac{\Delta z}{\Delta y} \cdot tan\Theta_y\right)$)

Subscripts

a	Ambient air/gas
b	Break-up
eq	Equivalent
f	Relative to fuel
inj	Relative to injection
j	Relative to a fuel jet
o	Relative to injector orifice
x	Parallel to cross-flow direction
y	Perpendicular to cross-flow direction, parallel to injector axis
z	Perpendicular to cross-flow direction, perpendicular to injector axis

Abbreviations

DI	Direct Injection
CRDI	Common-Rail Diesel Injection
TDI	Turbocharged Direct Injection

Chapter 1

Introduction

1.1 Motivation

As government regulations for fuel economy and pollutant emissions become increasingly stringent, the subject of direct injection engines, especially in combination with the use of alternative fuels, has expanded drastically in today's transportation industry. The efficiency of combustion and the amount of emissions produced in direct injection engines are strongly associated with fuel spray processes. Researchers today have access to a variety of cutting edge software that can model fuel spray processes [1, 2, 3, 4, 5]. However, many of these models are based on and validated with experimental data conducted in quiescent ambient conditions [6, 7, 8, 9]. These conditions are unrealistic of internal combustion engines. Therefore, it is beneficial to study fuel spray processes under more realistic conditions in order to improve the accuracy and predictive capabilities of existing fuel spray models. This chapter will provide brief background information, objectives, scope, and outline of this thesis.

1.2 Background information

Liquid fuel cannot be burned efficiently in combustion chambers [10]. The chemical bonds of the liquid need to be broken to form the proper compounds for combustion [11]. This is accomplished by heating the droplets to vaporization. In other words, breakup of the bulk liquid fuel is necessary for increasing the specific surface area of the fuel, which enhances the rate of evaporation and creates a combustible air-fuel mixture [12]. The more complete the combustion process is, the higher the volumetric heat release rates and fuel efficiency and lower the pollutant emissions.

For example, in a direct injection (DI) diesel engine, liquid fuel is injected at very high injection pressures and through small injector orifices into a high temperature environment. The liquid fuel is injected into the combustion chamber towards the end of the compression stroke, at which point the pressure and temperature in the cylinder may reach 10MPa and 1000K [13]. Simultaneously, air in the cylinder undergoes significant swirling and tumbling motion, which affects the heat transfer and air-fuel mixing inside the cylinder. This is vastly different from a direct injection gasoline (GDI) engine. The injection pressures experienced in a DI diesel engine are typically an order of magnitude higher than those in GDI engines. Also, the design of a DI diesel engine cylinder, such as the piston bowl shape and injector location, is very different from the GDI engine cylinder (Figure 1.1). This is because different fuel injection strategies are required to ensure the optimal conditions for combustion in the respective cylinders.

Figure 1.2 illustrates the effect of an air swirl on a single diesel fuel spray plume. For the purpose of this study, an airflow of constant velocity perpendicular to the direction of the spray injection (or crossflow) can be used to simplify the phenomenon found inside a combustion chamber. This type of interaction is easier to reproduce and to analyze and therefore can provide some insight on spray-swirl interaction.

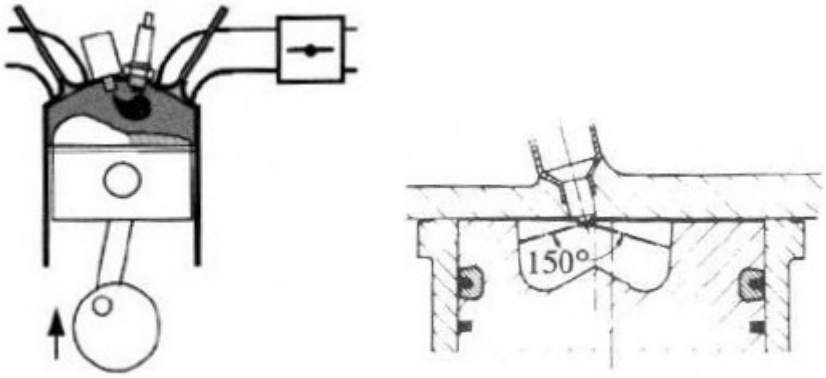

(a) GDI cylinder [14] (b) DI diesel cylinder [13]

Figure 1.1: Design of a) direct injection gasoline cylinder and b) direct injection diesel cylinder

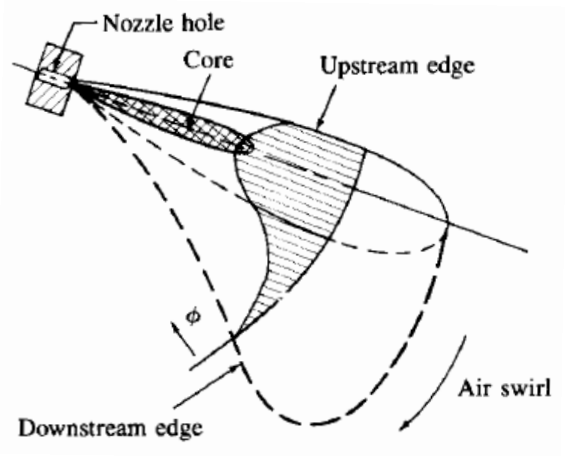

Figure 1.2: Swirl motion interaction with diesel fuel spray. [13]

1.3 Objectives and Methodology

The objective of this thesis is to investigate multi-hole fuel macroscopic spray characteristics in an air crossflow. Also, experiments are conducted with both commercial and in-house fuels in an attempt to develop fuels with properties that produce optimized spray characteristics. To achieve these objectives, an experimental apparatus capable of crossflow velocities up to 230m/s was constructed. The apparatus is also equipped with a piezoelectric diesel fuel injector that injects at pressures up to 180MPa, typical of a 3rd generation

Bosch common-rail diesel injection (CRDI) fuel system. Visualization and measurements are done with a LaVision PIV system. The results can be beneficial not only for model validation and spray simulations of diesel engines, but also DI gasoline engines and gas turbines.

1.4 Scope and Outline

Chapter 2 discusses the existing literature on fuel spray characteristics in both quiescent and non-quiescent ambient conditions. Chapter 3 provides a detailed description of the experimental apparatus, experimental conditions, and measurement techniques involved. Chapter 4 discusses the data post-processing performed and the experimental uncertainties encountered. Chapter 5 provides the analysis and discussion of the experimental results. Lastly, all conclusions and recommendations are provided in Chapter 6.

Chapter 2

Literature Review

Many parameters play a role in fuel spray development, including, but not limited to, ambient gas conditions, injector geometry, and fuel properties. [15, 16] Due to the many variables that affect spray behaviour and the difficulty of experimenting with realistic engine conditions, there is no consensus in the literature as to which correlations best predicts spray characteristics. This chapter will define the spray characteristics pertaining to this thesis and review their existing correlations in literature.

Spray characteristics can be classified as microscopic or macroscopic. Microscopic spray characteristics generally focus on aspects like liquid break-up mechanisms, droplet diameter, and droplet velocity. Macroscopic spray characteristics describe the interaction between the injector's internal flow parameters (e.g. injection pressure, injector orifice diameter) and the ambient conditions (e.g. temperature and pressure). [17, 18] The macroscopic characteristics relating to the overall shape and size of the spray are often referred to as characteristics of the spray structure or spray geometry (Figure 2.1).

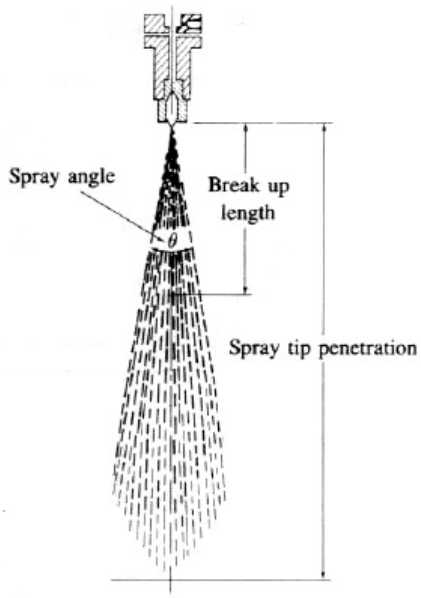

Figure 2.1: Spray Geometry Characteristics [19]

2.1 Sprays in Quiescent Environments

2.1.1 Liquid Jet Break-Up

In the context of liquid sprays in quiescent conditions, there are four regimes by which liquid jets break up into droplets. These regimes are commonly referred to as the Rayleigh regime, the first and second wind-induced regimes, and the atomization regime. [20] The regimes are characterized by the different combinations of liquid inertia, surface tension, and aerodynamic forces acting on the jet, as shown in Figure 2.2. [21]

The Rayleigh regime describes low velocity flows where an unbroken jet length is formed at the exit of the injector hole. At a certain length downstream of the injector hole, droplets are formed due to the instability in the liquid column caused by oscillations as a result of liquid inertia and surface tension forces. The liquid column length at which the droplets pinch off is called the break-up length and the diameter of the droplets here are larger than that of the injector hole. Increasing the velocity of the liquid jet results in a decrease of the break-up length. At sufficiently higher velocities, aerodynamic forces come into

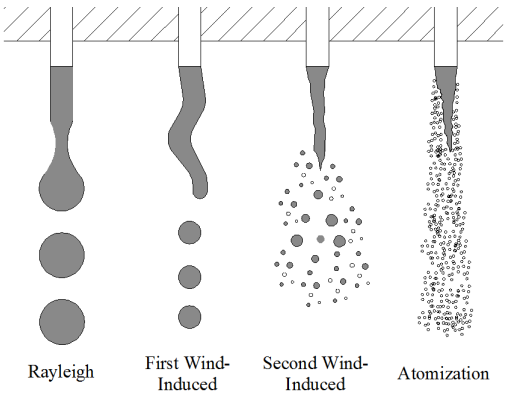

Figure 2.2: Schematic description of jet break-up regimes [22]

play and the size of the droplets decrease to the order of the injector hole diameter. This kind of break-up is characterized under the first wind-induced regime. Further increasing the velocity results in jet break-up due to a combination of turbulent surface waves in the liquid column and the aerodynamic forces between the gas and liquid phases. In this second wind-induced regime, the droplets begin breaking off of the liquid jet surface while the core of the jet remains intact. At this point, the droplets formed are smaller in diameter than the injector holes.

In the atomization break-up regime found in high-velocity engine fuel sprays, the liquid readily breaks up into a conical spray of microscopic liquid droplets immediately after leaving the injector. [13] This is also called the primary break-up region, as the droplets become entrained in the surrounding air. An intact core length still exists despite the fact that atomization begins near the injector tip. As the droplets interact with the aerodynamic forces from the surroundings, they continue to break up into progressively smaller droplets in the secondary break-up region. Here, the droplets spread throughout the ambient gas and reduce in velocity. In the hot environment of an engine cylinder, these droplets evaporate to create a fuel vapour-air mixture that is suitable for combustion. All the fuel sprays encountered in this study fall under the atomization regime.

2.1.2 Spray Characteristics

The Society of Automotive Engineers released a standard, SAE-J2715, that outlines the recommended practices for fuel injector spray and measurement and characterization. This standard applies strictly to direct injection gasoline sprays. No equivalent standard was found for diesel sprays. However, the Engine Combustion Network (ECN) follows spray characterization developed by Naber and Siebers [23]. The ECN methods are used by many experimental and computational researchers in the engine combustion community across the world. As Naber and Siebers describe, the evaluation of the spray angle and

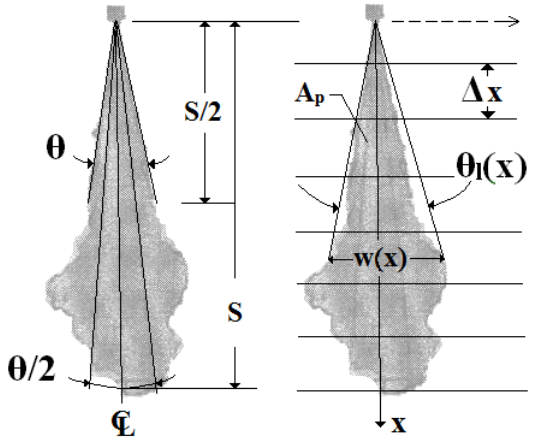

Figure 2.3: Spray geometry characteristics in quiescence. Adapted from [23]

spray penetration length is an iterative process, as they depend on each other. The spray angle is defined as $\theta = tan^{-1}\left(\frac{A_{p,S/2}}{(S/2)^2}\right)$, where $A_{p,S/2}$ refers to the projected spray area of the upstream half of the spray in an image. The penetration is defined as "the distance along the spray axis to a location where 1/2 of the pixels on an arc of $\theta/2$ centered on a spray axis are dark", as shown in Figure 2.3 [23].

Spray Angle

The spray angle is a measure of the air entrainment of the spray or the quality of atomization [24]. As the spray angle increases, so does the exposure of spray droplets to the

surrounding gas, leading to higher rates of heat and mass transfer and ultimately better combustion [25, 26]. Conversely, a decrease in spray angle results in a reduction of air entrainment in the spray [27]. Wakuri et al. [28] experimented with non-vaporizing diesel sprays using injection pressures between 40MPa and 75MPa, injector orifice diameters between 0.31mm and 0.38mm, and ambient gas densities up to 22kg/m^3. They found that spray angle is influenced by ambient gas density, injector orifice diameter, injection velocity, and time. Hiroyasu and Arai [19] looked at non-vaporizing diesel sprays with injection pressures up to 80MPa and ambient gas density up to 30kg/m^3. They expressed spray angle in terms of gas-fuel density ratio and injector orifice aspect ratio. They found that at high enough injection velocities, the spray angle reaches a maximum value and remains almost constant thereafter.

Modern CRDI systems can inject at pressures up to 200MPa. Gupta et al. [29] also experimented with non-vaporizing diesel fuel sprays, but used a CRDI system and injection pressures up to 120MPa. They discovered that the spray angle decreased significantly over the early period of the main injection in CRDI systems with multi-injection strategies, resulting in a large spread of values. They reasoned that the high injection pressure and shorter injection duration cause the spray angle to become transient because air entrainment and dispersion continue even after the main injection. Consequently, using an averaged spray angle value in the previous correlations would not be representative of the spray angle. Gupta developed a correlation for spray angle that depends on the fuel density, injection pressure, and time elapsed from start of injection.

Spray Penetration

The spray penetration is defined as the "maximum distance the spray reaches when injected into stagnant air, i.e. the maximum distance between the tip and the root of the spray" [30]. In DI diesel engines, fuel spray penetration in the engine cylinder influences the air utilization and fuel-air mixing rates [13]. Under-penetration means that the air around the periphery of the combustion chamber is not being efficiently used, resulting in less power output. Conversely, over-penetration causes fuel impingement against cylinder walls, producing more unburned and partially burnt chemical species.

Dent et al. [31] derived an equation for spray penetration that accounts for the ambient temperature into which the fuel is injected. They validated this correlation against experimental data from various test conditions, including cold bomb (room temperature), hot bomb (∼800K), and engine experiments (∼1000K). Hay and Jones [32] recommended the Dent correlation for ambient gas pressures of under 10MPa. Over 10MPa, the correlation tends to over-predict the penetration length, which implies that higher ambient gas pressures may actually decrease penetration lengths. Based on experimental data covering a wide range of conditions and applying jet disintegration theory, Hiroyasu and Arai [19] developed equations for spray penetration lengths before and after the break-up time, t_b, the time it takes a spray to reach the break-up length. Mancaruso et al. [33] found that Hiroyasu's break-up time is always 20% less than the break-up time developed by Naber and Siebers using a CRDI system.

Gupta et al. [29] investigated the effect of injection parameters on multi-hole injector diesel spray characteristics with a CRDI system and found that the Hiroyasu correlation consistently over-predicted the spray penetration lengths. Gupta proposed their own equation; however, the injector orifice diameter was not taken into account. Mancaruso et al. [33] attributed the over-prediction of the Hiroyasu spray penetration to the high injection pressure of common rail systems. They presented a modified Hiroyasu correlation that reduces the effect of the injection pressure. When comparing solenoid and piezoelectric injectors in a CRDI system, Oki et al. [34] found that although piezoelectric injectors have shorter response times, they produce longer penetration lengths.

2.1.3 Multi-Jet Sprays

Multi-hole injectors found in diesel engines typically have 6 to 8 orifices positioned radially around the injector axis (Figure 2.4a). The injector axis is typically angled between 12°-16° from the cylinder head. [35] The individual holes or orifices are also tilted at small angles from the plane orthogonal to the injector axis (Figure 2.4b).

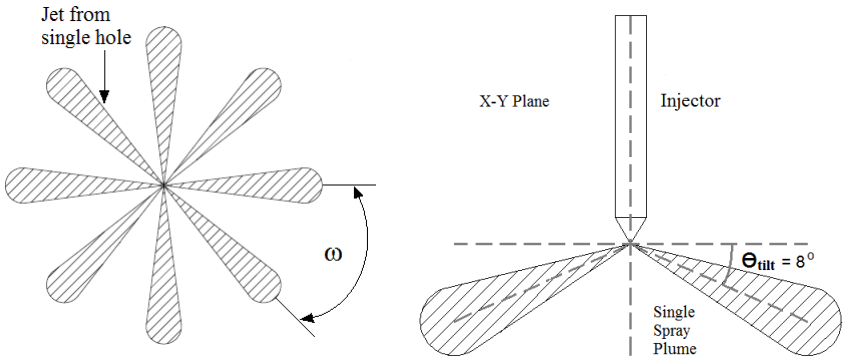

(a) Jets from multiple holes (b) Orifice tilt angle

Figure 2.4: Multi-hole injector in crossflow

Jet-Jet Interaction

Interactions between jets in a multi-hole injector affect the fuel-air mixing processes in the DI diesel engine. Increasing the number of injector holes results in an increase of mixing, but only to an optimal number of holes. [35] Beyond this number, jet-jet interaction may negatively affect the fuel-air mixing. For multi-hole injectors, geometrical parameters such as hole diameter and orifice configuration start to influence the spray formation. [36] Abraham et al. found that the orifice tilt is proportional to the fuel-air mixing inside an engine cylinder. [35] As the orifice tilt decreases and the jets spread further apart from each other, the mixing rate increases. They also concluded that jet-jet interactions are dependent on the azimuthal angle between jet centerlines, ω. Since diesel injector holes are usually equiangular from each other, ω determines the number of holes in the injector. In an experimental study, Malbec and Bruneaux [37] found that the maximum air entrainment level and total mass of entrained air remains similar regardless of the number of holes in the injector. However, there exists a delay in reaching the maximum air entrainment level when the injector has a high number of holes (i.e. 12). In other words, the transient behaviour of air-fuel mixing is affected by the number of holes in the injector.

2.2 Sprays in Crossflow

A spray in crossflow can be defined as a liquid jet of mean velocity, V_j, issuing perpendicularly into a transverse gas stream of velocity V_a. Fric and Roskho [38] explained that near the jet exit, several vortical structures can be found. Among these structures are the jet shear layer, wake structures, and counter-rotating vortex pairs (CVP) as illustrated in Figure 2.5. CVP formation in the near field (close to injection) affects the spray by producing lifting forces that alter the spray trajectory, enhancing secondary break-up, and decreasing the mean fuel droplet diameter [39, 40]. The CVP flow structure dominates the cross-section of the jet, particularly beyond 5-10 diameters downstream of injection [41]. Leong et al. [42] also reported that these vortices may account for the stripping of drops from the downstream side of the liquid column. Disintegration and atomization of the liquid jet col-

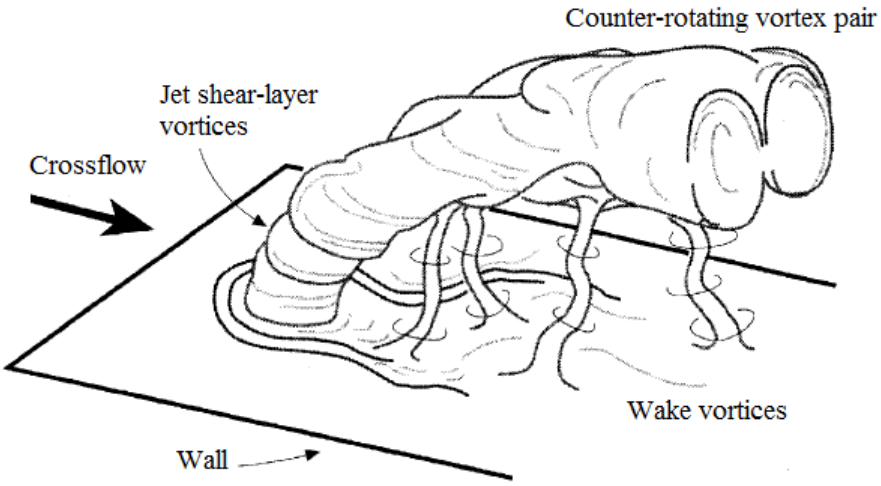

Figure 2.5: Types of vortical structures associated with transverse jet in crossflow [38]

umn becomes more complex in a crossflow. In the context of internal combustion engines, these complexities relate to cylinder wall impingement and jet interaction (in a multi-hole injector), making them important to characterize and understand. According to Mashayek and Ashgriz, a liquid jet in crossflow can be expressed using $C = f\left(\frac{\rho_j}{\rho_a}, \frac{V_j}{V_a}, \frac{\rho_a V_a^2 D}{\sigma}, \frac{\rho_a V_a D}{\mu_j}\right)$. This expression uses non-dimensionalized fluid properties of the liquid and gas components, including the velocity, density, surface tension, and dynamic viscosity of the liquid component (V_j, ρ_j, σ, μ_j) and the velocity, density, and viscosity of the gas component

$(V_g,\ \rho_a,\ \mu_a)$.

In above equation can be simplified to $C = f(q, We_a, Re_j)$, where $q = (\rho_j V_j^2/\rho_a V_a^2)$ is the liquid momentum to gas phase momentum ratio, $We_a = (\rho_a V_a^2 D)/\sigma$ is the gas Weber number based on orifice diameter and liquid surface tension, and $Re_j = \rho_j V_j D/\sigma_j$ is the jet Reynolds number. As the momentum flux ratio, q, increases, the fuel jet is expected to bend less and penetrate further. This parameter is important in determining the jet trajectory. The Weber number is the ratio of the gas inertia to the liquid surface tension, which is important when looking at jet break-up and droplet sizes. Finally, the Reynolds number characterizes the droplet size and velocity, the break-up locations, and the level of turbulence in the system.

2.2.1 Liquid Jet Break-Up

The break-up mechanisms in a crossflow are very different compared to a break-up in quiescent environments. Sedarsky illustrates in Figure 2.6 primary, column, and secondary break-up mechanisms that can be encountered [43]. Primary break-up refers to the result of surface stripping from the liquid column. Column break-up occurs when the intact liquid jet column breaks down into droplets at the column break-up length. Secondary break-up refers to the subsequent break-up of those droplets formed at column break-up length. In primary break-up, aerodynamic forces from the crossflow overcome surface tension in

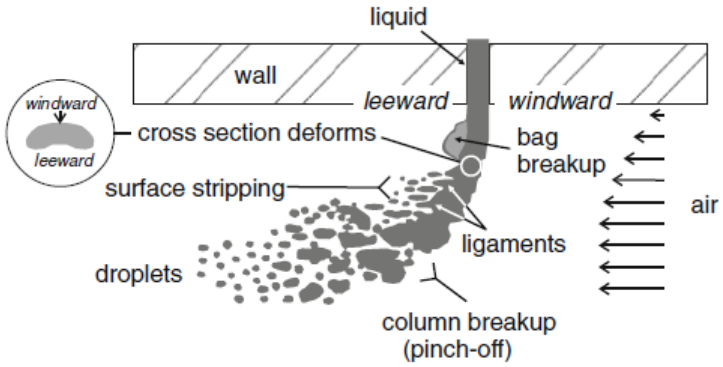

Figure 2.6: Schematic of break-up processes of liquid jet in air crossflow [43]

the liquid column, causing instability and deformation in the liquid-to-gas interface [44].

Sallam et al. [45] experimented with round nonturbulent jets and found that the structures formed in primary break-up depend on the Weber number, varying from bag-like structures at low Weber numbers ($4 < \text{We} < 30$) to ligaments shearing off the liquid column at high Weber numbers ($\text{We} > 100$).

When the liquid column bends with the force of the crossflow, a point of curvature is created. It is near this point of curvature where the intact liquid column breaks up into large individual fragments [46]. This mechanism of break-up is called column break-up. Sallam et al. [45] and Wu et al. [47] found that the length at which the column break-up occurs, x_b, correlates to the liquid jet orifice diameter. For nonturbulent jets, $x_b = 8D$, while for turbulent jets, $x_b = 5D$. The mechanism for liquid column break-up again depends on the Weber number. For low Weber numbers, the instability and break-up of the liquid column is a result of waves forming due to Rayleigh/Taylor instability. At high Weber numbers, the liquid column breaks as a result of deformation and loss of liquid mass due to shear break-up (up to 90% of the original mass) [48]. Finally, the droplets formed from both primary and column break-up undergo secondary break-up from the same forces that created them [46]. The Weber number is also used to predict the break-up regimes of droplets in a gas crossflow, although the transition Weber number is not consistent in literature. Oscillations and distortions begin at low Weber numbers, followed by bag break-up, shear break-up, and a fourth regime called the catastrohpic break-up [20]. Desantes et al. [49] found that the Sauter-Mean Diameter (SMD) of the droplets increases with the axial coordinate, implying that large droplets are being influenced to a bigger extent than small droplets.

2.2.2 Spray Characteristics

Relatively few studies to date have fundamentally characterized spray geometry in crossflows. Depending on the type of imaging performed and the method of analysis used, the resulting characteristics can vary widely. [48] Figure 2.7a and 2.7b illustrate the characteristics discussed in this thesis.

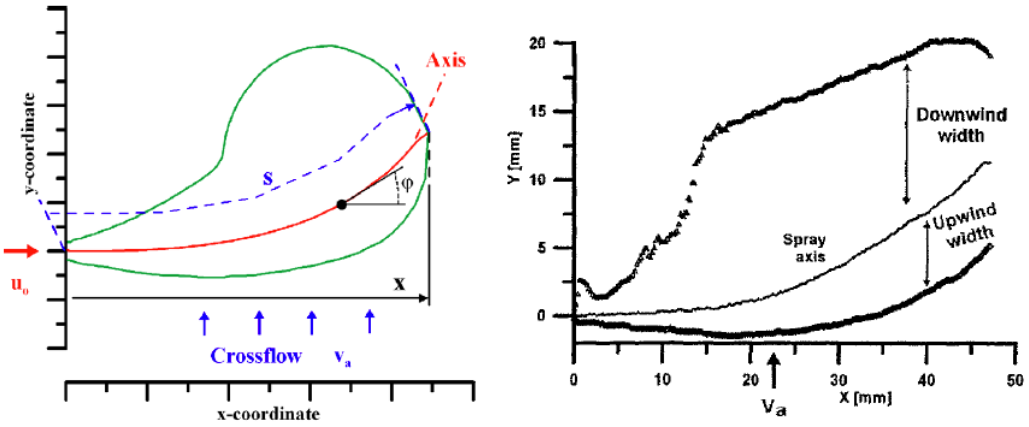

(a) Axis deflection angle, φ [49] (b) Spray axis and spray width [39]

Figure 2.7: Spray characteristics in crossflow

Jet Axis Angle and Spray Width

Spray angles of crossflow sprays cannot be easily measured due to the deformation and break-up. Thus, many researchers have characterized a different feature called the axis deflection angle. Desantes et al. experimented with turbulent gas jets and defined the axis deflection angle as the angle between the jet axis and the x-direction, denoted as φ and illustrated in Figure 2.7a. Similarly, Lee et al. [50] defined the axis deflection angle as the angle between the bent jet and injector axis. Variations in the name of this angle include "jet inclination angle" [51] and "jet axis angle" [49]. Desantes et al. also calculated for spray axis deflection, defined as the amount in the x- and y-directions by which the centerline spray axis of a quiescent spray is shifted. In that study, they found that axis deflection behaves similar in diesel sprays and in gas jets, and is related to the spray cone angle of the same spray in the free spray condition.

Spray or droplet dispersion can provide information regarding the width of the spray. Inamura et al. measured the variation of mass flux distributions in the x-y plane as shown in Figure 2.7a to visualize droplet dispersion [52]. In the region where droplet dispersion is dominated by the droplet momentum ($L/d \leq 60$), they found that the mass flux distribution can be approximated by a standard normal function. Stenzler et al. generated spray penetration curves based on the upper spray boundary (downwind side)

[53]. This method, however, does not provide any indication of spray widths. Desantes et al. experimented with a single hole of a multi-hole injector using crossflow velocities of up to 8.4m/s and diesel injection pressures up to 110MPa [49]. They indicated that the upwind spray width remains unchanged, but the downwind width increases with crossflow velocity. Becker and Hassa [54] derived a correlation for momentum flux ratios in the range of 1-26, Weber numbers of 360-2120, and characteristic length (x/D) of 2-18, to calculate the half-width lateral dispersion in the y-z plane. It was found that the momentum flux ratio has nearly negligible effect on lateral dispersion.

Jet Trajectory and Spray Penetration

In a gas crossflow, the momentum of the crossflow is partly expended to bend the liquid jet and partly to disintegrate the liquids. Therefore, a jet trajectory and spray penetration can be defined. The jet trajectory refers to the path of the liquid column up until the column break-up location. Once droplets break off the liquid column, they are considered independent of the liquid column and interact solely with the crossflow gas. Mashayek and Ashgriz [48] assumed that droplets have an initial velocity equal to the fuel jet velocity and zero velocity in the cross flow direction, which they consider a fair assumption for high momemtum ratio jet flows such as DI diesel sprays. Wu et al. [47] developed a correlation based on the drag force acting on the liquid jet in the direction of the crossflow to calculate for jet trajectory. One year later, Wu et al. [55] extended their previous correlation to account for the full spray penetration. Becker and Hassa [54] experimented with sprays in crossflow at elevated ambient pressures typical of gas turbine applications. Stenzler et al. [53] suggest that spray penetration in crossflow is not only a function of the momentum ratio, q, but also the Weber number and liquid viscosity. This is because it has been shown that Weber numbers affect the average droplet size and that viscosities influence the drag force on the liquid column. They found that increased Weber numbers and liquid viscosities decreased the spray penetration and increased the extent of the liquid column bending. Similarly, Desantes [49] concluded that higher crossflow velocities correspond to lower spray penetration and is a result of the gas entrainment process. These correlations are summarized in Table 2.1.

Table 2.1: Correlations of spray penetration in crossflow from past studies

Author(s)	**Conditions**	**Spray Penetration Correlation**
Mashayek & Ashgriz [48]	Droplet evaporation, droplet interaction neglected	$y = Cq^{\alpha} ln(1 + \beta x)$
	C,α, β: Conditional constants	$\beta \approx 1$
Wu et al. [55]	$54 < We_a < 217$	
	$5.3 < q < 59.1$	$\frac{y}{D} = 4.3 \cdot q^{0.33} \left(\frac{x}{D}\right)^{0.33}$
	Ma=0.2,0.3,0.4	
Becker & Hassa [54]	$90 < We_a < 2120$	
	$1 < q < 40$	$\frac{y}{D} = 1.48 \cdot q^{0.42} \cdot ln\left(1 + 3.56 \cdot \frac{x}{D}\right)$
	$2 < x/D < 22$	
Inamura et al. [51]	$50m/s < V_a < 140m/s$	$\frac{y}{D} = (1.18 + 0.24D) \cdot q^{0.36}$
	$10.6 < We_a < 158.1$	$\times ln\left(1 + (1.56 + 0.48D)\frac{x}{D}\right)$
Stenzler et al. [53]	$0.9 < We_a < 164.3$	
	$10.8m/s < V_a < 118.7m/s$	$\frac{y}{D} = 3.354q^{0.442} \left(\frac{x}{D}\right)^{0.390}$
	$3.06 \times 10^{-4} < \mu < 10.02 \times 10^{-4}$	$\times We^{-0.088} \left(\frac{\mu_l}{\mu_{H_2O}}\right)^{0.027}$
	q=9,4,18	

2.2.3 Atomized Sprays in Crossflow

Until now, the reviewed literature studied liquid jets that do not fall in the atomization break-up regime. DI diesel sprays are almost always in the atomization regime, which means the intact liquid core is short and droplets form promptly at the injector nozzle exit. For high momentum flux ratio jet flows, such as in DI diesel sprays, jet bending may not be significant. [48] Ghosh and Hunt [56] experimented with pressure-atomized sprays in crossflow and observed that the motion after the liquid jet break-up length can be divided into different regions, depending on the relative velocity of the crossflow and the

spray. As shown in Figure 2.8, for weak crossflows ($V_a/V_j \lesssim 0.1$), the air jet created by the

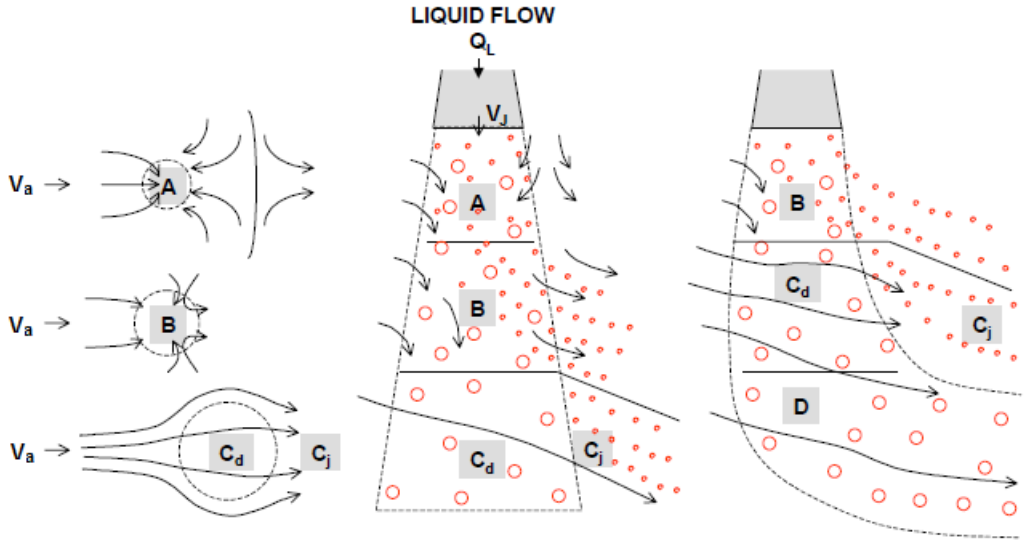

Figure 2.8: Regions of interaction of spray jet in crossflow [56]

co-flowing gas stream induces a vertical air velocity that entrains air from the surrounding into the spray region. In region B, the entrainment continues while the small droplets are deflected and dispersed downstream of the crossflow. In region C, all of the crossflow air passes through the spray and carries with it the small droplets. At higher crossflows, ($V_a/V_j \gtrsim 0.1$), the spray behaves as in a fluid jet in crossflow, where a CVP appears. At even higher crossflows ($V_a/V_j > 0.3$), the crossflow is too fast to be entrained. As a result, region A of the flow zones disappears and a new, region D, appears, in which even the larger spray droplets are deflected and dispersed. Ghosh and Hunt analyzed the effect of crossflows in the context of agricultural sprays where the crossflow is induced by the movement of a tractor and therefore did not consider crossflows where $V_a/V_j > 1$.

Leong et al. [42] looked at sprays in crossflows that were atomized by means of an airblast, essentially atomizing the liquid directly at the injector outlet. They noticed that with an increased air-to-liquid ratio (ALR), or momentum flux ratio, resulted in decreased jet bending, increased jet penetration, increased air entrainment, and increased spray dispersion. Since the spray is atomized near the injector outlet, the droplets formed are promptly dispersed. Figure 2.9 shows the effect of ALR on the spray geometry of a liquid jet in a crossflow.

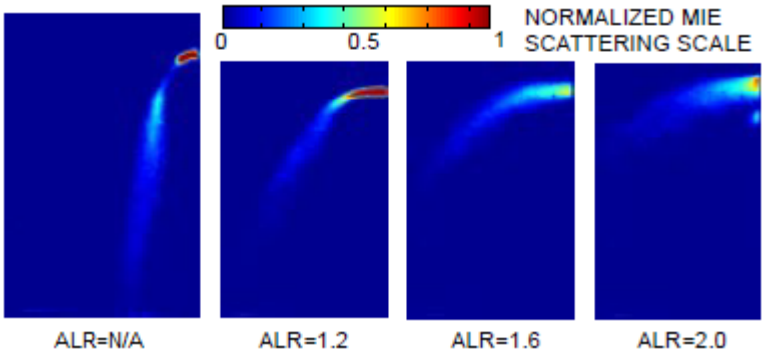

Figure 2.9: Effect of airblast pressure drop on spray geometry of liquid jet in crossflow (Increasing airblast pressure and air-to-liquid ratio (ALR) from left to right) [42]

2.2.4 Multi-Jet Sprays

The interaction of multiple jets with one another and with the crossflow influences the overall spray's accessibility to oxygen, level of turbulence, fuel mixing, and combustion [57]. Whereas jet-to-jet interaction in quiescent air depends primarily on the separation distance between jets, the interaction of multiple jets in crossflow depends on the geometrical orientation of the jets, the momentum flux ratio, as well as the separation distance [57]. Ajersch et al. [58] observed that for a row of jets in crossflow, jet penetration decreases and entrainment increases as the separation increases. On the other hand, Holdeman [59] concluded that closely spaced holes inhibited penetration. It has also been found that two jets impinging on each other behave similarly to a jet impinging on a wall when the jet injection pressures are closely matched [25].

Jet-Air Interaction

Holdeman et al. [59] investigated the mixing characteristics of a row of cold gaseous jets injecting into a rectangular duct with a 15m/s hot airstream and concluded that the jet-to-air momentum flux ratio was the most important variable influencing the jet penetration and mixing. Kim et al. [60] looked at the effect of canted injection angles on the spray characteristics of a single liquid jet in subsonic crossflows and concluded that the injection angle affects the liquid column break-up length. They found that for injectors pointed

downstream, the liquid column penetrates further and its break-up length is dominated by the injection velocity. They reason that the shear stress from the crossflow acting on the liquid column decreases and therefore atomization is degraded. For sprays are injected in reverse (i.e. against the airflow), liquid column break-up lengths are dominated by aerodynamic effects. In other words, depending on the type of flow a jet is experiencing (i.e. crossflow, co-flow, counter-flow, or a combination of these), its mechanism of atomization changes accordingly. With a flow of air normal to a multi-hole injector that sprays along a plane, it can be assumed that the individual jets produced from the injector experience flows as shown in Figure 2.10.

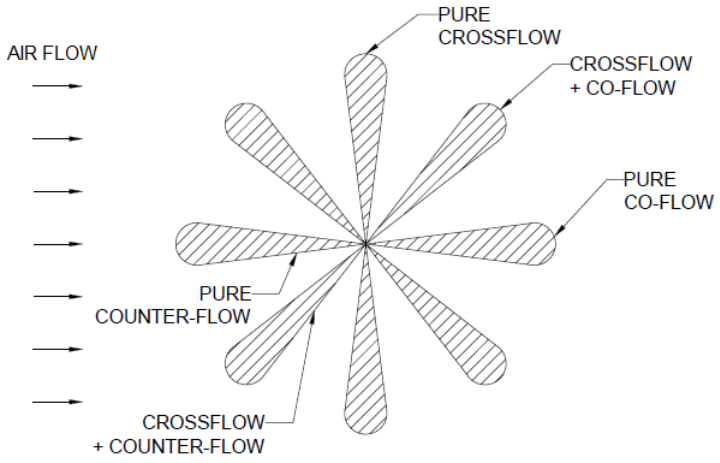

Figure 2.10: Types of flow experienced by a multi-hole injector

2.3 Biodiesel Sprays

Biodiesel is an ethyl or methyl ester produced from a chemical process called transesterification, which reacts triglycerides (any vegetable or animal fat) with an alcohol (ethanol or methanol) in the presence of a catalyst (e.g. potassium hydroxide). Biodiesels have the advantage of being non-toxic, biodegradable, sulphur-free, and non-carcinogenic [61]. The use of biodiesel also significantly decreases pollutant (e.g. soot) and greenhouse gas emissions when compared to petrol diesel because of its 9–12% oxygen, which promotes more complete combustion [61]. Past studies report that biodiesel combustion reduces particulate

matter (PM) by 47%, carbon monoxide (CO) by 47%, carbon dioxide (CO_2) by 65%–90%, and hydrocarbons (UHC) by 67% in heavy-duty highway diesel engines [62, 63]. On the other hand, it has been observed that the higher oxygen content of biodiesel increases nitrogen oxide (NO_x) emissions by approximately 10% [62].

2.3.1 Fuel Properties

The fuel properties of biodiesel are relatively similar to conventional diesel. However, the slight differences are enough to cause differences in their respective spray characteristics. It is generally agreed upon that new or altered injection strategies may be required to compensate for these differences [64, 65, 66, 12]. Table 2.2 compares the common fluid properties for biodiesel and diesel. The three major properties investigated by researchers pertaining to the spray characteristics of biodiesel are viscosity, surface tension, and density.

Viscosity is the most important fuel property of the three as it influences the operation of the fuel injection equipment [66]. It affects the internal fluid friction or resistance of the fuel to flow within the pipelines and injector. Lefebvre indicates that higher viscosity hinders atomization by lowering the Reynolds number and preventing the instabilities required for jet disintegration [12]. Higher viscosities of a liquid results in larger viscous losses, meaning less energy is available for atomization, as well as larger droplet diameters. The viscosity of biodiesel can be 3–5 times higher than that of conventional diesel [63]. Viscosity becomes a major issue when biodiesel is utilized in cold climates, since viscosity is inversely proportional to temperature.

Surface tension represents the force that resists the formation of new droplets [12]. Biodiesel's higher surface tension increases the resistance of the liquid jet to form droplets, essentially decreasing the total liquid surface area [67]. Consequently, the biodiesel jets penetrate further before break-up occurs, producing smaller spray angles [68].

Density is another important property in fuel sprays. Biodiesels also exhibit higher densities than diesel. Bittle et al. [69] found that density affects the needle behaviour inside the common-rail fuel injector. Ra et al. [65] modelled the effect of 11 different fuel properties

on diesel engine combustion characteristics, such as ignition delay and burning rates, and found that liquid fuel density is one of the most sensitive properties. Likewise, Pandey et al. [70] indicate that higher fuel density requires earlier injection timing, which produces higher cylinder temperatures and NO_x emissions.

Table 2.2: Comparison of fuel properties of biodiesel and No. 2 diesel fuels [66, 71]

Property	**Biodiesel**	**No. 2 Diesel**
Density, 288K, kg/m^3	860–895	840–860
Cetane number	46–70	47–55
Cloud point, K	262–289	256–265
Pour point, K	258–286	237–243
Flash point, K	408–423	325–350
Oxygen, wt%	11.25	0
Kinematic viscosity, at 313K, mm^2/s	3.6–5.0	1.9–3.8
Dynamic viscosity, at 313K, cP	5.626	1.69
Surface tension, at 298K, N/m	0.00296	0.0020
Higher heating value, MJ/kg	39.3–39.8	45.3–46.7

2.3.2 Spray Characteristics

The fundamental aspects of biodiesel spray characteristics are studied much less than the overall engine performance or emissions generated by biodiesel-fueled engines. However, the spray characteristics of biodiesel are important to study if biodiesel is to be used as an alternative fuel, especially if used without modification of the existing diesel engine. Som et al. compared computationally the injection and spray behaviours of diesel biodiesel. They concluded that biodiesel's viscosity attributes to decreased injection velocity, discharge coefficient, turbulence and cavitation levels, and mass flow rate when compared to petroleum diesel [71]. A fuel temperature increase of 60K is required to compensate for these viscous

losses. Also, their models predict that biodiesel exhibit longer spray penetration and larger droplet sizes in the primary break-up region, consistent with experimental studies. Som et al. suggested that revised piston bowl designs and injection and ambient conditions may improve biodiesel usage in engines. The simulations of Pogorevc et al. show that biodiesel distributes the fuel spray over a larger area of the piston chamber, but at the expense of larger spray droplets and slower evaporation rates compared to diesel [72].

Experimental studies consistently shows longer spray penetration and smaller spray angle for biodiesel compared to diesel as a result of fuel properties [68, 73, 74, 75, 72]. This implies that biodiesel degrades atomization if injected in the same conditions as diesel. Mancaruso et al. [33] explain that biodiesels exhibit longer spray penetrations compared to diesel because of their higher densities, which slow down the air entrainment process, producing fuel jets with higher velocities that penetrate further. Kastengren et al. [76] collected ensemble-averaged near-nozzle sprays of non-evaporating biodiesel and biodiesel-diesel blends using X-Ray radiography. They hypothesized that biodiesel spray cores are less fuel dense than diesel spray cores, which could explain the reduction of soot emissions for biodiesel. However, they observed narrower cone angles and denser spray core regions for the biodiesel blend compared to the diesel fuel, meaning the soot reduction may not be attributed to the change in spray characteristics. Payri et al. [77] concluded that when cavitation occurs inside an injector orifice, a significant increase in the spray cone angle is observed, implying that cavitation enhances atomization. Park et al. [78] found that biodiesel results in lower cavitating flow rates than diesel due to the higher viscosity, density, and fuel to injector wall friction.

Chapter 3

Experimental Method

3.1 Experimental Apparatus

Figure 3.1 is a schematic diagram of the entire apparatus. The apparatus involves a fuel injector placed inside a transparent wind tunnel made of Poly(methyl methacrylate), also known as PMMA or Plexiglas®. An air delivery system provides the air crossflow to the fuel spray, while a measurement system captures and records the necessary data for analysis. The following sections will describe each of these systems in detail.

3.1.1 Fuel Injection System

The fuel injection system was built using components from a 2010 Volkswagen Jetta 2.0L TDi engine. This engine employs a 3rd generation Bosch Common-Rail diesel injection system that consists of a high pressure fuel pump, common rail, fuel pressure sensor and regulator valve, and piezoelectric fuel injectors.

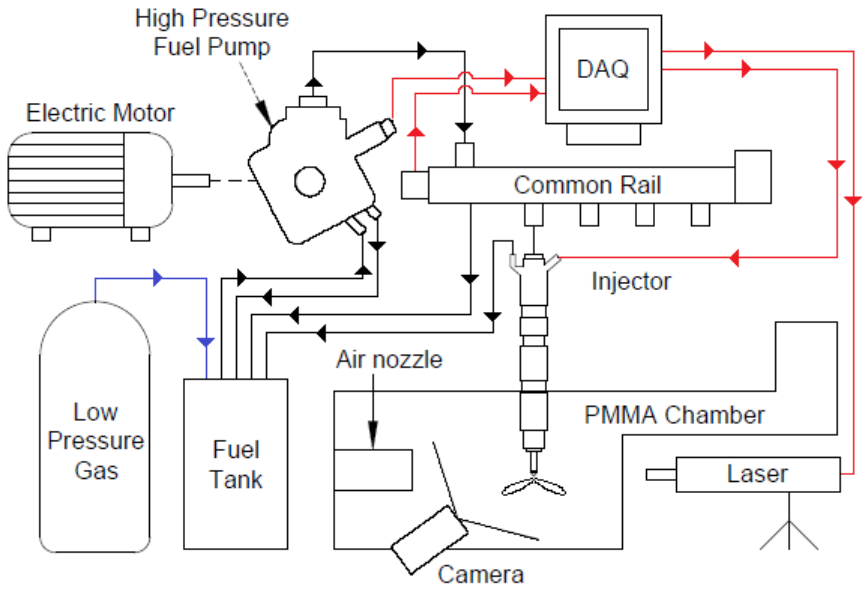

Figure 3.1: Schematic diagram of the experimental apparatus. Red - Electrical; Black - Fuel; Blue - Air

Fuel Delivery and Control

The fuel delivery system has a maximum operating pressure of 1800bar. Compressed nitrogen gas at 500kPa is used to pressurize a diesel fuel tank that is then fed into the high pressure fuel pump. The fuel pump is driven by a 2hp electric motor and pumps high pressure diesel fuel into the common rail. A 3:8 ratio pulley system reduces the motor output speed to just under 1300RPM. The common rail functions as an accumulator to maintain constant fuel pressure via the electronically-controlled fuel pressure regulator and return valve. The pressure in the common rail is dictated by the Stand-Alone Direct Injection (SADI) controller supplied by Drivven Inc. This controller is designed for use with DI injectors and is capable of controlling fuel pressure, injector electrical profiles, and injector triggering from an external input. Flexible fuel hoses supplied by KW Fuel Injection Systems carries the fuel from the common rail to the piezoelectric injector. The parameters and values used to calibrate the rail fuel pressure sensor are shown in Table 3.1.

Piezoelectric fuel injectors operate by expanding the piezo crystal stack inside the injector.

Table 3.1: Fuel Pressure Calibation

Parameter	**Value**
Nominal Pressure Range (bar)	0 – 1800
Equivalent Voltage Range (V)	0.5 – 4.5

As the stack expands, it pushes a valve open, allowing fuel to flow from the common rail to the injector orifices. The expansion of the piezo stack is controlled by applying a voltage across the piezo stack; thus, lifting the injector needle can be accomplished in an extremely short time. The higher the voltage, the larger the expansion. The electrical parameters used in controlling the voltage profile are the high voltage setpoint and the charging time. In this sytem the high voltage setpoint is 150V and the charging time is 0.1ms. Due to manufacturer confidentiality, needle lift information was not attainable. Therefore, it is assumed that full needle lift is achieved in 200μs – the time that it takes for the voltage to reach and maintain 150V over the 1.5ms injection duration, as shown in a current and voltage profile trace taken from the SADI (Figure 3.2).

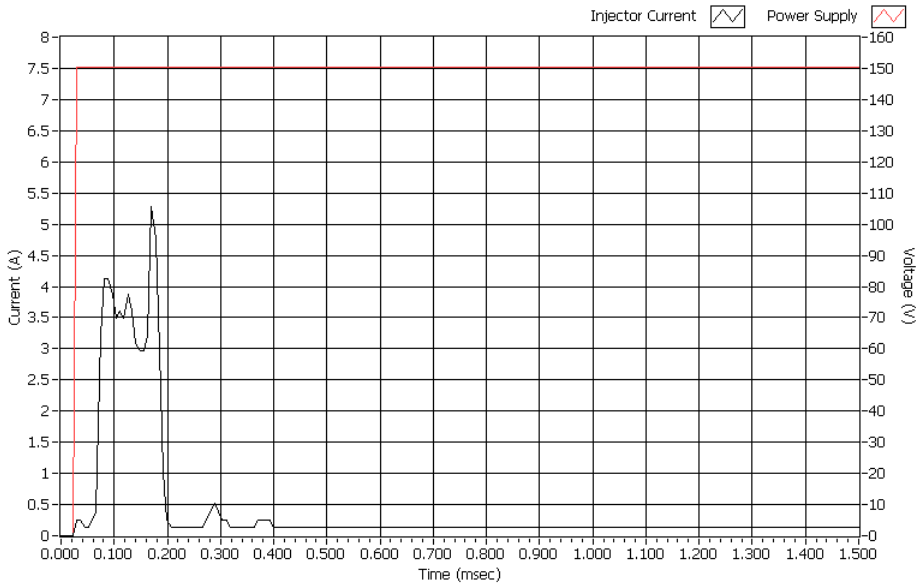

Figure 3.2: Sample current and voltage profile

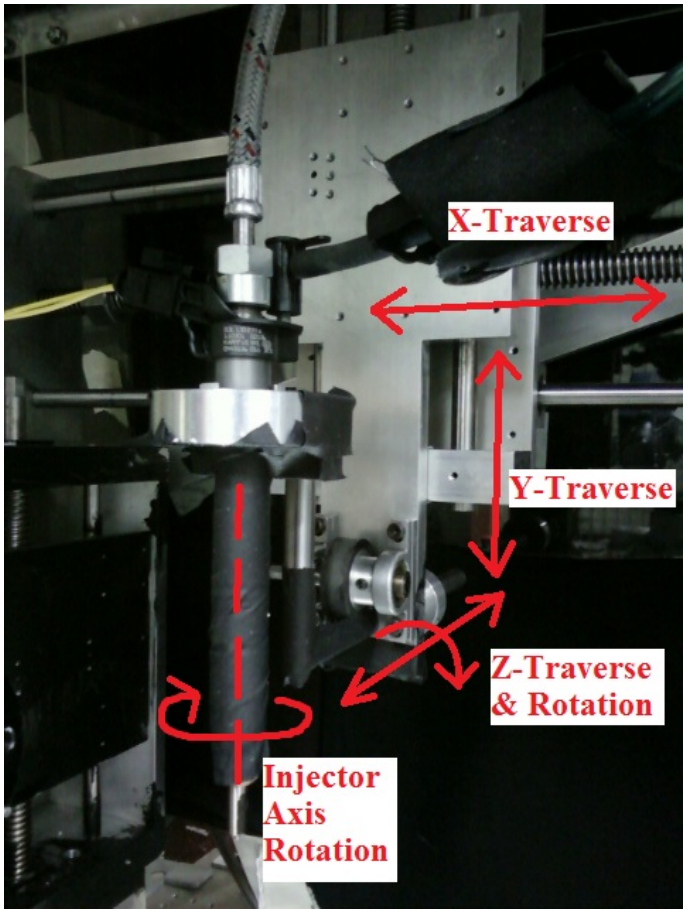

Figure 3.3: Injector traverse system

Injector

The injector is mounted on a three-axis traverse system that moves independently of the air jet nozzle, as shown in Figure 3.3. The injector is also free to rotate about its own axis and the z-axis. Digital microscopy (Appendix A) revealed that this particular injector has eight 100μm orifices symmetrically positioned around a 3mm long tip, as seen in Figure 3.4a and Figure 3.4b. Figure 3.4c shows one of these orifices at 50 times magnification.

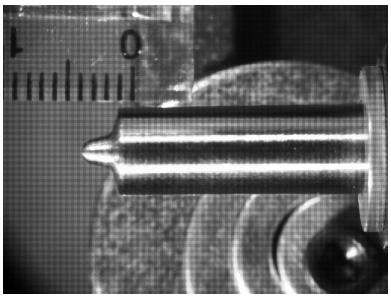

(a) Injector tip

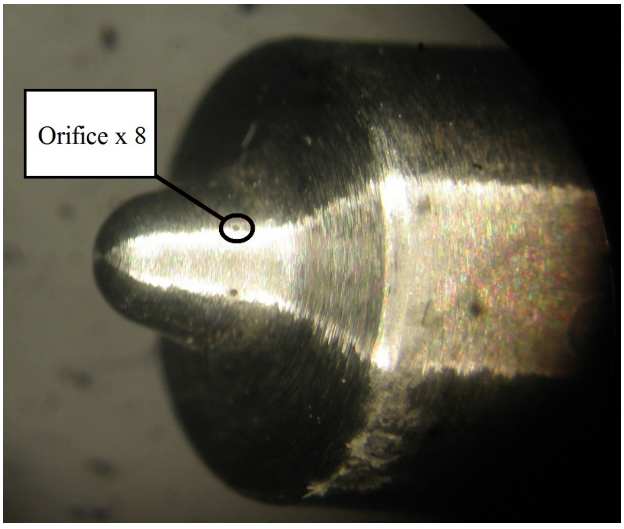

(b) Orifice location

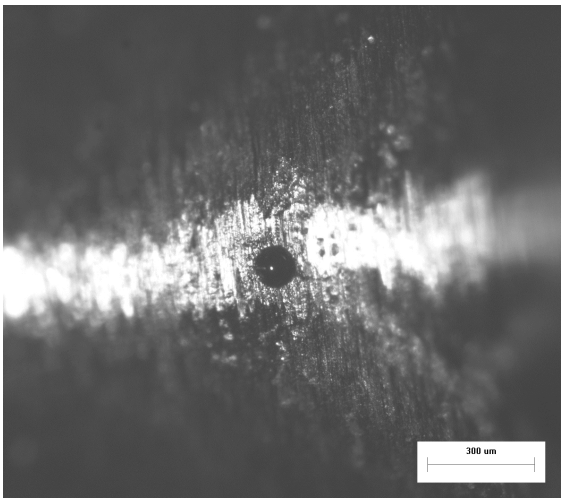

(c) Injector orifice at 50x magnification

Figure 3.4: Injector Geometry

3.1.2 Air Delivery System

The air delivery system provides the crossflow of air to the fuel spray. This is achieved using a ring compressor supplied by Air Power Products Limited and controlled by a variable frequency drive (VFD). The maximum air flow rate is 85L/s. The ring compressor is connected to the air nozzle, delivering the air jet into the PMMA wind tunnel. In a direct injection gasoline engine, the velocity of air inside the engine cylinder during the intake stroke can reach over 120m/s. [79] Therefore, the air nozzle was designed and modelled in Fluent to achieve velocities of up to 200m/s in the potential core of the air jet. The actual apparatus achieves velocities of over 220m/s. The air nozzle was designed in-house based on wind tunnel test section principles in order to achieve a relatively uniform and low turbulence jet stream. The air nozzle consists of three sections as is illustrated in Figure 3.5.

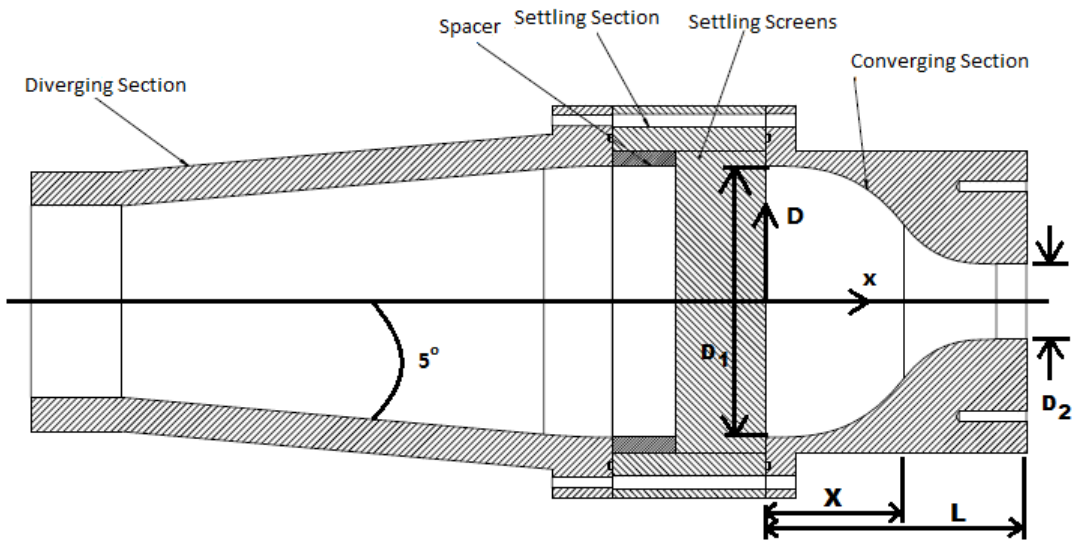

Figure 3.5: Cross-sectional view of air nozzle

The diverging section expands at a 5° angle from the nozzle centerline. This 5° angle was chosen to reduce the probability of separation, as recommended by Tavoularis. [80] A settling section is then used to reduce the size of the turbulent structures resulting from the diverging section. Following the guidelines of Indelchik, a metal honeycomb of 5.08cm thickness is enclosed between two sheets of higher porosity wire mesh and further enclosed

by two sheets of smaller porosity wire mesh. [81] The percentage of open space in the both wire meshes is kept at a minimum of 62%. The settling section schematic is shown in Figure 3.6.

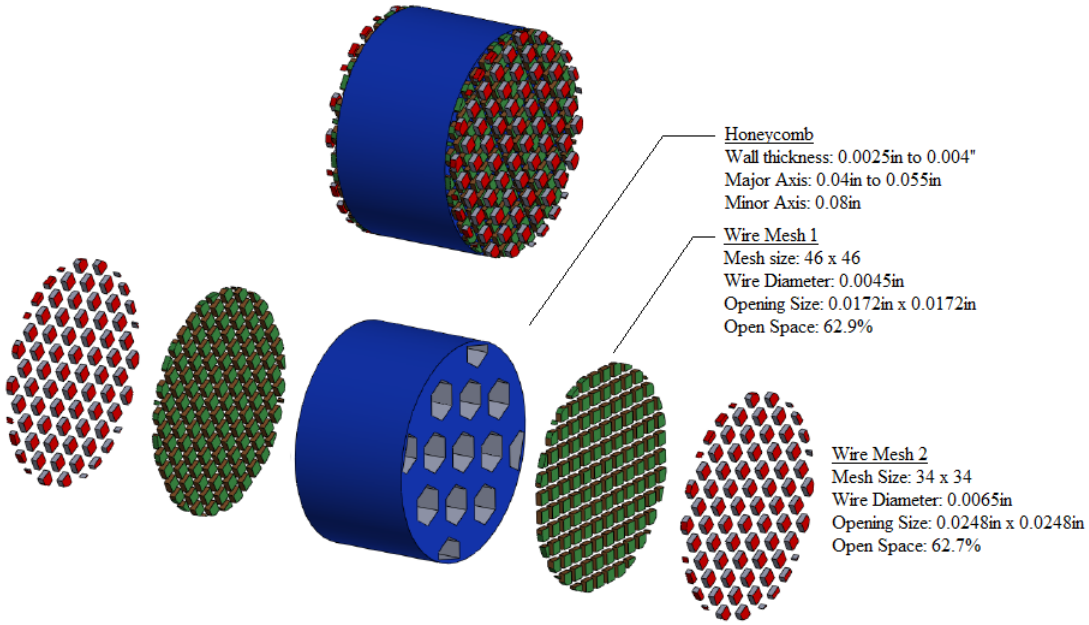

Figure 3.6: Air nozzle settling section components and dimensions

The profile of the converging section was designed according to the methodology presented by Morel and then validated experimentally by Tulapurkara et al. [82, 83] A contraction ratio of 13 and a nozzle outlet diameter of 25mm were selected, according to Bradshaw and Pankhurst [84]. The final profile of the converging section and its calculations can be found in Appendix B.

3.1.3 Measurement System

Air Pressure and Temperature Measurements

Pressure and temperature measurements were taken to characterize the air flow and maintain consistent test conditions throughout all experiments. Due to their low sensitivity to

yaw angle variation and isotropic turbulence, Kiel probes were chosen to measure total gage pressure in the air flow. Kiel probes also have better performance in turbulent environments compared to Pitot tubes. The Kiel probes were connected to voltage output pressure transducers, which sent voltage readings to the computer. The voltage readings were then converted to pressures. Refer to Appendix C) for equipment specifications.

T-type, ungrounded, and sheathed thermocouples from Omega were used for measuring the temperatures of the high velocity air and ambient air. The sheath has a diameter of 0.062" and helped to prevent damage to the thermocouple. The thermocouple wires were connected to a high accuracy data logger, which monitored the temperatures. A summary of the specifications is listed in Table 3.2.

Total gage pressure and temperature were measured by inserting the Kiel probes and thermocouples at the inlet and outlet of the air nozzle, as indicated in Figure 3.7.

Table 3.2: Temperature Measurement Hardware (Details – See Appendix C)

Hardware	**Supplier/Part Number**	**Accuracy**
Thermocouple	Omega/TMQSS-062U	$1.0°C$ or 0.75%
Data Logger	Omega/HH506A	$\pm$(0.05% reading + 0.3°C)

Velocity Measurements and Imaging

The velocity measurement system used in this study is a high resolution Particle Imaging Velocimetry (PIV) unit provided by LaVision Inc. The light source for the PIV system is a Quantel "Evergreen 70" Nd:YAG dual cavity pulsed laser, which emits 532nm wavelength beams at up to 70mJ of power per pulse. The time between the two laser pulses, or pulse width, can be controlled down to 0.5ns. This allows the system to capture characteristics of high speed fluid flows. Two types of optical lenses are used to alter the laser beam. The first of which is the spherical lens. This lens spreads the focused laser beam into a planar

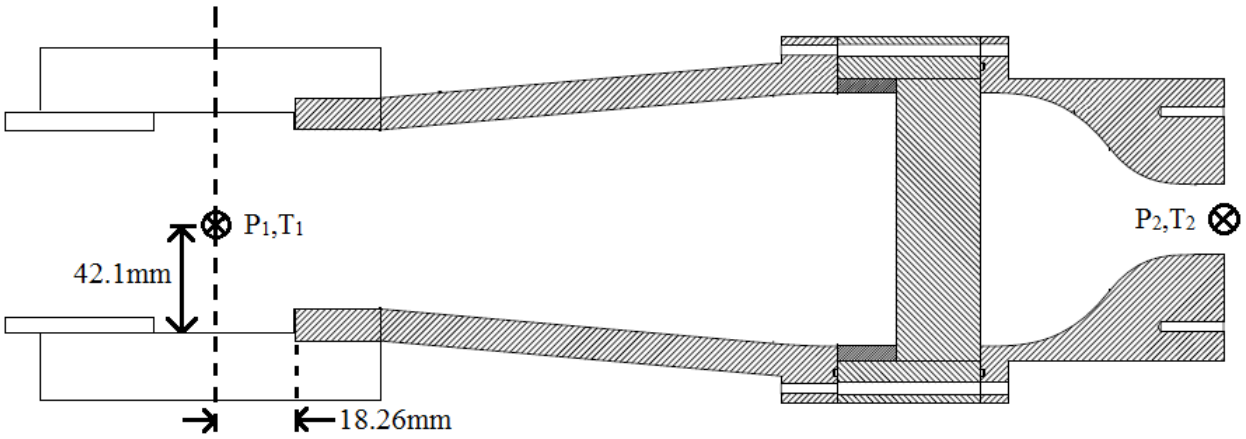

Figure 3.7: Pressure probe and thermocouple locations in air nozzle

sheet. The second lens, a cylindrical lens of focal length of -10mm or -20mm, thins the laser sheet down to a thickness between 1mm and 4mm. The sheet optics unit on the laser head allows the waist focal length of the laser sheet to be adjusted between 300mm and 2000mm.

Imaging in this study was done using a LaVision Imager Intense CCD camera, fitted with a Nikon lens (60mm, F2.8 or 50mm, F1.8) and 532nm bandpass interference filter to reduce background noise of captured images. The camera is positioned towards a 12in x 12in flat mirror that is secured under the injector tip, as shown in Figure 3.8. This allowed the camera to capture all eight fuel spray plumes simultaneously. The camera, laser, and fuel injector were triggered using a programmable timing unit (PTU), which is controlled via LaVision's DaVis 8 software. DaVis was also used for pre- and post-processing operations. Table 3.3 summarizes the important specifications of the camera.

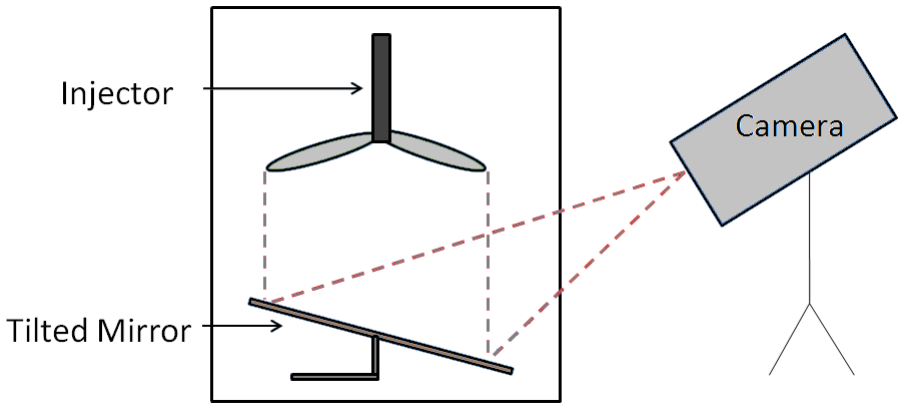

Figure 3.8: Position of camera and mirror relative to spray

Table 3.3: Imager Pro X 2M Specifications

Parameter	**Value**
Resolution (px)	1648 x 1214
Frames/second	110
Interframe time (ns)	500
Exposure time (ns)	30
Pixel Size (μm)	7.4

Seeding Material

In order for the laser to capture the air motion, the air flow must be seeded with particles that the laser illuminates. This was accomplished using a Laskin Nozzle Aerosol Generator. Di-2-ethylhexyl-sebacate (DEHS) oil was fed into an aerosol generator capable of producing 1μm to 2μm diameter particles at a rate of 1.4 to 20 x 10^8 particles per second.

3.2 Experimental Conditions

The parameters varied for the experiments are air jet velocity, fuel type, fuel injection pressure, and x-location of the injector tip. The following sections describe these parameters and their levels in more detail. All the test matrices can be found in Appendix E.

3.2.1 Air Crossflow Velocity

In addition to the quiescent environment condition, three velocities were considered in this study: 49.3m/s, 125.0m/s, and 213.7m/s along the centerline of the jet and in the potential core region (Figure 3.9). These velocities were measured using particle image velocimetry (PIV), which is explained in Section 4.1. The temperature of the air jet increased with jet velocity due to air compression and friction. Table 3.4 summarizes the average air jet centerline temperatures the average ambient temperatures inside the wind tunnel chamber along with their one standard deviation variations as a function of the jet velocity.

Table 3.4: Air jet temperature rise as a function of air jet velocity

Air Velocity (m/s)	0	49.3	125.0	213.7
Avg. Jet Temperature (°C)	24.3±0.9	27.1±1.1	40.2±1.6	73.3±1.6
Avg. Ambient Temperature (°C)	24.3±0.9	24.6±1.0	30.7±1.5	45.2±1.6

3.2.2 Fuels and Fuel Injection Pressure

Three fuels are compared in this study. No. 2 Diesel was purchased at the pump from a local PetroCanada gas station. Pure fatty acid methyl ester (F.A.M.E.) biodiesel was obtained from Rothsay Biodiesel in Guelph, Ontario (specifications can be found in Appendix D). A diesel-biodiesel blend was produced from a mixture of 20% biodiesel and 80% diesel. The surface tension was measured using a goniometer from ramé-hart (Model 590,

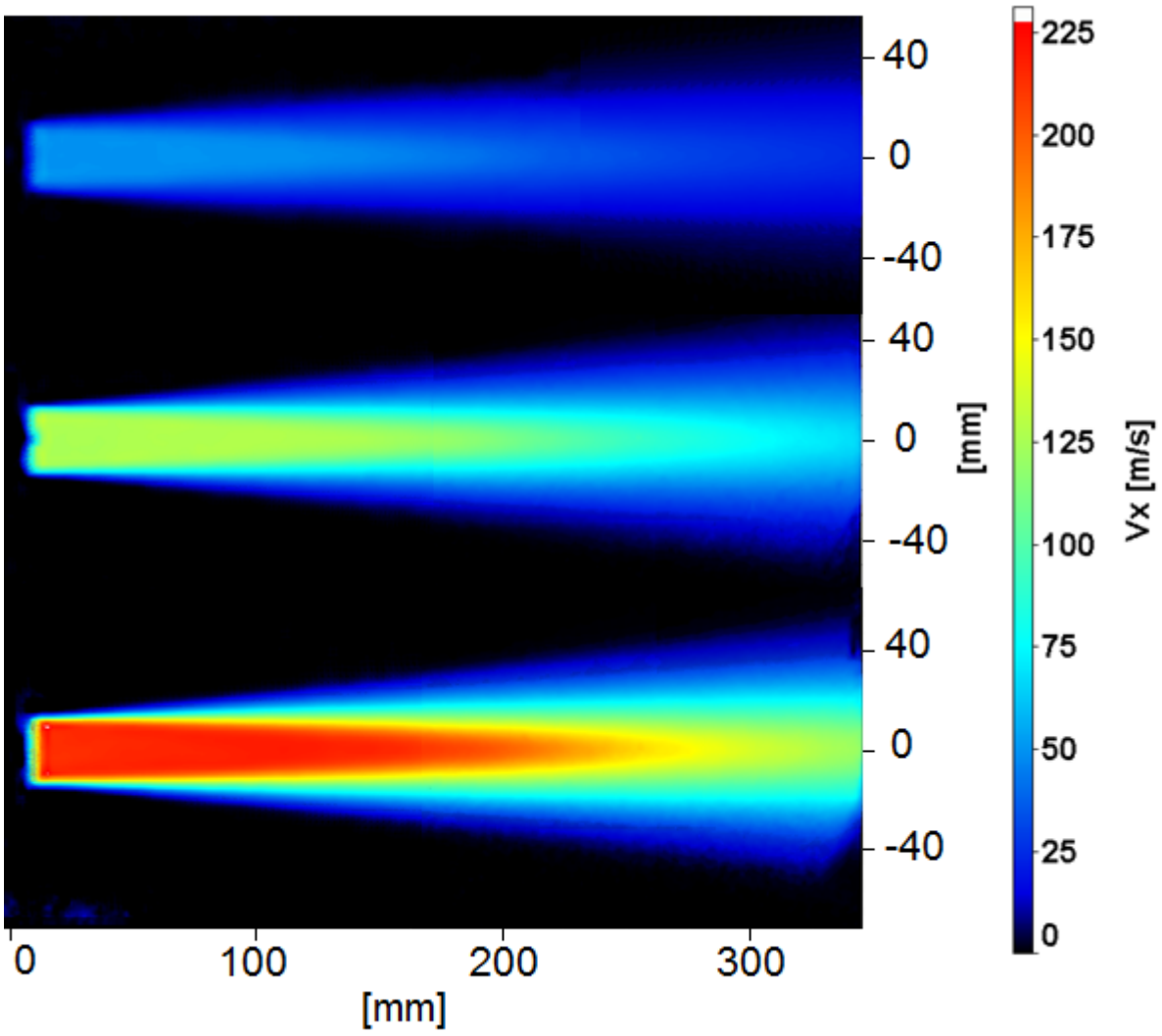

Figure 3.9: Air jet characterization velocity vector maps

F4 Series) and the dynamic viscosity was measured with a Fungilab Smart Series Rotational Viscometer. Table 3.5 summarizes the fuel properties at 21.1°C and their associated measurement errors. The same fuel properties were measured at the air jet temperatures encountered in the experiments and the results are shown in Figure 3.10. Two injection pressures are considered in this study: 1200bar and 1500bar.

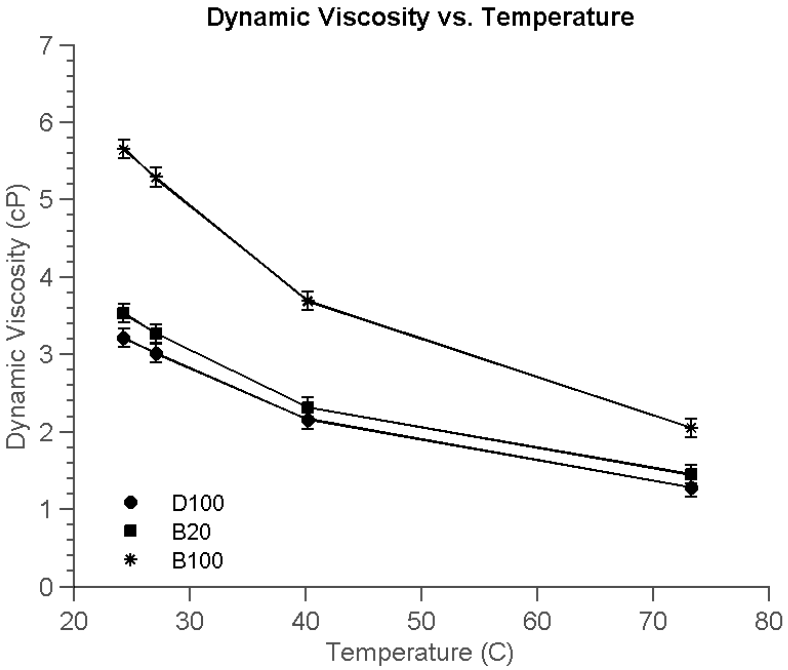

(a) Dynamic viscosity (cP)

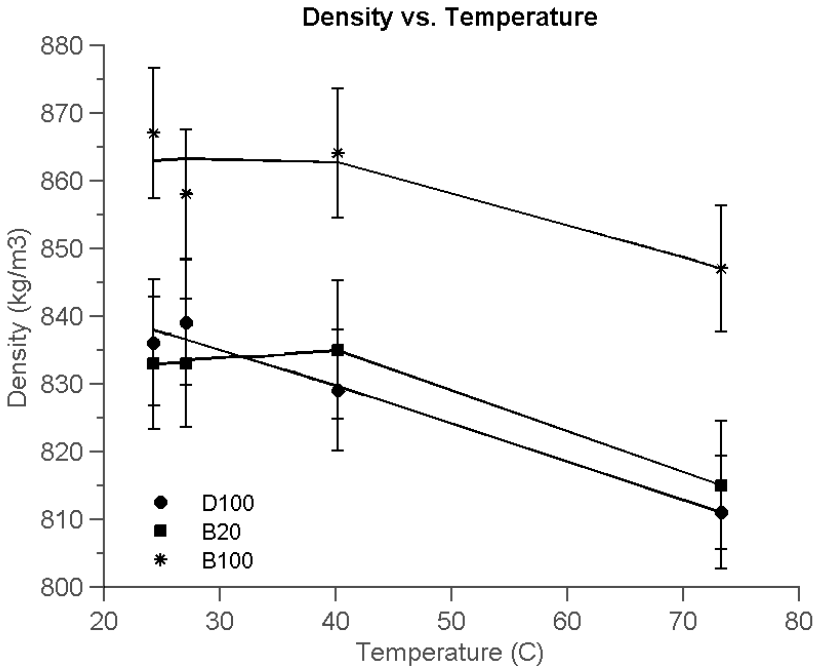

(b) Density (kg/m^3)

Figure 3.10: Change in a) fuel dynamic viscosity and b) fuel density as a function of the air jet temperature

Table 3.5: Summary of tested fuels at 21.1 °C

Fuel Type	**Surface Tension (mN/m)**	**Dynamic Viscosity (cP)**	**Density (kg/m^3)**
Pure No. 2 Diesel (D100)	27.1±0.1	3.4±0.12	830±9.3
20% Biodiesel-Diesel Blend (B20)	28.1±0.1	3.7±0.12	850±9.8
Pure Biodiesel (B100)	30.5±0.1	6.0±0.12	883±9.6

3.2.3 Position of Injector Tip

The injector tip was positioned at y=0mm and z=0mm for all experiments. The x-location, or the distance downstream of the air nozzle outlet, is equal to 37.5mm or 250mm, which correspond to the non-dimensionalized x/D values of 1.5 and 10, where D=25mm is the air nozzle outlet diameter. Calculations for potential core length in existing literature ranges from x/D=4.7 to x/D=7.7. [85, 86, 87]. At these locations, the jet velocity can be represented as approximately 90% to 99% of the jet velocity right out of the air nozzle. Figure 3.11 illustrates how for all three crossflow velocities, x/D=1.5 falls within the potential core region of the air jet where the velocity is quite uniform and x/D=10 falls outside the potential core and in the fully-developed turbulent region. A comparison between these x-locations can provide insight on the effect of airflow motion on fuel spray characteristics.

3.2.4 Injection Timing

The injection pulse width used for all spray events is 1.5ms. Due to the charging time required to life the nozzle pin inside the injector, an inherent delay of approximately 0.35ms exists between the PTU trigger signal and the emergence of fuel from the injector. Thus, all images were taken with respect to the injector trigger as opposed to the start of fuel. For 0m/s crossflow velocity, sprays were found to exceed the size of the mirror beyond 0.8ms and thus images cease there. For the three other velocities, images were captured up until

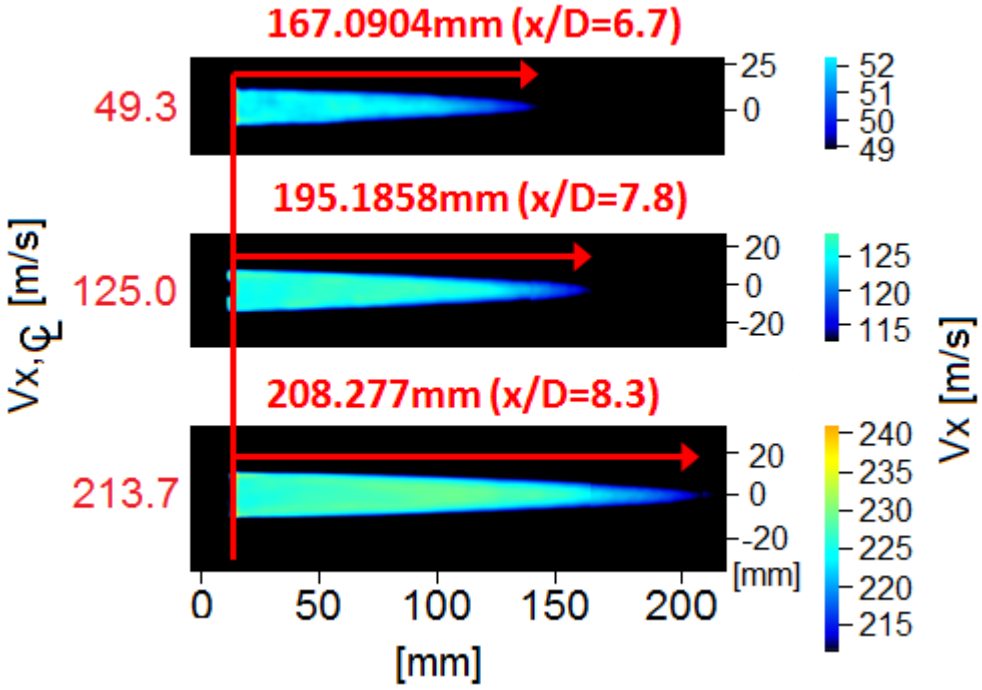

(a) 90% core velocity

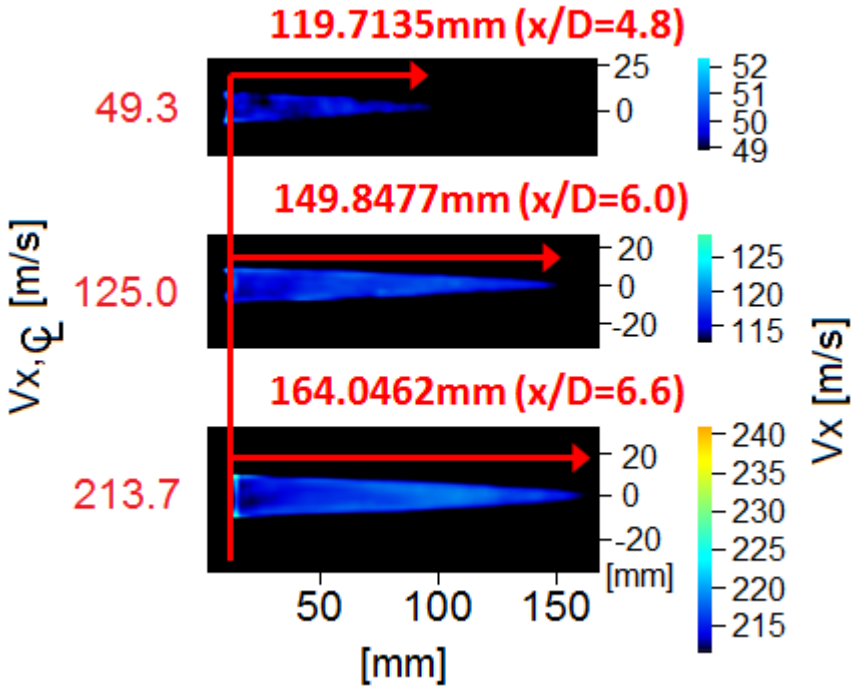

(b) 99% core velocity

Figure 3.11: Potential core lengths based on a) 90% of core velocity and b) 99% of core velocity

1.0ms. The laser trigger signal was used as the reference signal at all times and designated as T1A (for the first laser pulse). The camera was always triggered simultaneously with the laser. The injector trigger was offset by the image time steps chosen for both the spray imaging and spray PIV experiments. To take an image at 0.5ms after the trigger signal, for example, a device offset of -500μs is inputted into DaVis. This means that the injector trigger signal (the device) is triggered 500μs prior to the T1A, such that when the laser and camera capture is triggered, they coincide with the spray at 500ms after the start of injection.

3.3 Experimental Procedure

3.3.1 Calibration

The camera must be focused on the same plane as the laser sheet in order to capture images where particles are best illuminated. To locate this plane, a calibration board was designed, such that it can be mounted tightly against the air nozzle outlet face, as shown in Figure 3.12. The dot diameter is 6mm and the centre-to-centre distance between dots is 16mm in both x- and z-directions. The camera is focused using the camera's three-axis gearhead and the manual focus on the lens. The DaVis calibration sequence uses a camera pinhole method of calibrating the dot dimensions and dewarps the images according to this scale. Every image taken henceforth can be processed according to the calibration such that it is dewarped and rescaled properly. The point of origin is defined with the air nozzle outlet face being x=0, the centre point of the air nozzle outlet being z=0, and the face of the board with the dots is aligned with y=0. An RMS value of the error associated with the calibration is calculated by DaVis. For all the experiments conducted, the RMS value is under 0.5 of a pixel. After calibrating the camera, the board is flipped 180° in order to locate the injector tip to y=0, as shown in Figure 3.13. The laser is also adjusted such that it illuminates evenly across the dotted face (Fig 3.14). For all experiments, the laser sheet thickness was in the order of 1mm to 2mm. With these steps complete, the injector tip, camera, and laser sheet are now all lined up to the same plane.

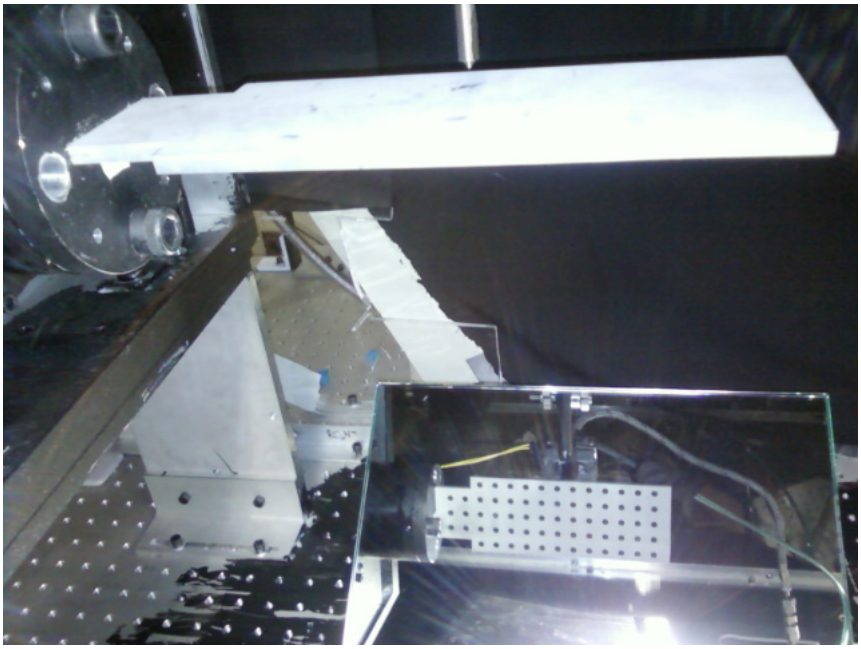

Figure 3.12: Calibration board secured on air nozzle outlet

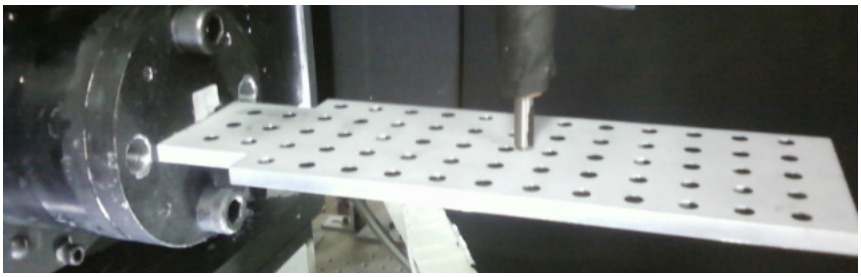

Figure 3.13: Positioning injector tip to y=0

3.3.2 Spray Imaging

Spray images provide a visual and qualitative progression of the spray plumes from the start of injection until the plumes penetrate past the camera's field of view. Processing these images allows for the calculation of spray penetration curves and axis deflection curves, which can be used to identify the effects of crossflow velocity, injection pressure, and fuel type on the macroscopic spray characteristics. Spray development was captured by taking images from 0.3ms to 1.0ms after the trigger signal, with increments of 0.1ms. A total of 25 images per time step were taken, each corresponding to a stand-alone injection

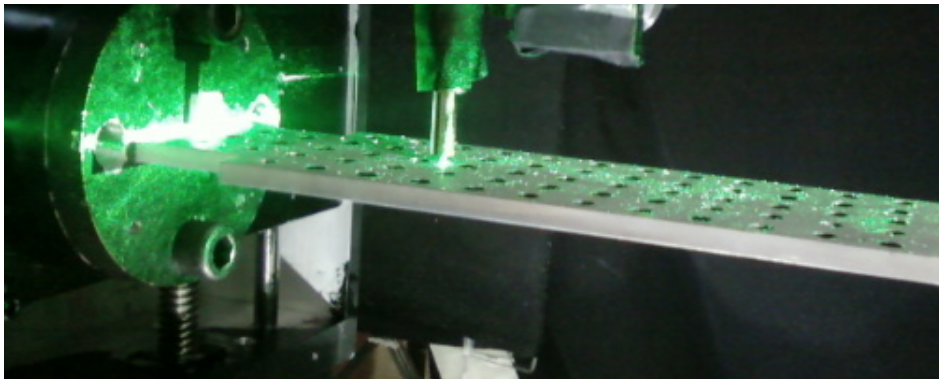

Figure 3.14: Positioning the laser sheet to y=0

event. The image recording rate for all experiments was kept between 1hz and 6hz so that fuel particles and vapours from the previous injection event can dissipate prior to the subsequent image. For all experiments done, an x-z-plane laser sheet was located through the centre of the air nozzle outlet. Because the x-z plane laser sheet is orthogonal to the injector axis, it is capable of illuminating all eight spray plumes simultaneously.

Chapter 4

Data Analysis

4.1 Air Velocity Vector Calculation

The particle image velocimety (PIV) technique provides a method of visualizing and creating a velocity vector map across a selected flow field. The PIV algorithms in DaVis work by first dividing the entire field of view into interrogation windows. The size of these windows are specified by the user and can vary between 8x8 and 512x512 pixels. Next, the time interval, dt, between the two successive laser pulses is set to a value that satisfies $0.1pixel < ds < 1/4Length_{Window}$, where ds denotes the resultant pixel shift. This is to ensure that the velocities produced from the vector processing are reasonable and accurate. It is also ideal for scattered laser light from the particles to span 2 to 3 pixels on the camera sensor to avoid peak locking (explained in Section 4.3). Using cross correlation, DaVis statistically determines the shift of the intensity pattern inside each interrogation window to correspond with the displacement of that window in the flow field. Combined with the value of dt, a velocity is found.

In this study, an x-z-plane laser sheet through the centre of the air nozzle outlet was used for all the PIV imaging. Seeding particles were introduced into the airflow at the intake of the air compressor. At least 5 to 10 particles were present per interrogation window

to ensure a sufficient seeding density. 4000 images were taken at each crossflow velocity. The air jet PIV images were then pre-processed by subtracting the minimum intensity encountered over the 4000-image time series from each image in the series (Figure 4.1. The purpose of this pre-processing step is to eliminate undesirable high intensty fluctuations due to background reflections. DaVis then takes the pre-processed images to calculate the velocity vectors. Cross correlation was accomplished using 5 iterations (3 passes using 64 x 64 pixel interrogation windows, followed by 2 passes using 32 x 32 pixel interrogation windows and 50% window overlap). Pixel shifts in the potential core region were measured to be in the range of 6.3 to 11.1 pixels across all images for all three cross flow velocities, satisfying the recommended pixel shift for good vector calculation. Finally, DaVis corrects the image by applying the calibrated scale and point of origin.

4.2 Spray Geometry

Spray images are first pre-processed in DaVis in order to reduce the background noise due to laser light reflections and structural objects. This was done by subtracting an image of the field of view with no spray. Next, the pre-processed spray images were binarized and segmented using the MATLAB 'Canny' edge detection command [88]. The algorithm uses a σ value to first smooth the image using a Gaussian filter and then high and low threshold values, T_H and T_L, to perform hysteresis thresholding and determine the connectivity of detected edges. The algorithm behind Canny edge detection is detailed in Appendix G. The 8 individual plumes were sectioned off into regions according to a polar coordinate system with the origin being the tip of the injector. Because the momentum ratios encountered in this study were so high, the deflection of the plumes were low. Therefore, the spray penetration lengths can be approximated using straight line distances as opposed to the arc length. Using the equation for the distance of a line, the spray penetration length was calculated between the origin and the furthest edge point in each region. The spray axis can be defined as the line between two points: the injector tip and the furthest detected edge point in the region. The axis deflection angle can then be calculated as the angle between the injector axis and this spray axis. The average of the 25 images per spray event is calculated to find the representative spray penetration and axis

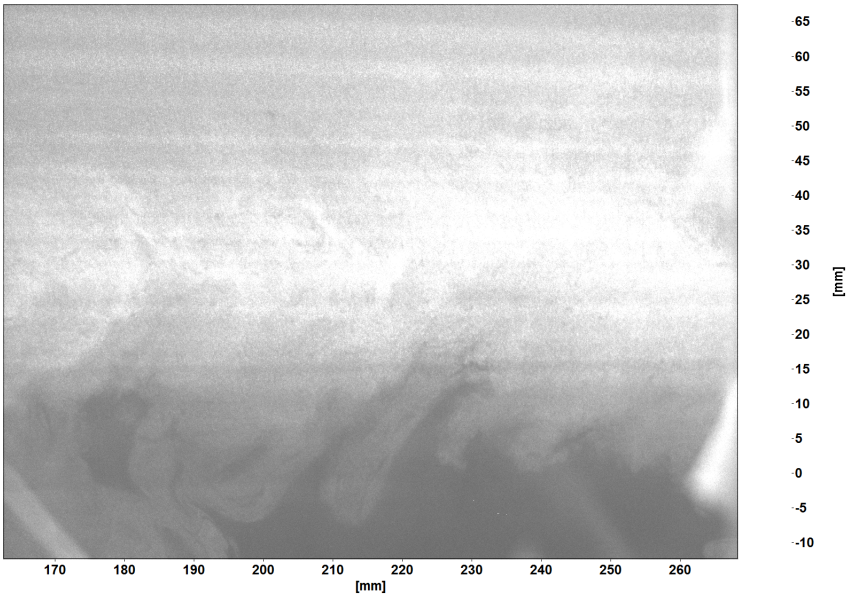

(a) Raw image

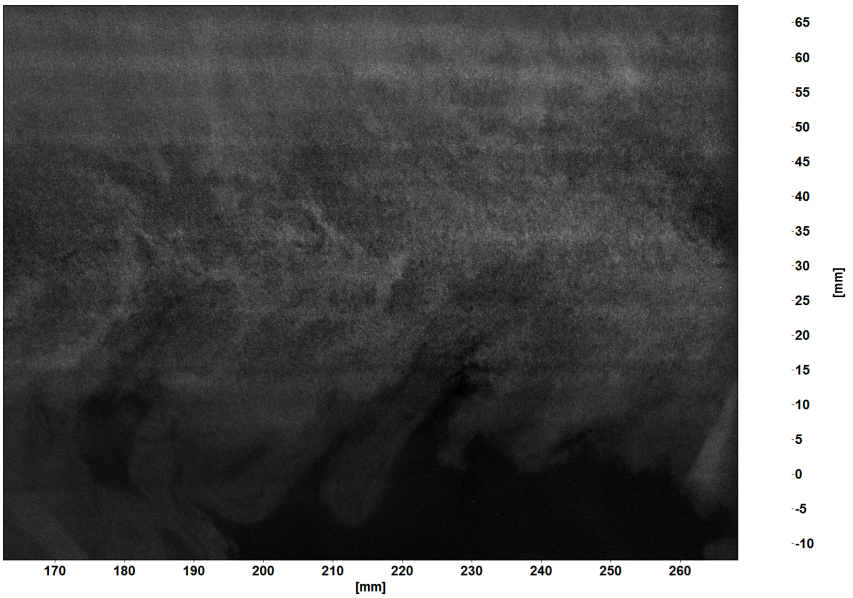

(b) Background subtracted image

Figure 4.1: Effect of background subtraction on PIV images

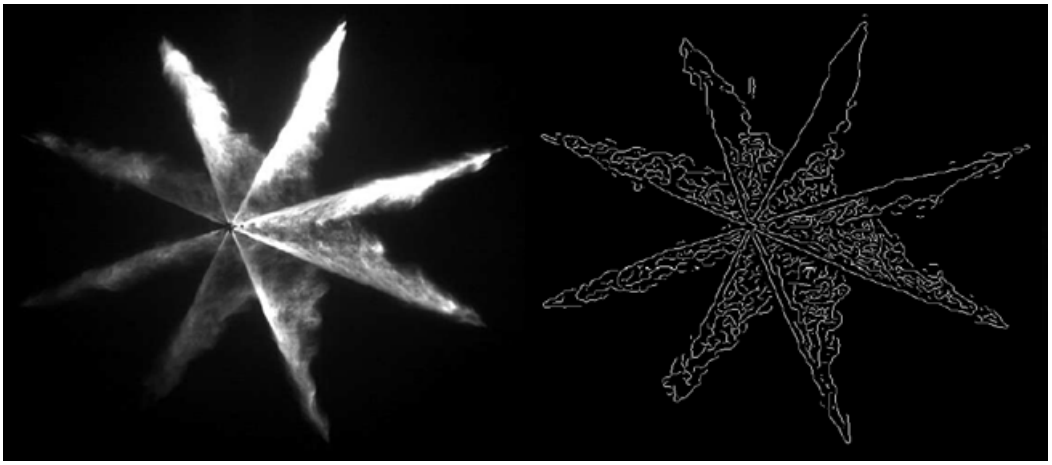

(a) Raw image (b) Edge-detected image

Figure 4.2: Result of binarization and segmentation using Canny edge detection on an instantaneous spray image

deflection at that specific fuel type, fuel injection pressure, crossflow velocity, x-location, and time step.

4.3 Experimental Uncertainties

4.3.1 PIV Uncertainties

PIV uncertainties are very difficult to quantify due to the large number of factors that contribute to the uncertainty. Inamura et al. estimated that variations in mean air velocity in the cross section were less than 4% of the max mean velocity. [52] Other similar studies reported velocity uncertainties between 1% and 7.2%. [89, 90] By following similar PIV technique and assuming similar uncertainties, the best estimate of the uncertainty in the PIV velocities computed from this study is 5%. The following sections will detail the major factors that affect the overall velocity uncertainty.

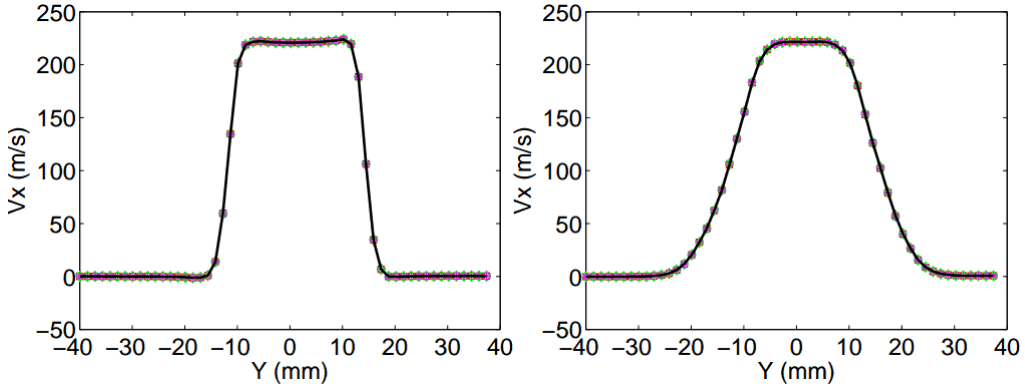

(a) x/D=1 (b) x/D=4

Figure 4.3: Velocity profile for 500 (cross), 1000 (circle), 1500 (square), 1800 (diamond), 1900 (asterisk), and 2000 (line) averaged images.

Number of Realizations

The air jet velocities are computed from an ensembled average of a number of realizations of the flow, each providing an instantaneous PIV snapshot of the flow. Thus, the number of realizations contributes to the random error in the computed velocities. The higher the number of realizations, the more accurate the computed average velocity is. The number of realizations used in PIV studies done in the past range anywhere between 10 and 500. [91, 92, 93, 94]. This study took an average of 4000 PIV image pairs. As shown in Figure 4.3 [95], the average axial jet velocities for different total PIV image pairs (from 500 to 2000) do not change significantly, implying that the error associated with the number of realizations for the current study is expected to be very low.

Peak Locking

Peak locking occurs when the detected particles in the PIV images are smaller in size than a single pixel on the camera sensor. When peak locking occurs, the PIV correlation would have trouble locating the centre of the particle. In other words, PIV correlations are forced to assume the centre of the pixel as the centre of the particle, thus adding to the errors of the resulting velocity vector. To avoid peak locking, the particle should occupy 2 to 3

pixels so that the pixel intensity distribution across those pixels can be more easily located. DaVis uses a probability density function (PDF) to quantify the peak locking effect in its velocity vector maps. A zero value means there is no peak locking and a value of 1 means that peak locking is a concern. For the average centerline air jet velocities of 49.3m/s, 125.0m/s, and 213.7m/s, the peak locking values were 0.153642, 0.190692, and 0.381769, respectively. Therefore, it is assumed that peak locking did not significantly affect the velocity vector maps.

Particle Slip Velocity

Slip velocity is the difference in the average velocity of one phase relative to another, primary, phase. In PIV, a slip velocity exists between the seeder particle and the fluid flow, resulting in an uncertainty in the resultant velocity vectors. The dimensionless parameter known as the Stokes number, St, is often used to measure the reliability of seeder particle in PIV experiments. Smaller Stokes numbers correspond to smaller the slip velocities and more accurate the velocity vectors. For Stokes numbers less than 1, seeder particles follow the flow quite closely, while Stokes numbers less than 0.1 have tracing accuracy errors under 1% [96]. In this study, the slip velocities for the three averaged centerline potential core velocities, 49.3m/s, 125.0m/s, and 213.7m/s, were 6.72 x 10^{-5}m/s, 7.02 x 10^{-5}, and 7.73 x 10^{-5}, respectively, while the Stokes numbers for 2μm diameter seeder particles were 0.164, 0.29, and 0.424 F. Therefore, it can be assumed that the PIV velocities calculated from DaVis have very low slip velocity errors.

Perspective Error

With a single camera, only 2-component velocity calculations (the x- and z-components, in this case) can be resolved accurately. Therefore, any out-of-plane y-component is represented as projections on the image plane, exaggerating the resulting velocity vector with perspective error. The influence of the y-component on the resultant velocity vectors is dependent on the thickness of the laser sheet; the thinner the light sheet, the smaller the perspective error. The perspective error can be quantified in vector form as a “relative

error between the true displacement on the object plane and the apparent in-plane displacement" [97] denoted by $\epsilon = \left(\frac{\Delta z}{\Delta x} \cdot tan\Theta_x, \frac{\Delta z}{\Delta y} \cdot tan\Theta_y\right)$. The maximum errors calculated for the centerline velocities of 49.3m/s, 125.0m/s, and 213.7m/s at the air nozzle outlet were ϵ=(2.9x10^{-8}, 2.9x10^{-8}), ϵ=(8.7x10^{-9}, 8.7x10^{-9}) and ϵ=(7.0x10^{-9}, 7.0x10^{-9}), respectively. These errors are low enough to be considered negligible. This is likely because the camera was located sufficiently far away from the object plane for it to not observe significant perspective error. The details of the calculations can be found in Appendix F.

4.3.2 Fuel Pressure Uncertainties

The fuel pressure is measured using the built-in fuel pressure sensor on the common rail and recorded using Drivven's CalScope tool. The unpressurized sensor readings were recorded for approximately 3.5min to see the sensor noise. The average zero pressure reading was 0.006±0.199bar.

In addition to the noise, fuel pressure fluctuations occur inside the common rail. These fluctuations are inherent in the design of a CRDI system, resulting from propagation of the pressure waves from the opening and closing of the injector. [98, 99] Luckily, the extremely rapid response of the piezoelectric injector results in minimal pressure decrease in the nozzle orifice in the early stage of the injection process when compared to solenoid injectors. [34] The resulting average fuel pressures and their one standard deviation variations from all experiments were: 1200±3.8bar and 1500±9.4bar.

4.3.3 Imaging Processing Uncertainties

The processing of diesel spray images is not standardized among researchers. The method of binarization and thresholding used in defining spray boundaries is experiment-specific and user-specific. As a result, different processing codes can generate vastly different spray penetration lengths and axis deflection angles, even for the same image. The following sections will discuss the main factors that affect the calculated spray characteristics. Using the root-mean-square method of summing various uncertainties, the estimated total

uncertainty in the characteristics due to image processing is about 6%.

Number of Realizations

The SAE J2715 standard for gasoline fuel injector spray and measurement characterization recommends using an average of 5 spray images to calculate spray characteristics, including spray penetration and cone angle. The standard was developed for quiescent environments and for gasoline direct injection. No equivalent SAE standard exists for diesel direct injection spray characterization. In addition, the high fuel pressures encountered in this study, along with the pressure fluctuations due to the injector opening and closing beg for a higher number of realizations for an accurate ensemble mean from which to calculate spray penetration and axis deflection. The current study uses an average of 25 images for the calculation of spray characteristics. Figures 4.4 and 4.5 show the residual error between the average of 25 images and that of 5, 10, 15, and 20 images for spray penetration and axis deflection angle on an arbitrary spray case. The maximum error decreases by about 3.5mm in the spray penetration and about 3° in the axis deflection angle when increasing the number of realizations from 5 images to 25 images. For the purpose of this study, it is assumed that 25 images is a sufficient number of realizations to average out image-to-image variations.

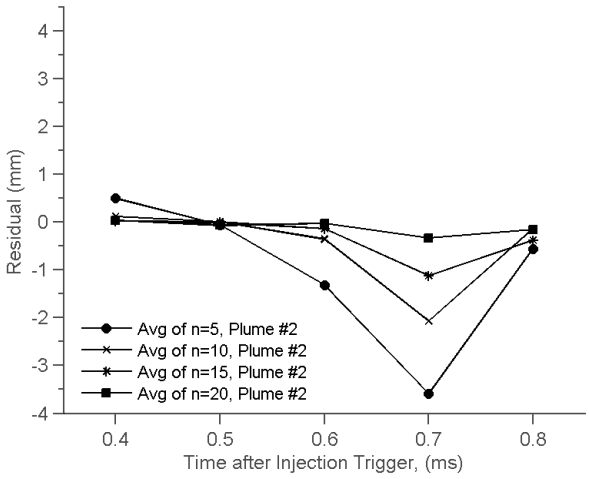

Figure 4.4: Residual error in spray penetration length between various numbers of realizations and n=25 images for D100, P_{inj}=1200bar, x/D=10, V_a=125.0m/s, Plume 2

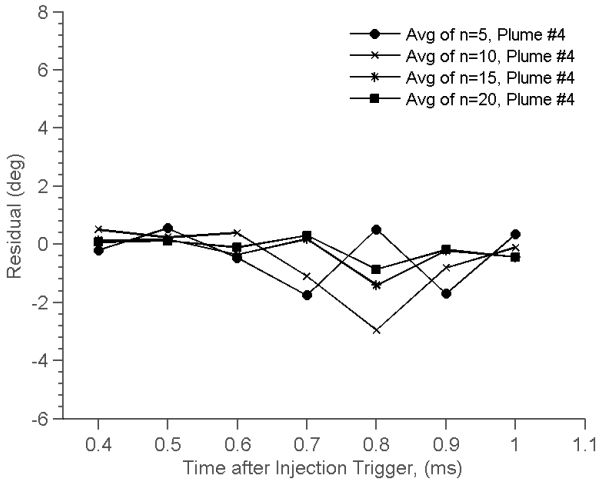

Figure 4.5: Residual error in axis deflection angle between various numbers of realizations and n=25 images for B20, P_{inj}=1200bar, x/D=1.5, V_a=213.7m/s, Plume 4

Perspective Error

An identical injector was disassembled and sent to Advanced Photon Source (APS) at the Argonne National Laboratory in Illinois. Microtomography was performed on the injector using a bending magnet X-ray beamline (2-BM) with a voxel resolution of 2.2μm. From these images, the orifice diameter was measured to taper from 152μm at the inlet to 110μm at the outlet, and the orifice tilt angle was calculated to be $\theta_{o,tilt} = 8°$ in the negative y-direction (Appendix A), as shown in Figure 4.6. Consequently, the perspective error involved in the spray penetration lengths can be estimated to be 1% using trigonometry, where $S_{measured} = cos(8) \cdot S_{actual} = 0.99 \cdot S_{actual}$.

Image Processing Uncertainty

A sensitivity analysis was performed to quantify the sensitivity of the σ, T_H, and T_L values used in the MATLAB 'Canny' edge detection command. Figure 4.7 shows the effect of increasing σ from 0.5 to 2.5, and the resulting increase in background noise reduction. However, the spray penetration length and axis deflection angles calculated from these processed images do not differ by much. By default, MATLAB sets $\sigma = \sqrt{2} \approx 1.414$. The

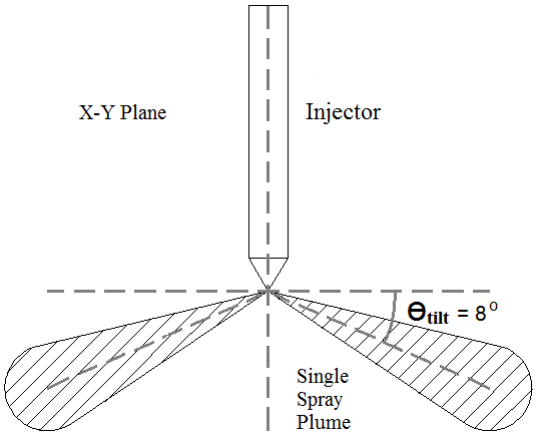

Figure 4.6: Orifice tilt angle

values for σ used in this study range from 1.8 to 2.7, implying that the images required more than typical smoothing to reduce pixel noise. The uncertainty pertaining to the sensitivity of the σ value can be estimated to about 1%. The sensitivity of T_L is insignificant, as shown

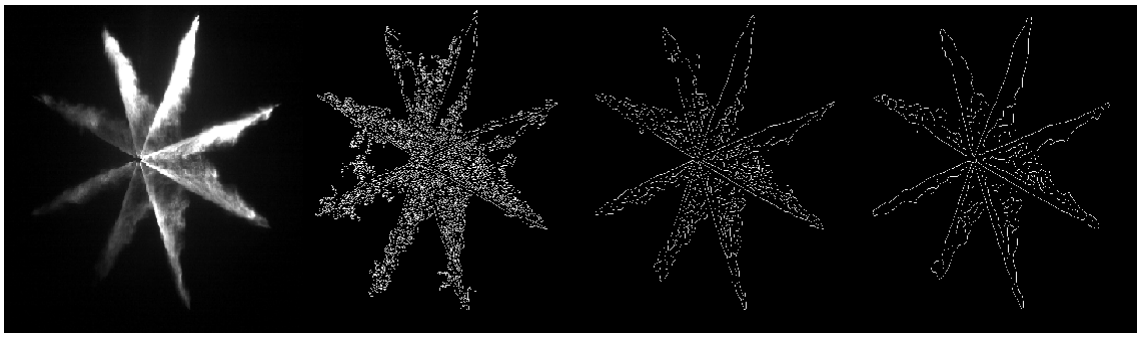

Figure 4.7: Sensitivity of σ on final Plume 1 spray penetration and axis deflection calculations (from left to right): Original instantaneous image; $\sigma = 0.5, S = 89.97$mm, $\theta_{def} = 2.7°$; $\sigma = 1.5, S = 90.05$mm, $\theta_{def} = 2.5°$; $\sigma = 2.5, S = 88.36$mm, $\theta_{def} = 3.0°$

in Figure 4.8. This is because the T_L value determines the threshold below which the edge detection command sets the pixel intensity to zero. Using the background subtraction operation in DaVis, the distinguishability between fuel and background pixels is quite high. Therefore, the T_L value must be unreasonably high to cause an effect. On the other hand, the sensitivity of T_H is very high. As shown in Figure 4.9, an increase of less than 1 in the value of T_H results in a drop of approximately 10mm in spray penetration. The values for T_H used in this study range from 0.01 to 0.06, the uncertainty pertaining to the

sensitivity of T_H can be estimated to about 5%.

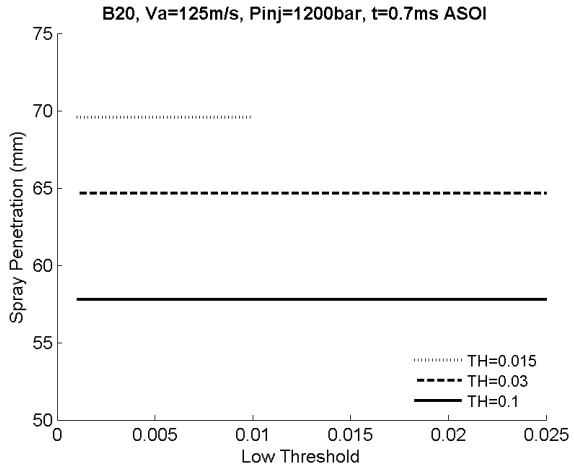

Figure 4.8: The sensitivity of the low threshold, T_L, in the MATLAB edge detection command

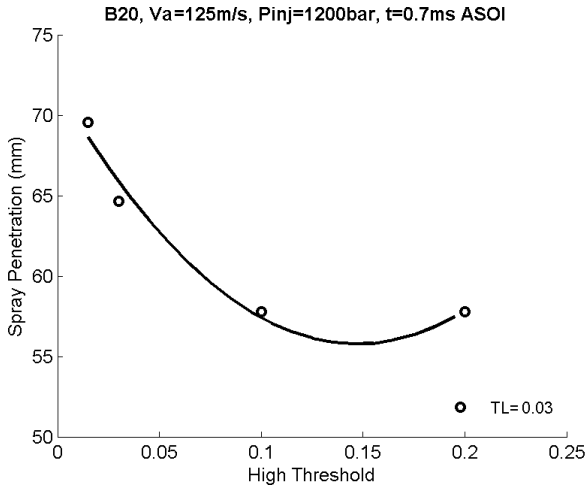

Figure 4.9: The sensitivity of the high threshold, T_H, in the MATLAB edge detection command

Chapter 5

Results and Discussion

5.1 Spray Development

This section will qualitatively show progressions of select averaged spray images between 0.4ms and 1.0ms after the start of injection and discuss the main visual differences in these images.

5.1.1 Effect of Injection Pressure

Figure 5.1 shows the effect of increasing the injection pressure from 1200 to 1500bar. Here, notable qualitative differences are difficult to distinguish. However, it is arguable that spray penetration lengths are longer for the 1500bar case; it is most obvious with the diesel fuel images. This is likely because the higher injection pressure provides the fuel with more kinetic energy to penetrate at a faster rate than at an injection pressure of 1200bar.

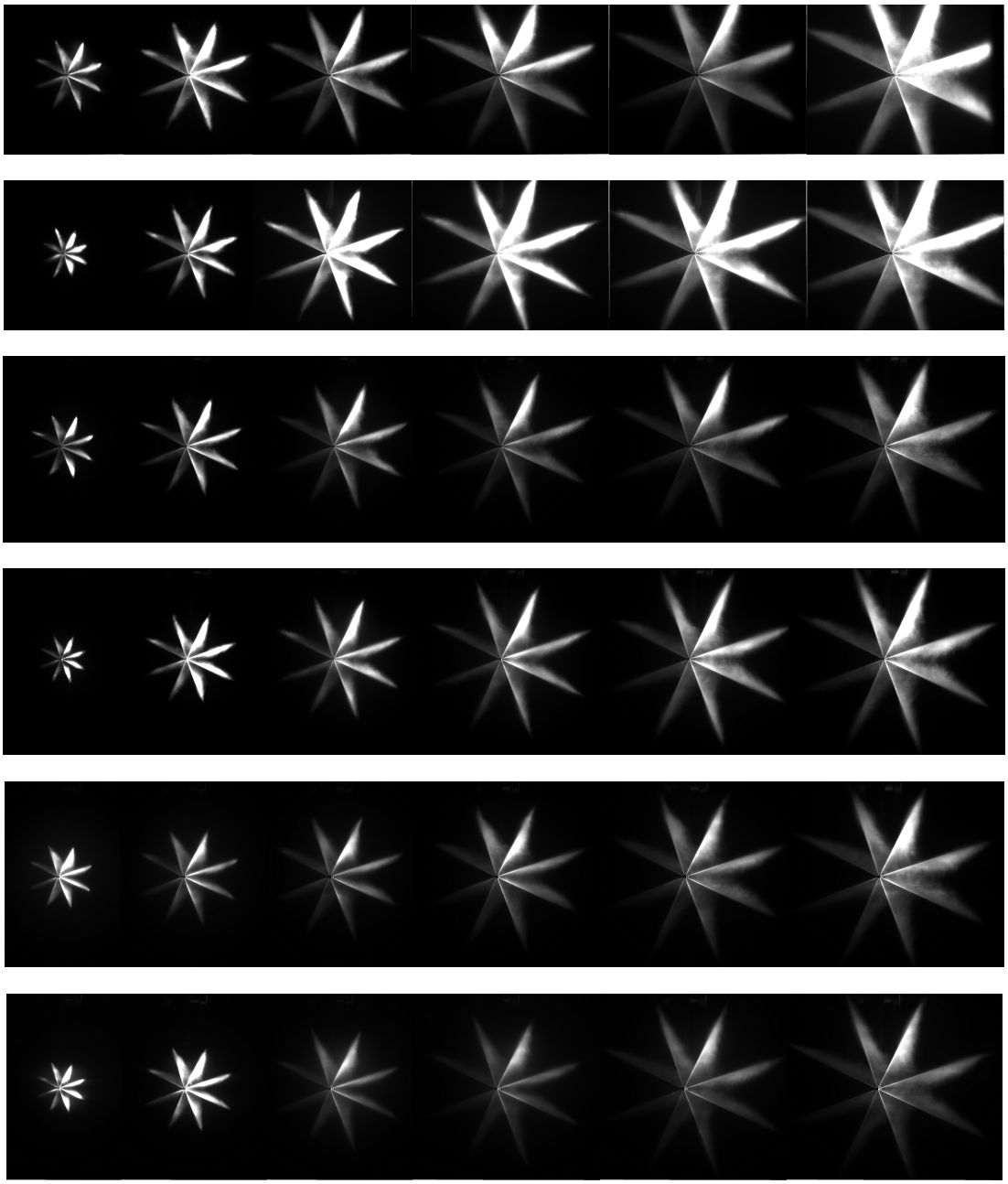

Figure 5.1: Averaged spray images at x/D=10, V_a=91m/s from 0.5ms to 1.0ms (left to right, 0.1ms increments): D100, P_{inj}=1200bar (1^{st} row); D100, P_{inj}=1500bar (2^{nd} row); B20, P_{inj}=1200bar (3^{rd} row); B20, P_{inj}=1500bar (4^{th} row); B100, P_{inj}=1200bar (5^{th} row); B100, P_{inj}=1500bar (6^{th} row)

5.1.2 Effect of Cross Airflow Velocity

Figures 5.2 and 5.3 show the averaged spray images for D100 and B100 fuels at the four jet centerline cross airflow velocities: 0m/s, 49.3m/s, 125.0, and 213.7m/s. The images show very dense liquid columns of fuel transitioning to wide and bent plumes as the cross airflow velocity is increased from V_a=0m/s to V_a=213.7m/s. These images demonstrate how cross airflows acting on a fuel spray help to atomize the droplets for more efficient combustion, by dispersing and deflecting the fuel droplets away from the dense liquid core. Moreover, spray penetration lengths decrease with increasing cross airflow velocities. Since the fuel droplets are being deflected early in the spray development, they are unable to penetrate as far into the surrounding air as they would in a quiescent environment.

5.1.3 Effect of Fuel Type

A more meticulous investigation of Figure 5.1 show that the width of the D100 plumes are larger than those of B20 and B100. This is likely a result of diesel exhibiting lower surface tension, providing less resistance to the formation of new droplets. These additional droplets are more easily deflected by the cross air flow, and thus more quickly dispersed into the cross air flow direction than in the case with biodiesel fuel. In addition, the biodiesel plumes appear to be longer than the diesel plumes (Figures 5.2 and 5.3). This is because biodiesel has a higher viscosity, so the droplets formed tend to be larger than the diesel droplets. The larger and heavier droplets have more momentum to penetrate further before being deflected by the cross air flow.

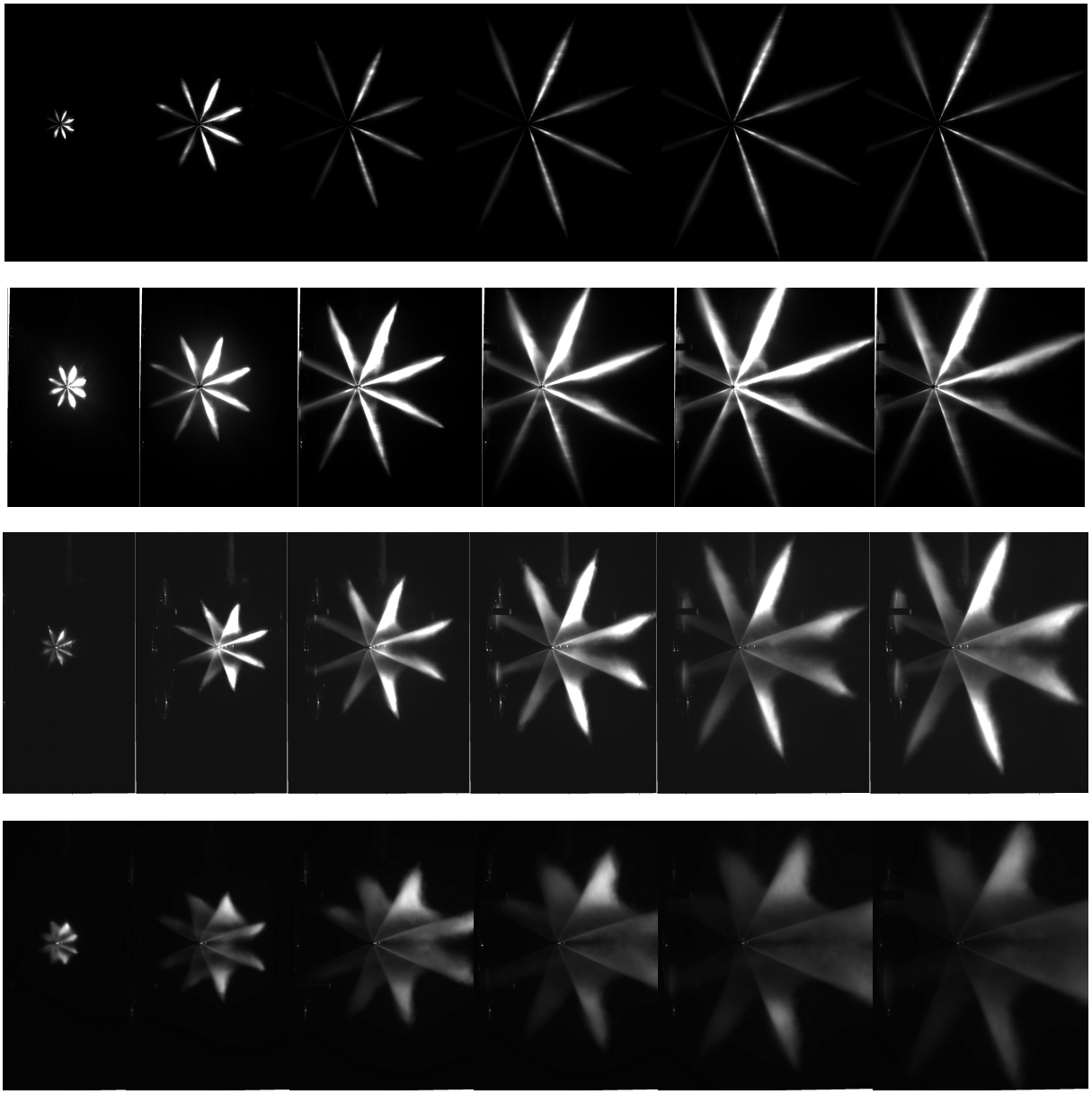

Figure 5.2: Averaged spray images for D100, x/D=1.5, P_{inj}=1200bar from 0.4ms to 0.9ms (left to right, 0.1ms increments): V_a=0m/s (1^{st} row), V_a=49.3m/s (2^{nd} row), V_a=125.0m/s (3^{rd} row), V_a=213.7m/s (4^{th} row).

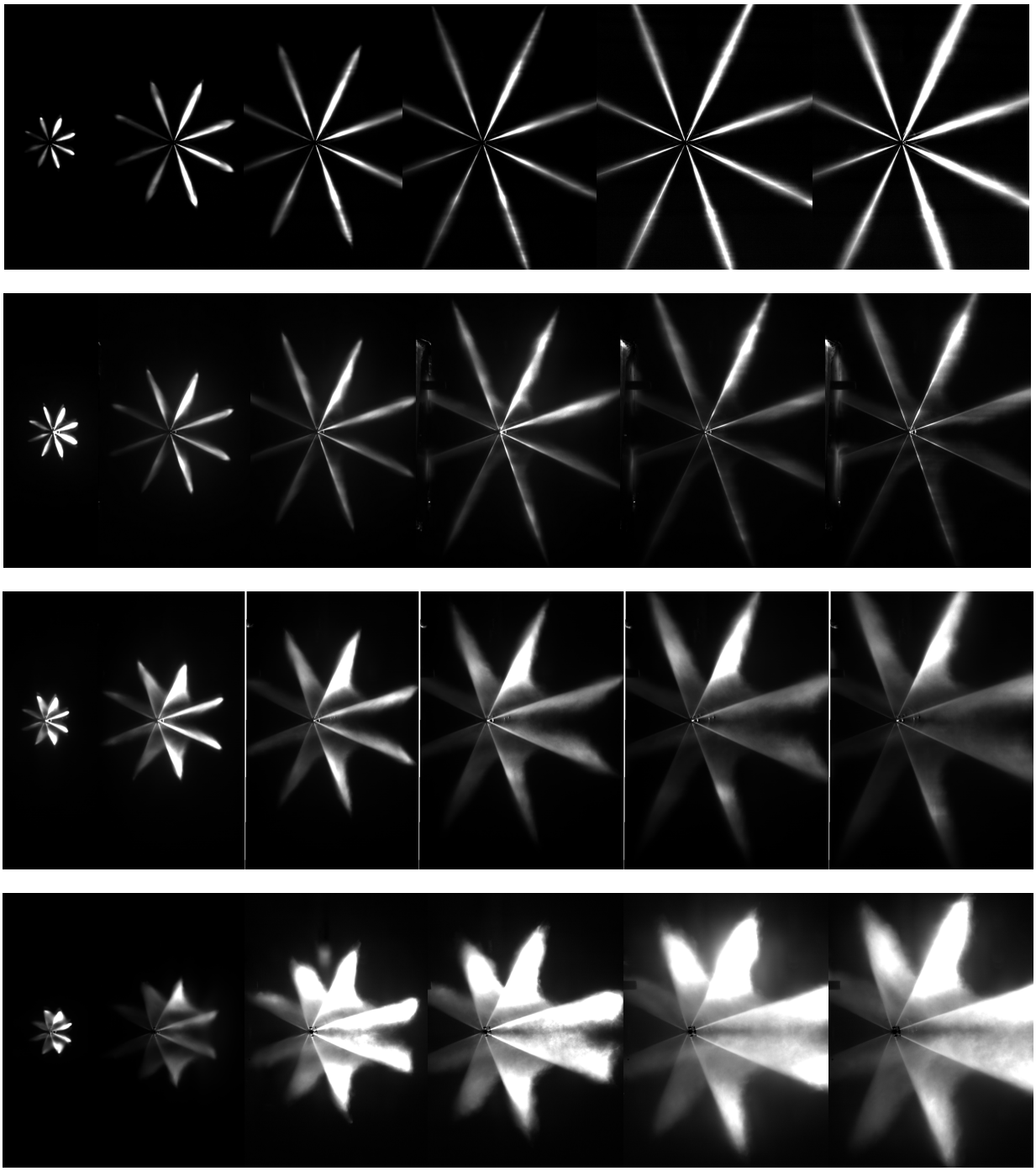

Figure 5.3: Averaged spray images for B100, x/D=1.5, P_{inj}=1200bar from 0.4ms to 0.9ms (left to right, 0.1ms increments): V_a=0m/s (1^{st} row), V_a=49.3m/s (2^{nd} row), V_a=125.0m/s (3^{rd} row), V_a=213.7m/s (4^{th} row).

5.2 Spray Penetration Curves

This section will discuss the spray penetration lengths calculated from MATLAB image processing and spray penetration curves created from MATLAB second order polynomial curve-fitting, providing a quantitative comparision of the sprays with respect to injection pressure, cross airflow velocity, and the type of fuel used.

Due to the fact that the injector is positioned such that it is symmetrical about the x-axis, Plumes 1 to 4 essentially respond to the experimental conditions almost identically to Plumes 5 through 8. This is illustrated in Figure 5.4, which shows the location of the plumes with respect to each other and to the cross airflow.

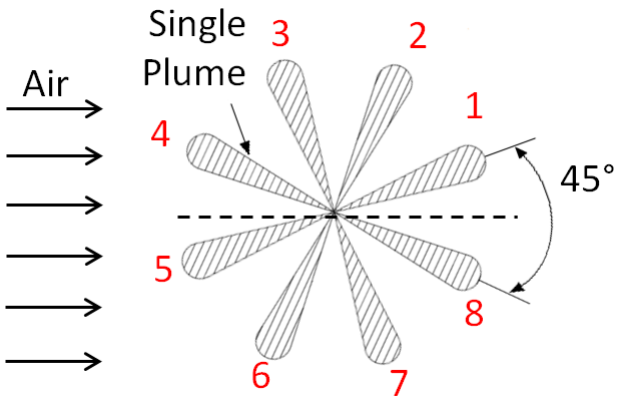

Figure 5.4: Plume numbering and relative location to other plumes and air jet

Because the air jet is positioned parallel to the x-axis and blown in the positive x-direction, Plumes 1, 2, 7 and 8 have a co-flow component together with the cross flow, whereas Plumes 3, 4, 5, and 6 have a counter-flow component. These varying degrees of co-flow and counter-flow components may explain some of the observations found in the spray penetration and axis deflection curves.

Sample spray penetration curves for Plumes 1 to 4 and Plumes 5 to 8 are shown in Figure 5.5. Qualitatively, the curves look very similar. Table 5.1 quantifies the difference in spray penetration between symmetric plumes in all four crossflow velocities at the same injection pressure, time step, and x-location. The magnitude of the percent difference fall between

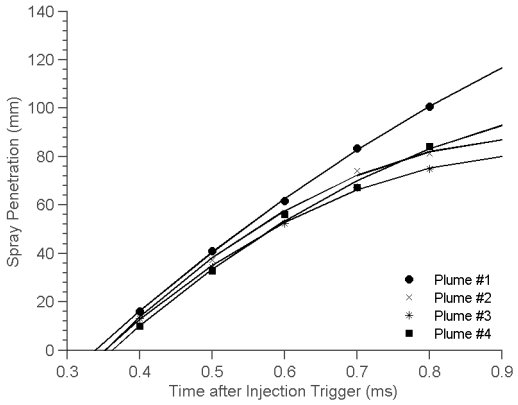

(a) Plumes 1 to 4

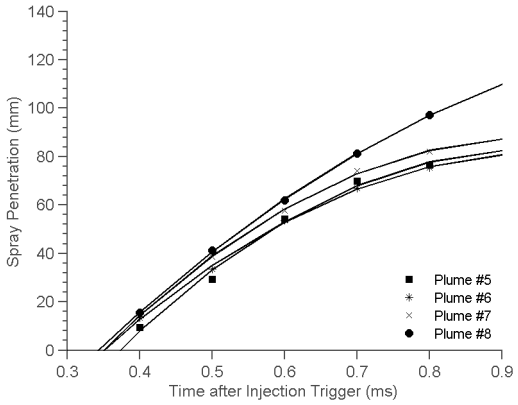

(b) Plumes 5 to 8

Figure 5.5: Axisymmetricity of Plumes 1 to 4 and Plumes 5 to 8 are evident from spray penetration curves

1% and 26%. The highest percentages correspond to the plumes that have a counter-flow component combined with the highest crossflow velocities (the most chaotic flow). For simplicity, the discussion of spray penetration and axis deflection will be limited to Plumes 1 through 4.

Table 5.1: Percent difference in spray penetration for symmetric diesel plumes at P_{inj}=1200 bar, 0.8ms ASOI, x/D=1.5.

	V_a (m/s)	Plume 8	Plume 7	Plume 6	Plume 5
Plume 1	0.0	4%	-	-	-
	49.3	6%	-	-	-
	125.0	5%	-	-	-
	213.7	11%	-	-	-
Plume 2	0.0	-	8%	-	-
	49.3	-	11%	-	-
	125.0	-	3%	-	-
	213.7	-	12%	-	-
Plume 3	0.0	-	-	6%	-
	49.3	-	-	15%	-
	125.0	-	-	1%	-
	213.7	-	-	26%	-
Plume 4	0.0	-	-	-	8%
	49.3	-	-	-	22%
	125.0	-	-	-	3%
	213.7	-	-	-	13%

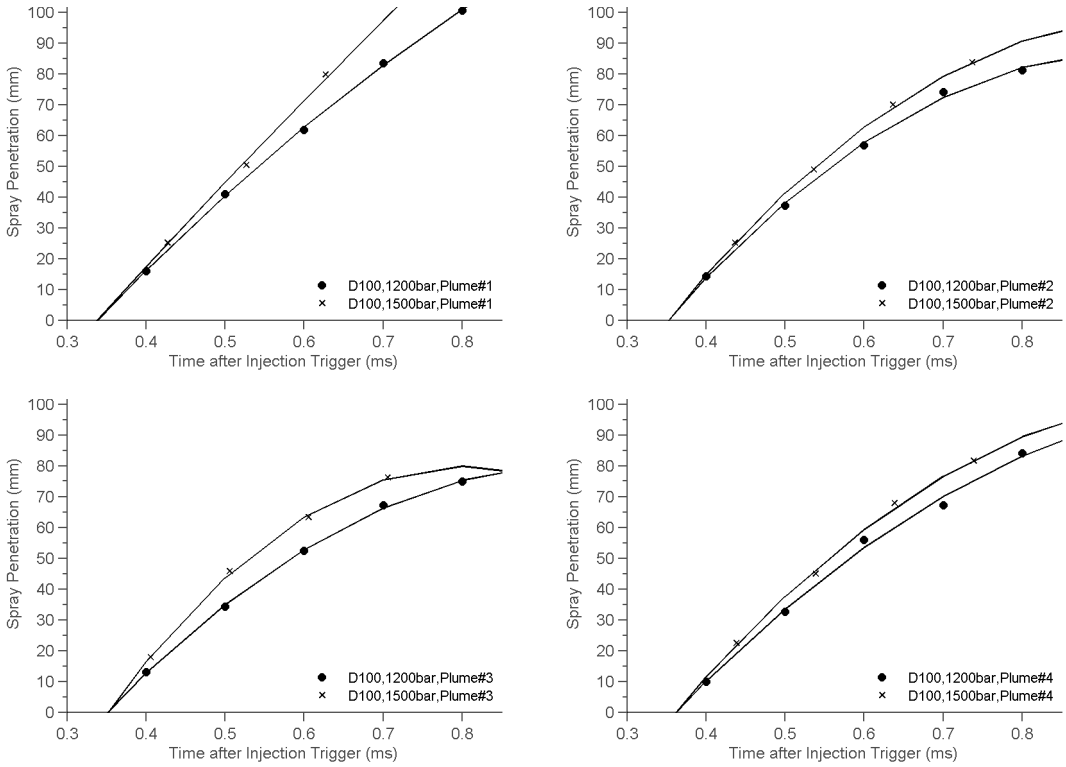

Figure 5.6: Effect of injection pressure on D100 spray penetration at x/D=10, V_a=125.0m/s

5.2.1 Effect of Injection Pressure

Figures 5.6 to 5.8 show the spray penetration curves for Plumes 1 to 4 for all three fuel types. The percentage change in spray penetration length with respect to injection pressure is summarized in Table 5.2. Spray penetration lengths show an increase between 4% to 15% with an increase in injection pressure from 1200bar to 1500bar. For all plumes except Plume 4, which has the strongest counter-flow component, the percent increase in spray penetration is greatest for D100, likely due to the low viscosity and higher momentum the fuel has to penetrate further. The reverse trend is observed for Plume 4, where the highest percent difference is observed for B100, possibly because the bigger and heavier fuel droplets are able to carry further against the air flow compared to the diesel.

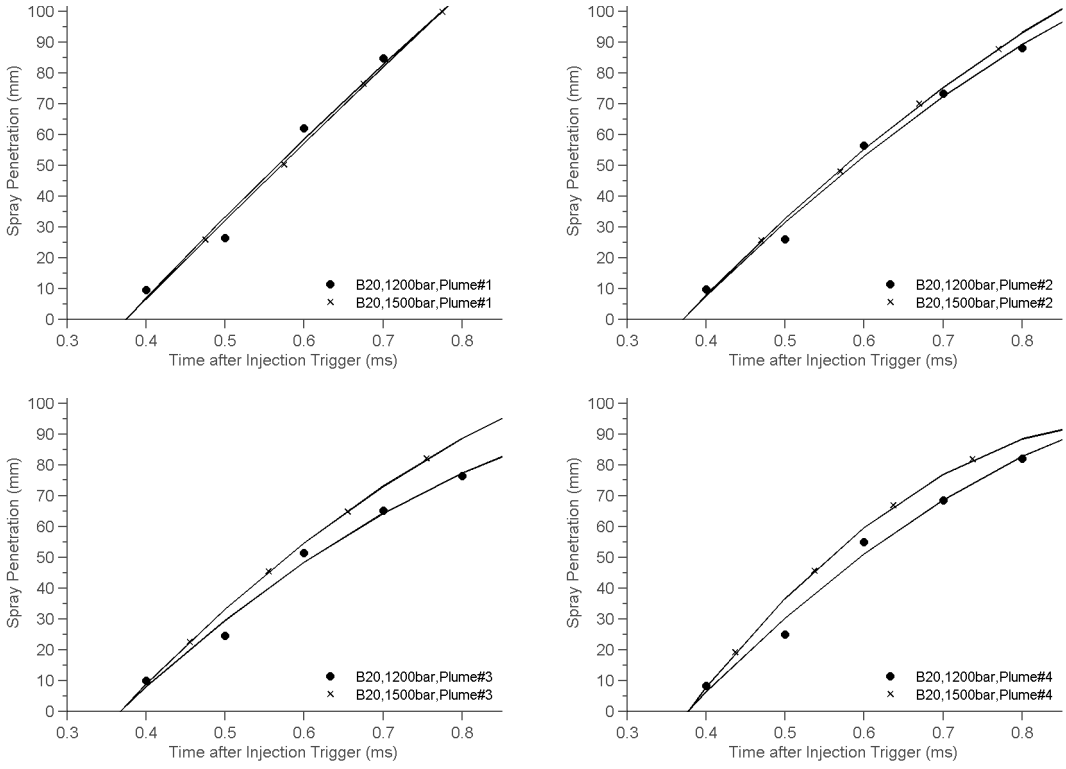

Figure 5.7: Effect of injection pressure on B20 spray penetration at x/D=10, V_a=125.0m/s

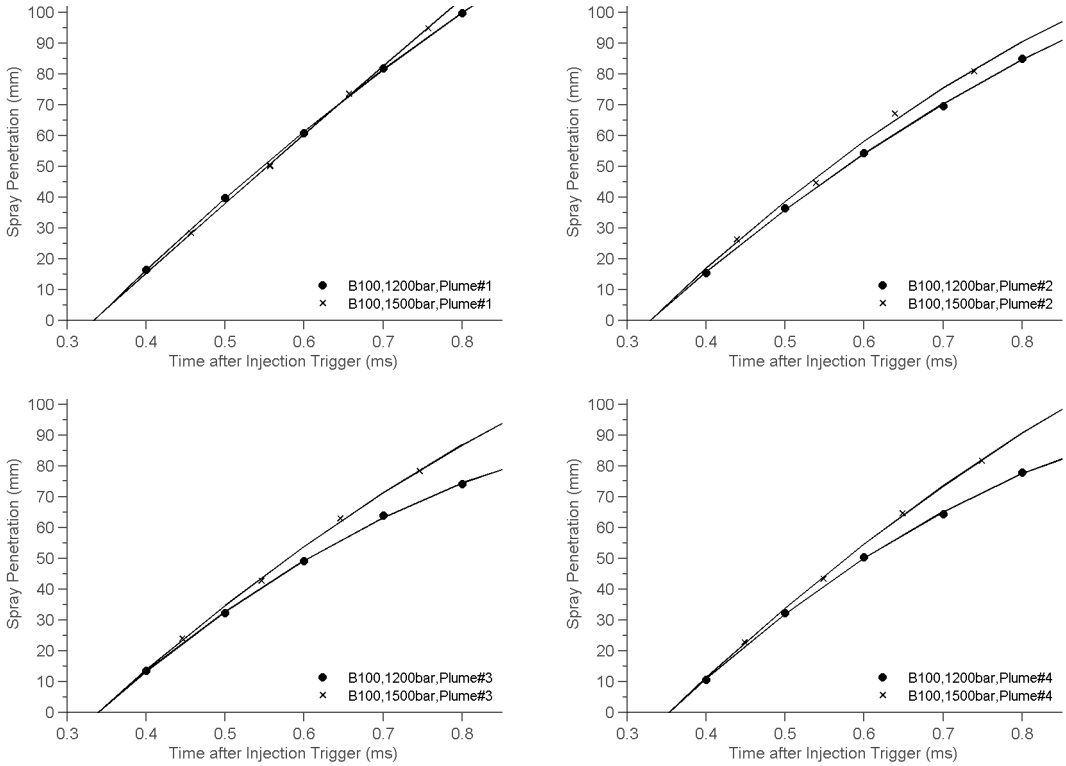

Figure 5.8: Effect of injection pressure on B100 spray penetration at x/D=10, V_a=125.0m/s

Table 5.2: Spray penetration for sprays with varying injection pressure at x/D=10, V_a=125.0m/s, 0.7ms ASOI

	Fuel	1200bar	1500bar	% Difference in S
Plume 1	D100	82.7mm	94.2mm	14%
	B20	82.6mm	94.8mm	15%
	B100	81.3mm	84.2mm	4%
Plume 2	D100	72.2mm	79.2mm	10%
	B20	72.2mm	75.2mm	4%
	B100	70.3mm	75.3mm	7%
Plume 3	D100	66.2mm	75.4mm	14%
	B20	64.2mm	73.0mm	14%
	B100	63.2mm	71.1mm	13%
Plume 4	D100	70.0mm	76.5mm	9%
	B20	68.4mm	76.9mm	12%
	B100	65.1mm	73.4mm	13%

5.2.2 Effect of Cross Airflow Velocity

Figures 5.9 to 5.11 show the effect of cross airflow velocity on spray penetration length for several plumes and all fuel types. Table 5.3 summarizes percentage difference in spray penetration at 0.7ms ASOI between the quiescent condition and the three crossflow velocities. Both the spray penetration curves and the percentage difference table show the consistent trend of decreasing spray penetration length (up to a 44% decrease) with increasing cross flow velocity. For some cases at V_a=0m/s and early in the spray progression (i.e. t<0.7ms ASOI), the spray progression lags that of the sprays with a cross flow, which is contrary to what would be expected since quiescent sprays have the least deflection. This phenomenon is worthy of further investigation.

Table 5.3: Spray penetration for sprays with varying crossflow velocities at x/D=1.5, 0.7ms ASOI

	Fuel	0m/s	49.3m/s	125.0m/s	213.7m/s
Plume 1	D100	56.4mm	3%	-4%	2%
	B20	84.4mm	0%	-6%	-3%
	B100	78.0mm	13%	5%	3%
Plume 2	D100	77.0mm	0%	-17%	-28%
	B20	81.4mm	-3%	-12%	-18%
	B100	79.41mm	6%	-8%	-18%
Plume 3	D100	77.4mm	-15%	-28%	-44%
	B20	83.0mm	-4%	-24%	-40%
	B100	77.9mm	4%	-18%	-39%

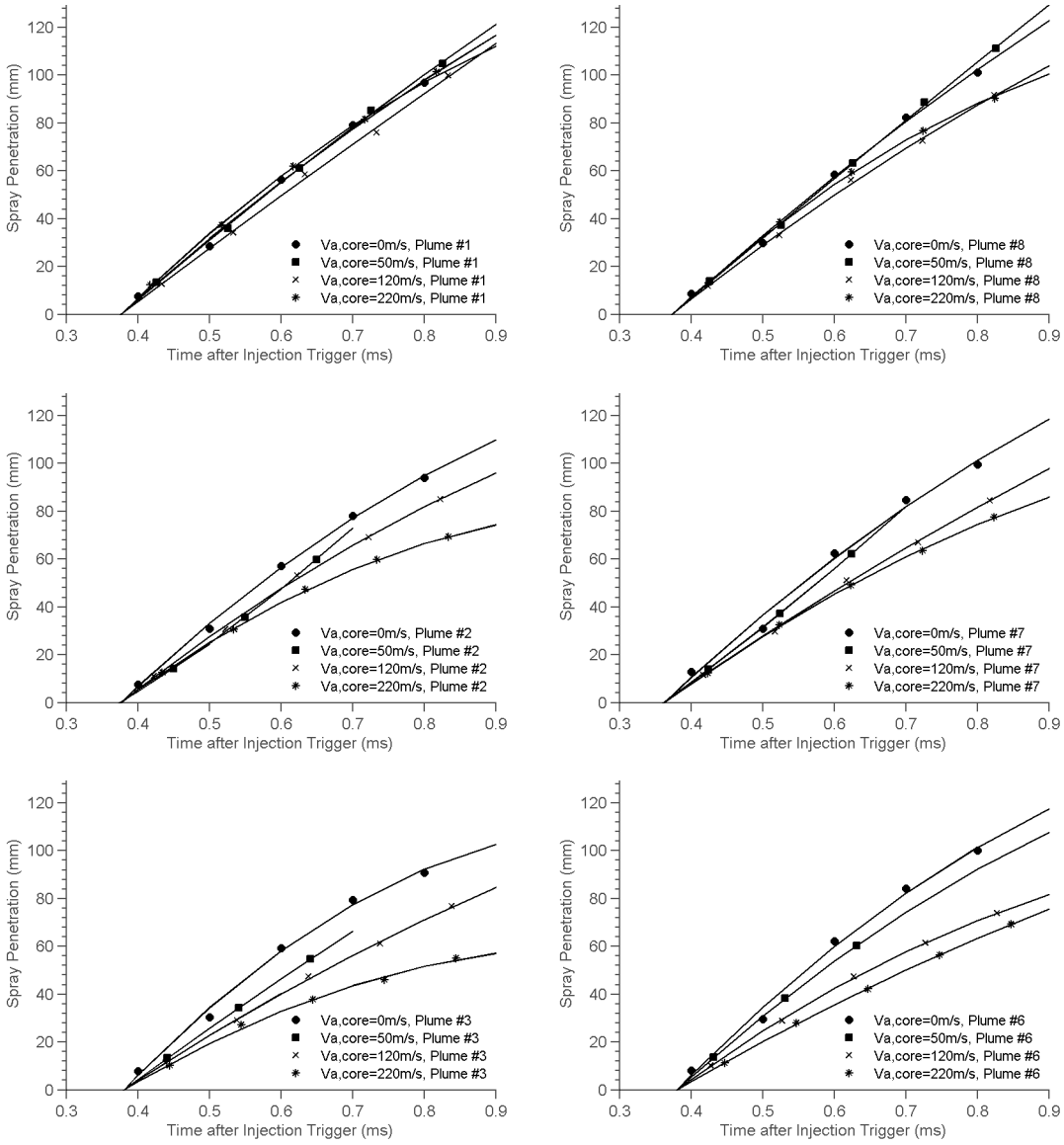

Figure 5.9: Effect of cross airflow velocity on D100 spray penetration at P_{inj}=1200bar, x/D=1.5

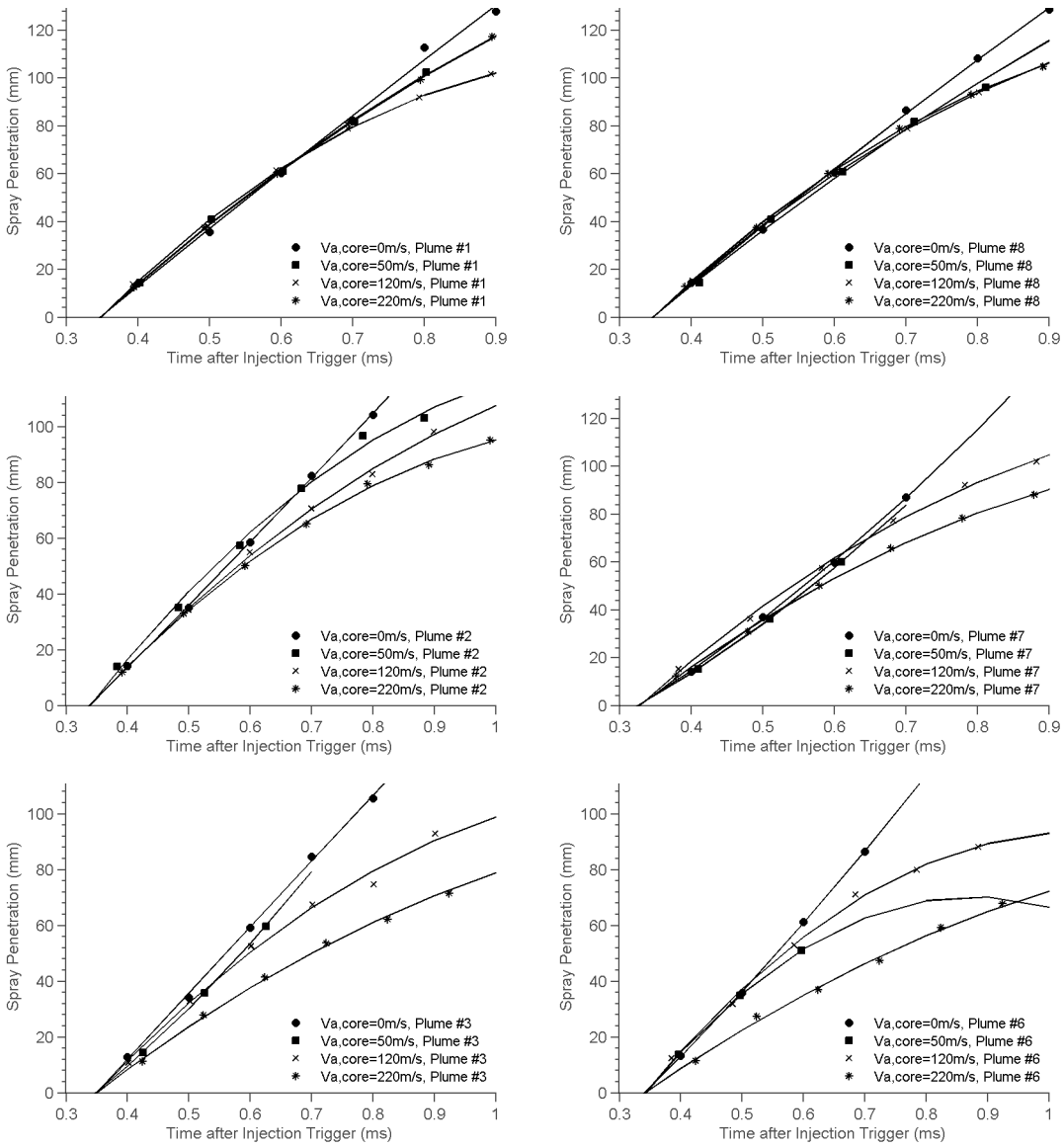

Figure 5.10: Effect of cross airflow velocity on B20 spray penetration at P_{inj}=1200bar, x/D=1.5

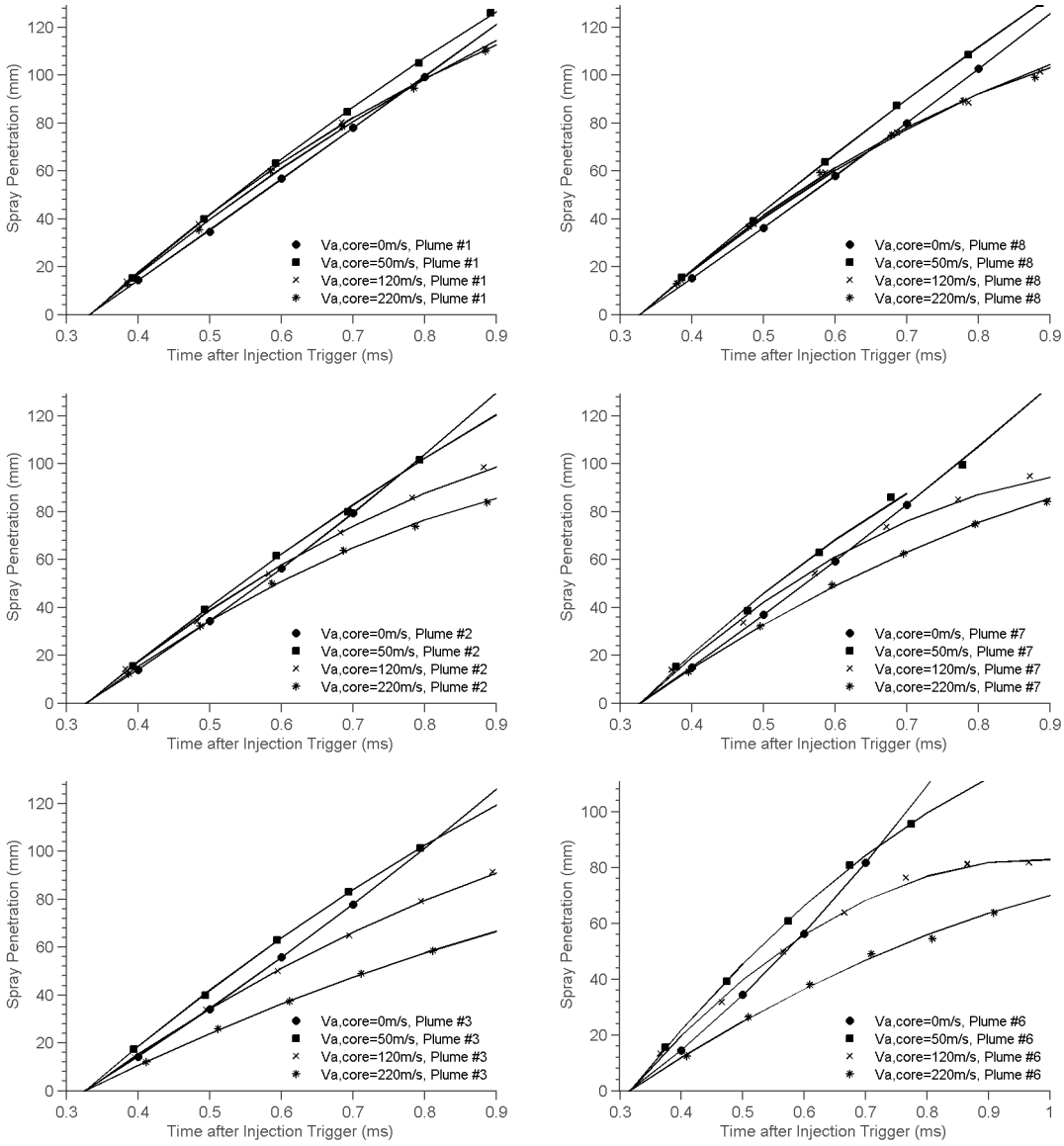

Figure 5.11: Effect of cross airflow velocity on B100 spray penetration at P_{inj}=1200bar, x/D=1.5

5.2.3 Effect of Fuel Type

Figures 5.12 shows the effect of fuel type on spray penetration lengths on Plumes 1 to 4 at 1200bar injection pressure and x/D=10. It is observed that for all four injector orientations the spray penetration in the early portion of the spray progression is highest for pure diesel fuel, followed by B20 and then B100. Once the spray progression reaches approximately 0.7ms ASOI, the axis deflection in the pure diesel fuel inhibits penetration of the fuel, allowing the penetration of the B20 to exceed that of pure diesel. This seems to be most visible in Plumes 2 and 3 where the crossflow component is highest. B100 penetrates at a much slower rate than the two lower viscosity fuels, but at the same time, is the least deflected of the three fuels. This is most likely a result of higher viscosity, which produces bigger droplets that require more energy to penetrate further. However, because of the bigger droplets having more momentum, B100 appears to exceed the penetration of B20 and D100 if the spray was allowed to progress beyond the 0.7ms ASOI. Ultimately, it can be concluded that higher viscosity fuels give longer spray penetrations but requires more time to achieve those penetrations compared to lower viscosity fuels. Table 5.4 summarizes the effect of fuel type on spray penetration. B20 has up to a 10% increase in spray penetration length. Spray penetration for B100 progresses slower due to the larger droplets and therefore has not reached its full length at 0.7ms ASOI. Consequently, when compared with D100 at 0.7ms ASOI, it lags in spray penetration by 3% to 9%.

Table 5.4: Spray penetration for sprays with varying fuel types at x/D=10, V_a=91m/s, 0.7ms ASOI

	D100	B20	B100
Plume 1	82.7mm	10%	-3%
Plume 2	72.2mm	5%	-7%
Plume 3	66.2mm	1%	-7%
Plume 4	70.0mm	1%	-9%

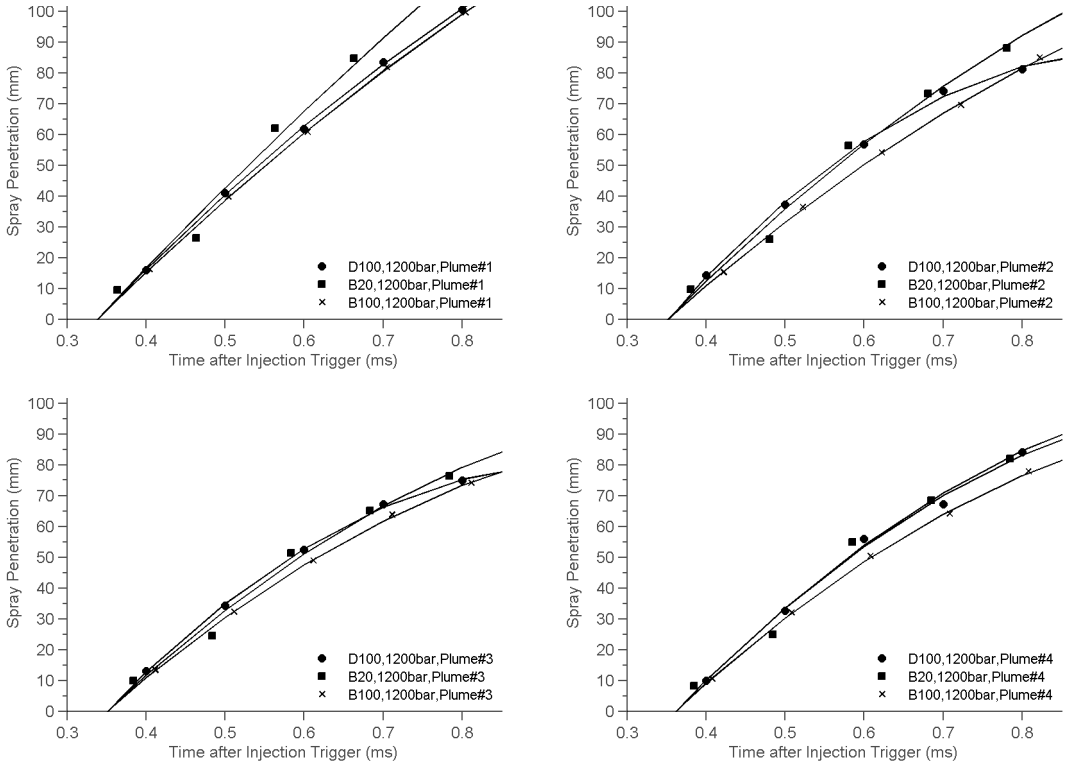

Figure 5.12: Effect of fuel type on spray penetration: x/D=10, V_a=91m/s

5.2.4 Model Comparison

As discussed in Chapter 2, the Hiroyasu correlation was developed for quiescent environment sprays, whereas the Wu and Inamura correlations were developed for sprays with an orthogonally positioned cross airflow. This section will compare the experimental results with the calculated spray penetration curves from the correlations to see their accuracy and applicability. Momentum ratios were estimated using $V_f = Cd \cdot \sqrt{\frac{2 \cdot (P_{inj} - P_{amb})}{\rho_f}}$ for fuel velocity and air densities corrected for air jet outlet temperatures. Assuming non-cavitating sprays the discharge coefficient, Cd, was set to 0.8 for all calculations. [49]

The cross flow correlations for spray penetration lengths were obtained by taking the x-component of the spray penetration length measured from the experimental data in MATLAB, calculating for the y-component, and then using $S = \int_{t=0}^{t} \sqrt{(1 + (dy/dx)^2)} dx$ to find the arc length of the spray curve produced from the x-y points. Figure 5.13 shows the experimental and calculated spray penetration curves calculated for Plume 1. Evidently, the quiescent correlation fits well with the experimental data. The quiescent correlation slightly under-predicts the experimental data for all cross flow velocities, especially during the early portion of the spray progression. On the contrary, the cross flow correlations differ drastically for all fuels and all cross flow velocities. The calculated penetration lengths are much longer and show very strong axis deflection angles. Due to the correlations being developed for perpendicular cross flows and much lower momentum ratios, they predict much different spray behaviours. The momentum ratios that these correlations were tested in were less than 100, whereas the experiments conducted in this study were in the order of 20,000. To the best of this study's knowledge, there is no correlation in a comparable momentum flux ratio range.

Figure 5.14 and 5.15 show the experimental and calculated spray penetration curves for Plume 2 and 3. Compared to the results from Plume 1, the correlations here fit much better, especially in the highest cross airflow velocity. The quiescent correlation begins to over-predict the spray penetration lengths at the later portions of the spray progression, as should be expected since there is no axis deflection involved in the quiescent environment. The cross flow correlations still over-predict the spray penetration lengths during the early portion of the spray progression, but are much closer to the experimental data. Plume 2

and 3 have a much bigger perpendicular cross flow component compared to Plume 1, which explains the better fit. Plume 4 was not compared because the impingment of the spray on the air nozzle face made the penetration curves too short to make any conclusions.

These results illustrate the effect of the angle of injection with respect to the cross flow has on the overal spray penetration length. This is one variable that has not been modelled extensively in spray correlation literature.

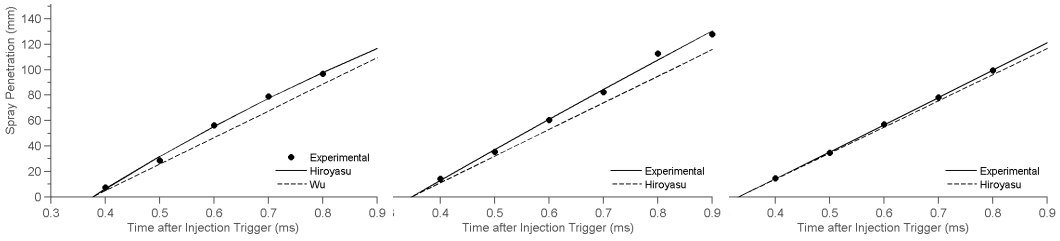

(a) D100, V_a=0m/s (b) B20, V_a=0m/s (c) B100, V_a=0m/s

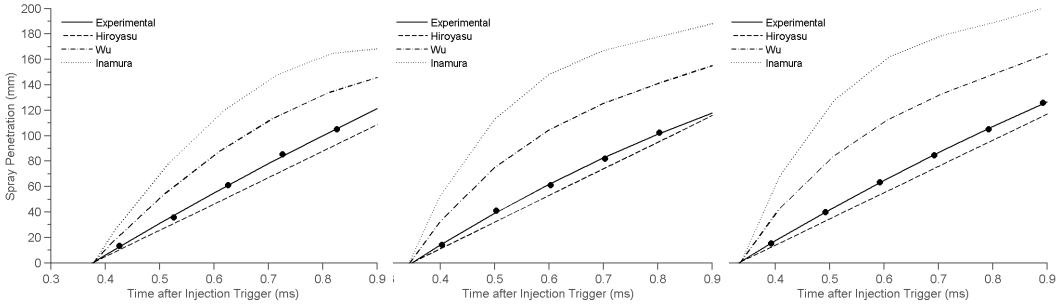

(d) D100, V_a=49.3m/s (e) B20, V_a=49.3m/s (f) B100, V_a=49.3m/s

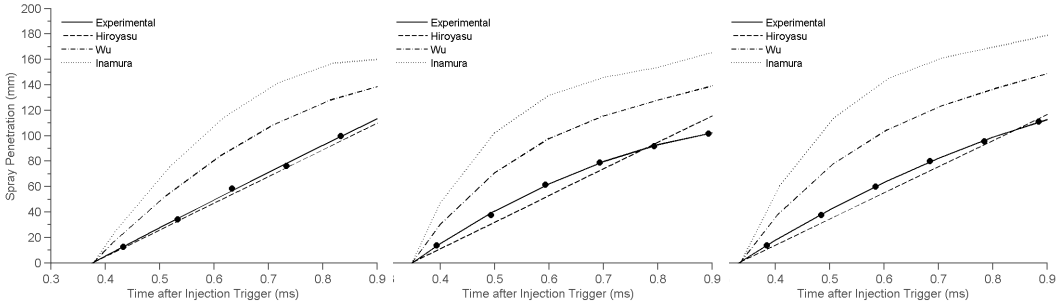

(g) D100, V_a=125.0m/s (h) B20, V_a=125.0m/s (i) B100, V_a=125.0m/s

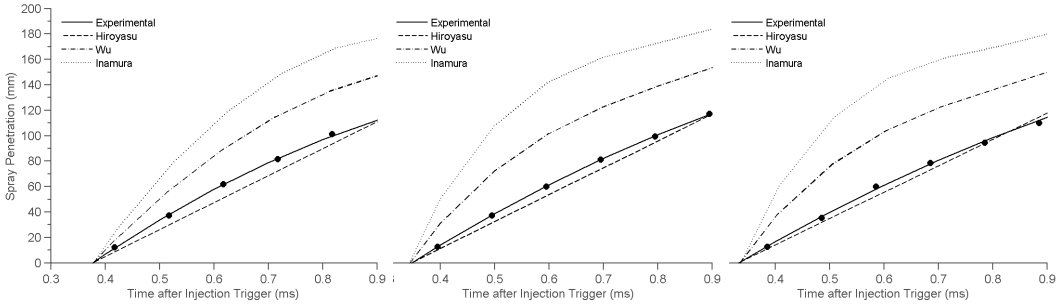

(j) D100, V_a=213.7m/s (k) B20, V_a=213.7m/s (l) B100, V_a=213.7m/s

Figure 5.13: Plume 1 spray penetration curves: P_{inj}=1200bar

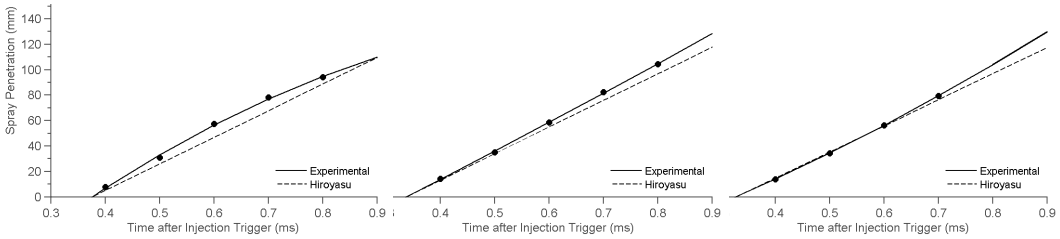

(a) D100, V_a=0m/s (b) B20, V_a=0m/s (c) B100, V_a=0m/s

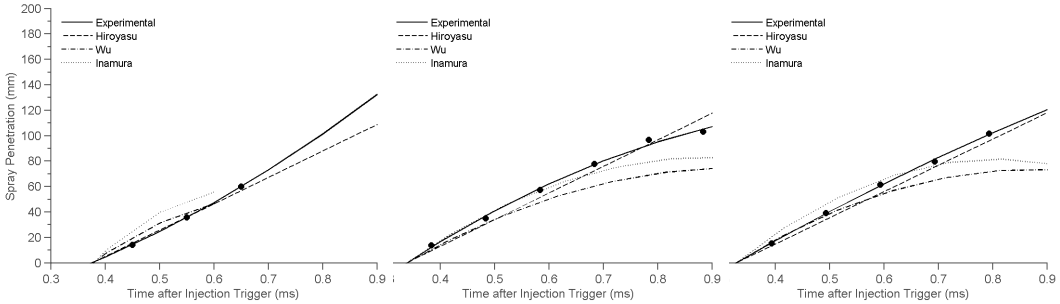

(d) D100, V_a=49.3m/s (e) B20, V_a=49.3m/s (f) B100, V_a=49.3m/s

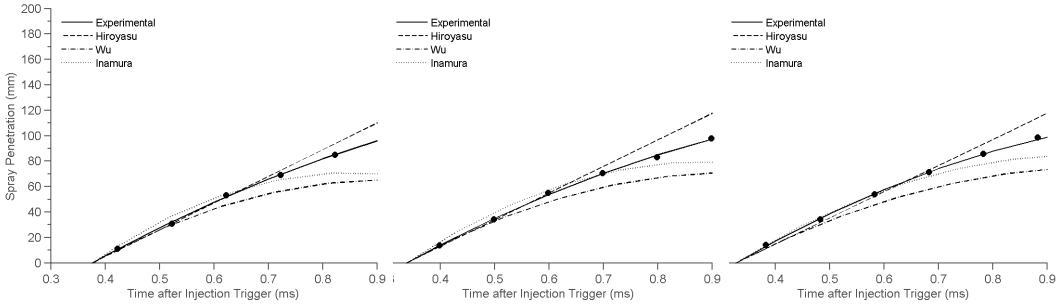

(g) D100, V_a=125.0m/s (h) B20, V_a=125.0m/s (i) B100, V_a=125.0m/s

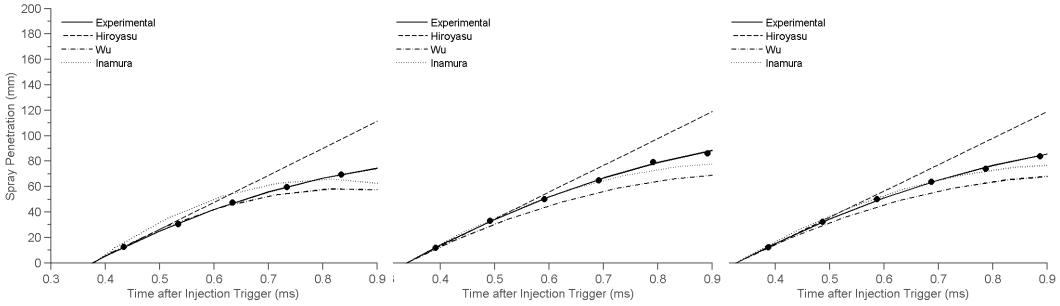

(j) D100, V_a=213.7m/s (k) B20, V_a=213.7m/s (l) B100, V_a=213.7m/s

Figure 5.14: Plume 2 spray penetration curves: P_{inj}=1200bar

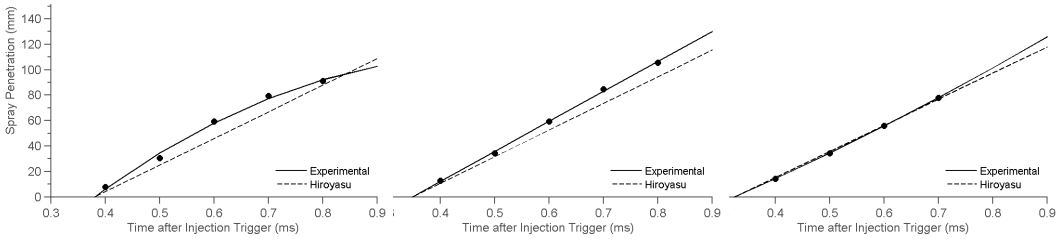

(a) D100, V_a=0m/s (b) B20, V_a=0m/s (c) B100, V_a=0m/s

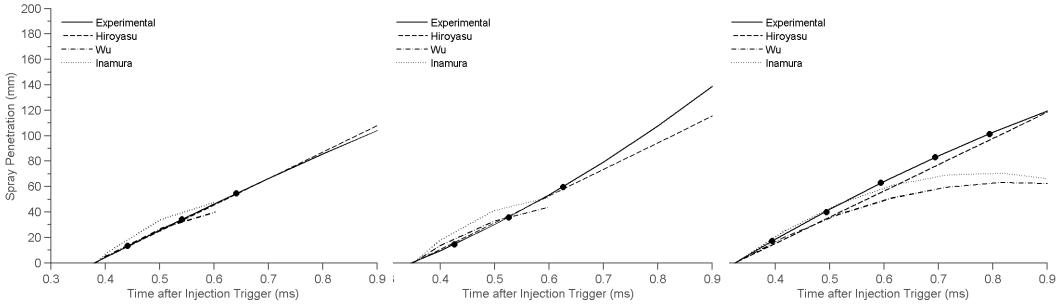

(d) D100, V_a=49.3m/s (e) B20, V_a=49.3m/s (f) B100, V_a=49.3m/s

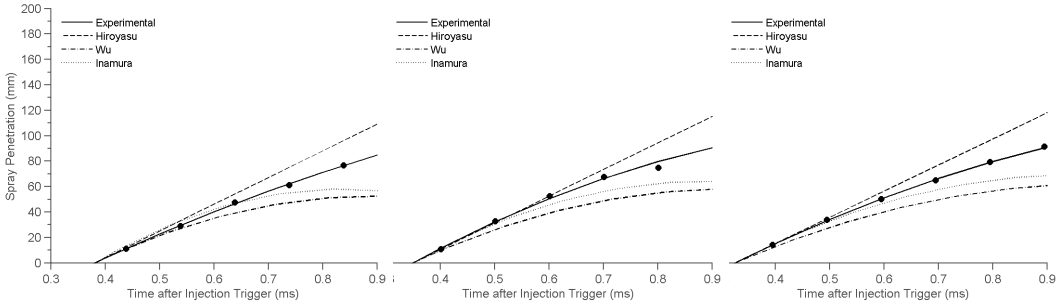

(g) D100, V_a=125.0m/s (h) B20, V_a=125.0m/s (i) B10, V_a=125.0m/s

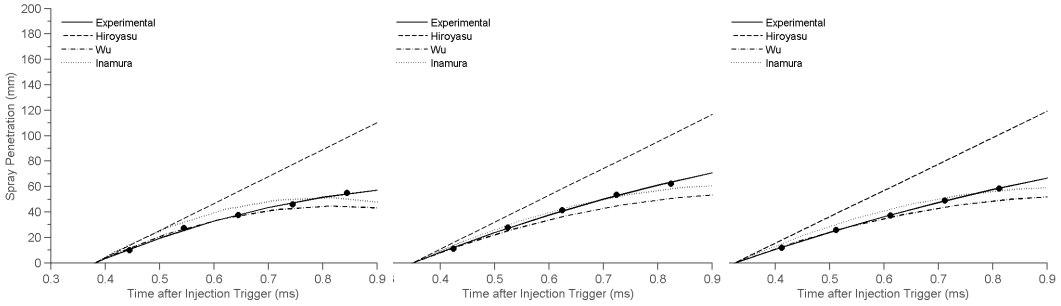

(j) D100, V_a=213.7m/s (k) B20, V_a=213.7m/s (l) B100, V_a=213.7m/s

Figure 5.15: Plume 3 spray penetration curves: P_{inj}=1200bar

5.3 Axis Deflection Curves

This section will discuss axis deflection angles calculated from MATLAB image processing and axis deflection angle progression curves created from MATLAB second order polynomial curve-fitting.

5.3.1 Effect of Injection Pressure

Figures 5.16 to 5.18 show the effect of injection pressure on the axis deflection angle for Plumes 1 through 4 and all fuel types. There does not appear to be a consistent trend for axis deflection with respect to injection pressures. For example, in Figure 5.18, B100 Plume 3 axis deflection angle for injection pressure of 1200bar is higher than that for injection pressure of 1500bar, whereas the opposite is observed for Plume 4. What these graphs reveal instead is that plume location plays a bigger role in the axis deflection angle. On average, Plume 1 has a linear axis deflection angle over the course of the spray progression. On the contrary, Plumes 2 and 3 have a decreasing axis deflection angle as it progresses from 0.4ms to 0.8ms. Lastly, Plume 4 shows little to no decrease in axis deflection angle over the progression. These observations are likely a result of the magnitude of cross flow, co-flow, and counter-flow components on the individual plumes. Plumes 2 and 3 have strong cross flow components compared to Plumes 1 and 4. Plumes 1 and 2 have a co-flow component and have similar axis deflection angles for spray past 0.5ms after the start of injection. Likewise Plumes 3 and 4 have a counter-flow component and show similar axis deflection angles in the later portion of the spray progression. The percent difference in axis deflection angles are shown in Table 5.5 at the instantaneous time step of 0.7ms. Negative values indicate a deflection in the negative direction on a polar coordinate system relative to the injector axis.

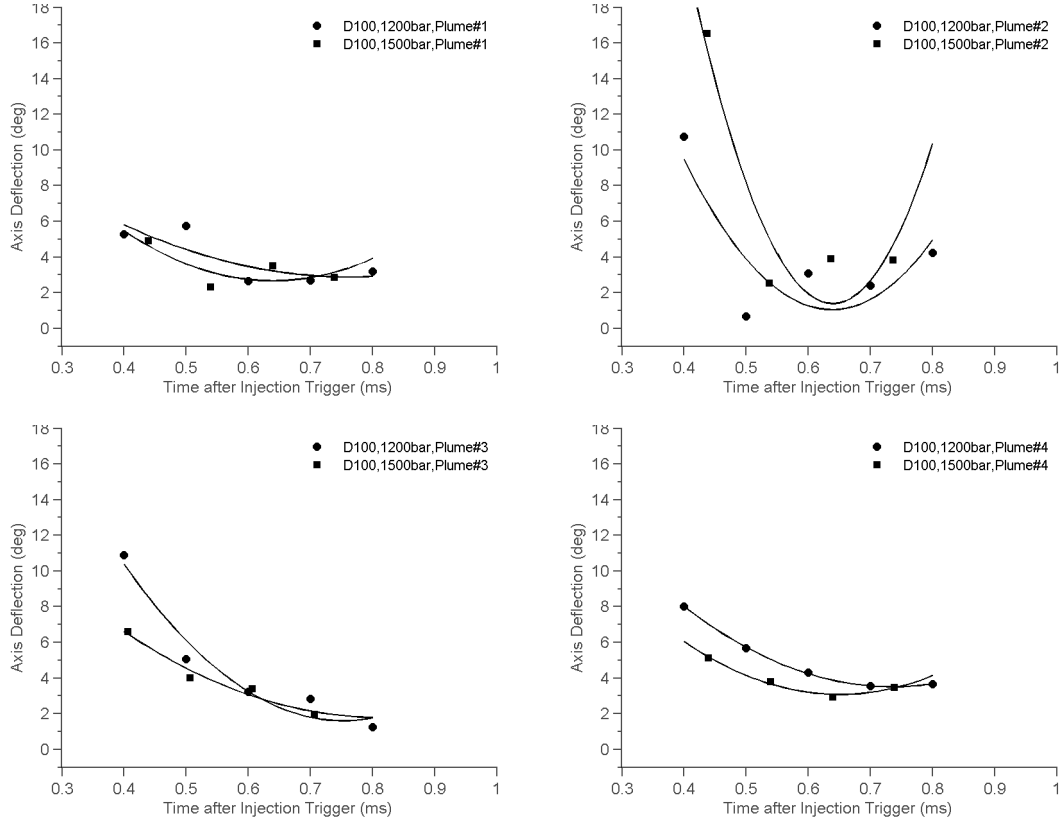

Figure 5.16: Effect of injection pressure on D100 axis deflection at x/D=10, V_a=125.0m/s

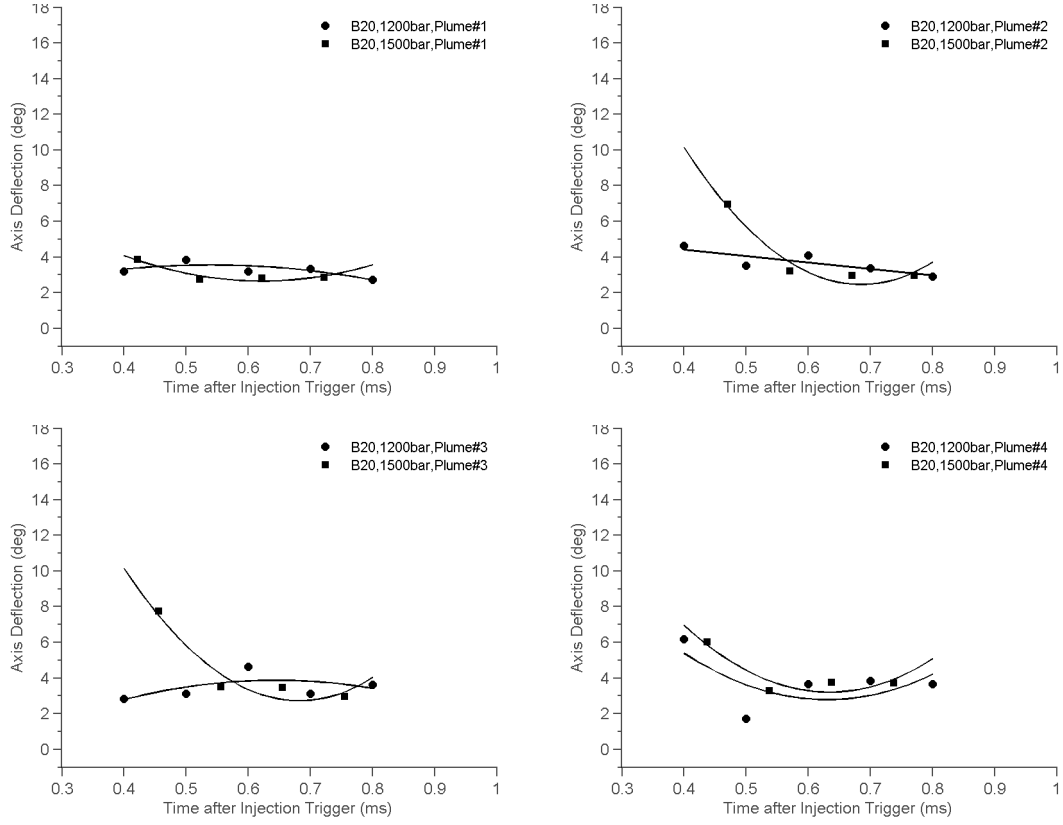

Figure 5.17: Effect of injection pressure on B20 axis deflection at x/D=10, V_a=125.0m/s

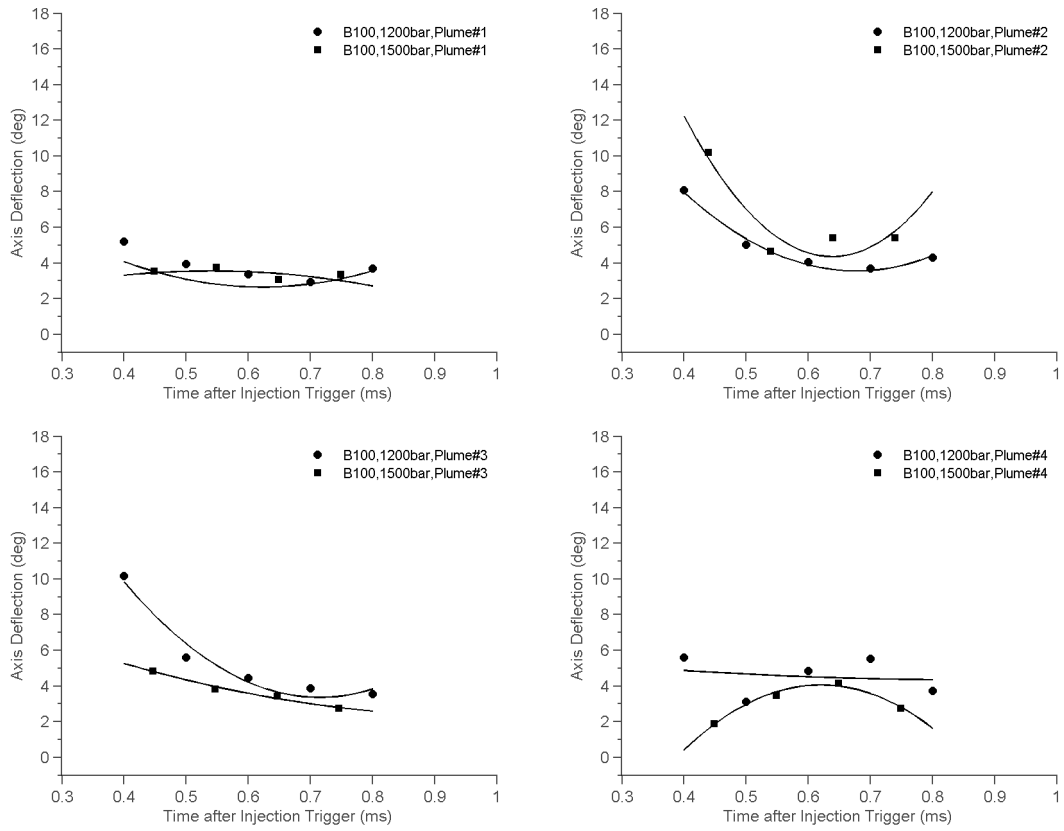

Figure 5.18: Effect of injection pressure on B100 axis deflection at x/D=10, V_a=125.0m/s

Table 5.5: Axis deflection for sprays with varying injection pressures at x/D=10, V_a=125.0m/s, 0.7ms ASOI

	Fuel	1200bar	1500bar	% Difference in θ_{def}
Plume 1	D100	3.0deg	2.8deg	-4%
	B20	3.2deg	2.8deg	-13%
	B100	3.1deg	3.3deg	6%
Plume 2	D100	1.6deg	2.7deg	65%
	B20	3.3deg	2.5deg	-26%
	B100	3.6deg	4.9deg	36%
Plume 3	D100	1.8deg	2.1deg	20%
	B20	3.8deg	2.8deg	-28%
	B100	3.4deg	3.0deg	-11%
Plume 4	D100	3.6deg	3.2deg	-10%
	B20	3.0deg	3.2deg	-10%
	B100	4.4deg	3.6deg	-19%

5.3.2 Effect of Cross Airflow Velocity

Figures 5.19 to 5.21 show the effect of cross airflow velocity on the axis deflection angle for several plumes and all fuel types. Across all three fuels, it is evident that an increase in crossflow velocity increases the axis deflection angle. Another trend observed from the curve-fitting is that axis deflection is high during the start of the spray progression, then drops to a minimum sometime between 0.6ms and 0.7ms ASOI, and then increases again after 0.7ms ASOI. This infers that the spray boundary changes shape between the time the spray emerges from the injector and when it penetrates through the airstream, and again when the cross airflow begins to interact with the spray droplets. Table 5.6 quantifies the effect of cross flow velocity on axis deflection at the instantaneous time step of 0.7ms ASOI and confirms findings from previous chapters that spray penetration lengths increase exponentially with the increase of cross airflow velocity, regardless of fuel type and plume. The highest deflection observed was for Plume 1 using B20 fuel, with a difference of deflection between the ambient condition and a crossflow velocity of 213.7m/s of 10.5°. Note that image processing and analysis of Plume 4 was not feasible for this experiment.

5.3.3 Effect of Fuel Type

Figure 5.22 show the effect of fuel type on the axis deflection for plumes 1 through 4. Similar to curves for effect of injection pressure on axis deflection, the curves here reveal more the effect of plume location than of fuel type. The curves for Plume 2 and 3 show the most drastic changes over the duration of the spray progression, with high axis deflection before 0.6ms ASOI, a drop to 2° or less around 0.6ms ASOI, and ending with a high axis deflection (4°+) after 0.7ms ASOI.

Table 5.7 summarizes the effect of fuel type on axis deflection at 0.7ms ASOI. It is evident that the increase in biodiesel content results in the increase in axis deflection regardless of plume. The highest axis deflection is consistent with the highest component of cross airflow (Plume 2) and the least deflection for the highest component of co-flow (Plume 1). Perhaps the higher viscosity and surface tension of biodiesel fuel allows spray droplets

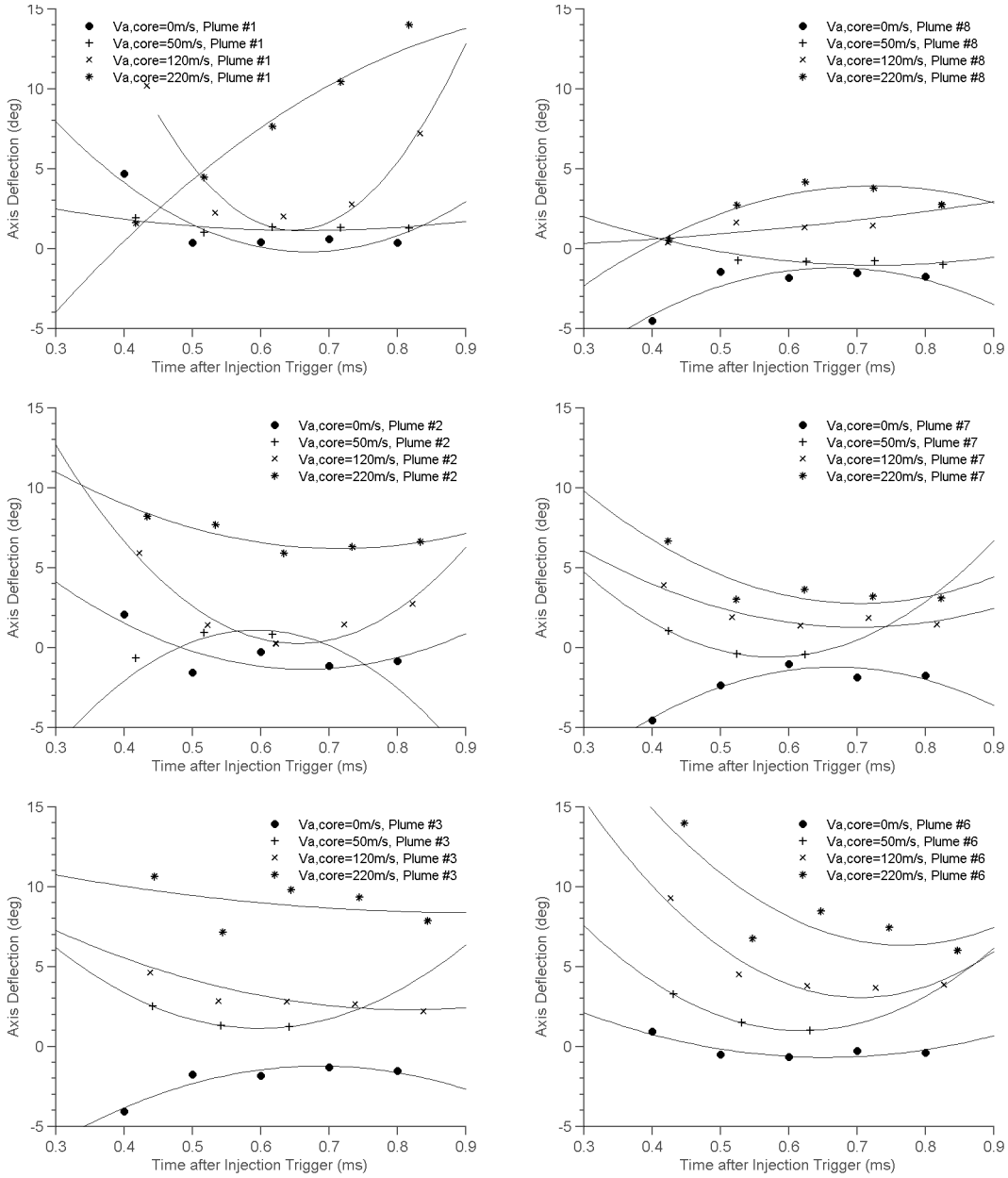

Figure 5.19: Effect of cross airflow velocity on D100 axis deflection at P_{inj}=1200bar, x/D=1.5

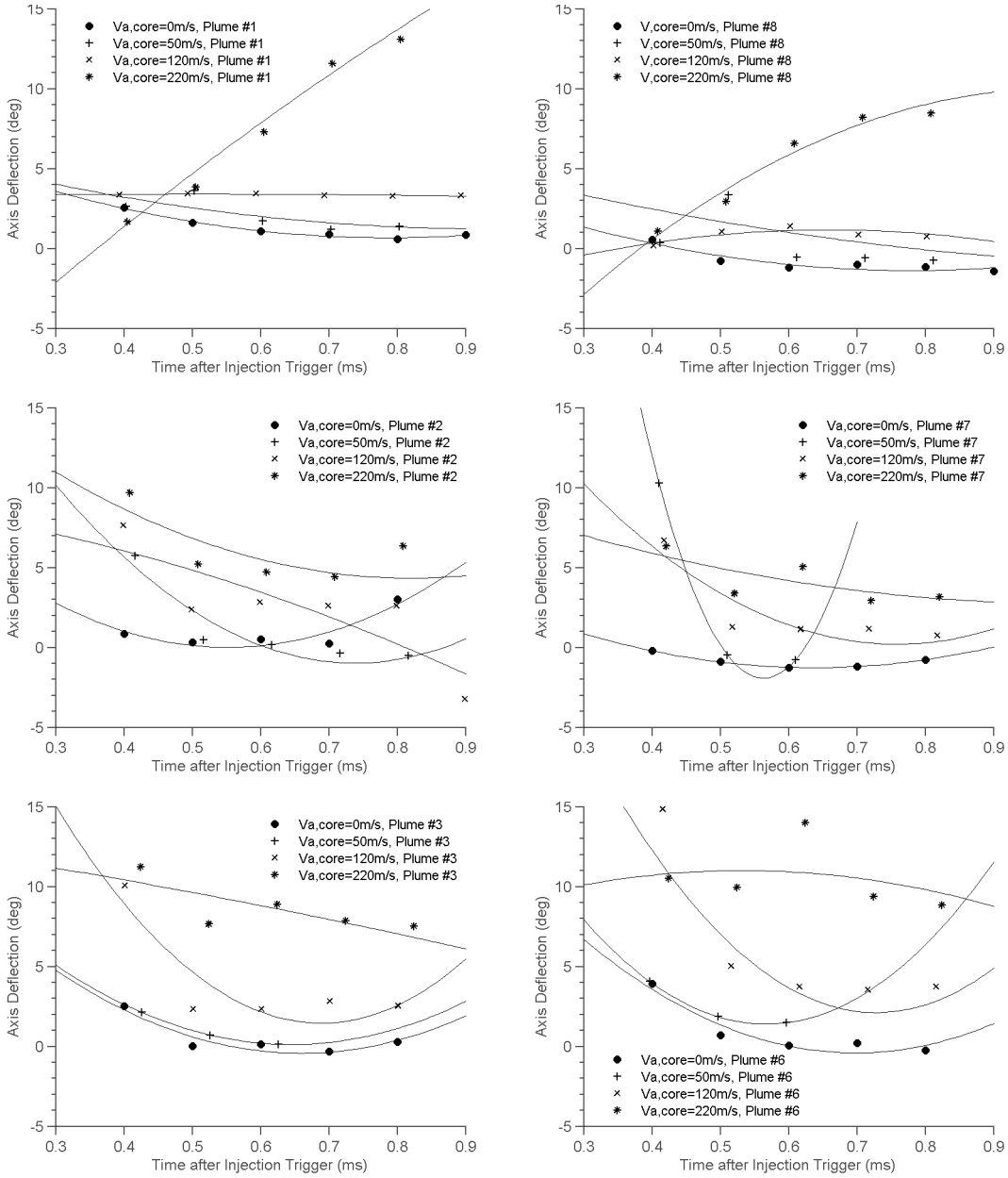

Figure 5.20: Effect of cross airflow velocity on B20 axis deflection at P_{inj}=1200bar, x/D=1.5

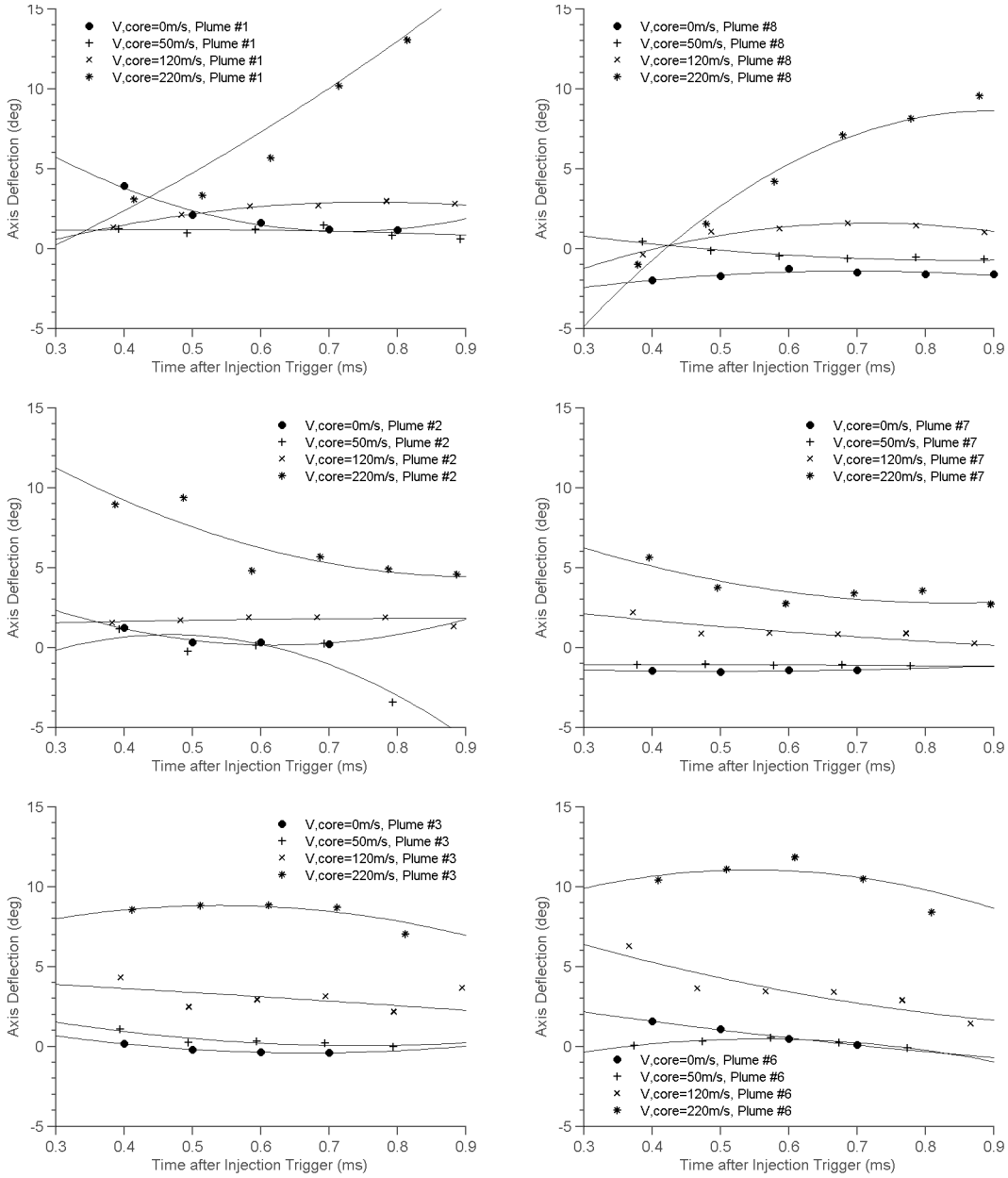

Figure 5.21: Effect of cross airflow velocity on B100 axis deflection at P_{inj}=1200bar, x/D=1.5

Table 5.6: Axis deflection for sprays with varying crossflow velocities at x/D=1.5, 0.7ms ASOI

	Fuel	0m/s	49.3m/s	125.0m/s	213.7m/s
Plume 1	D100	-0.2deg	1.1deg	1.6deg	10.2deg
	B20	0.8deg	1.7deg	3.5deg	11.3deg
	B100	1.1deg	1.1deg	2.9deg	10.1deg
Plume 2	D100	-1.3deg	0.1deg	0.5deg	6.1deg
	B20	1.0deg	-0.9deg	2.0deg	4.9deg
	B100	0.3deg	-1.1deg	2.0deg	5.7deg
Plume 3	D100	-1.2deg	1.7deg	2.5deg	8.5deg
	B20	-0.4deg	0.3deg	1.7deg	9.1deg
	B100	-0.4deg	0.1deg	2.9deg	8.6deg

dispersing from the core of the spray plume to continue in its natural path for a longer time before the cross airflow has any axis deflection effect. Therefore the axis deflection of B100 is larger than B20, which in turn is larger than D100, even though the spray penetration length is longest.

Table 5.7: Axis deflection for sprays with varying fuel types at x/D=10, V_a=91m/s, 0.7ms ASOI

	D100	B20	B100
Plume 1	3.0 deg	4%	5%
Plume 2	1.6 deg	102%	120%
Plume 3	1.8 deg	110%	92%
Plume 4	3.6 deg	-12%	24%

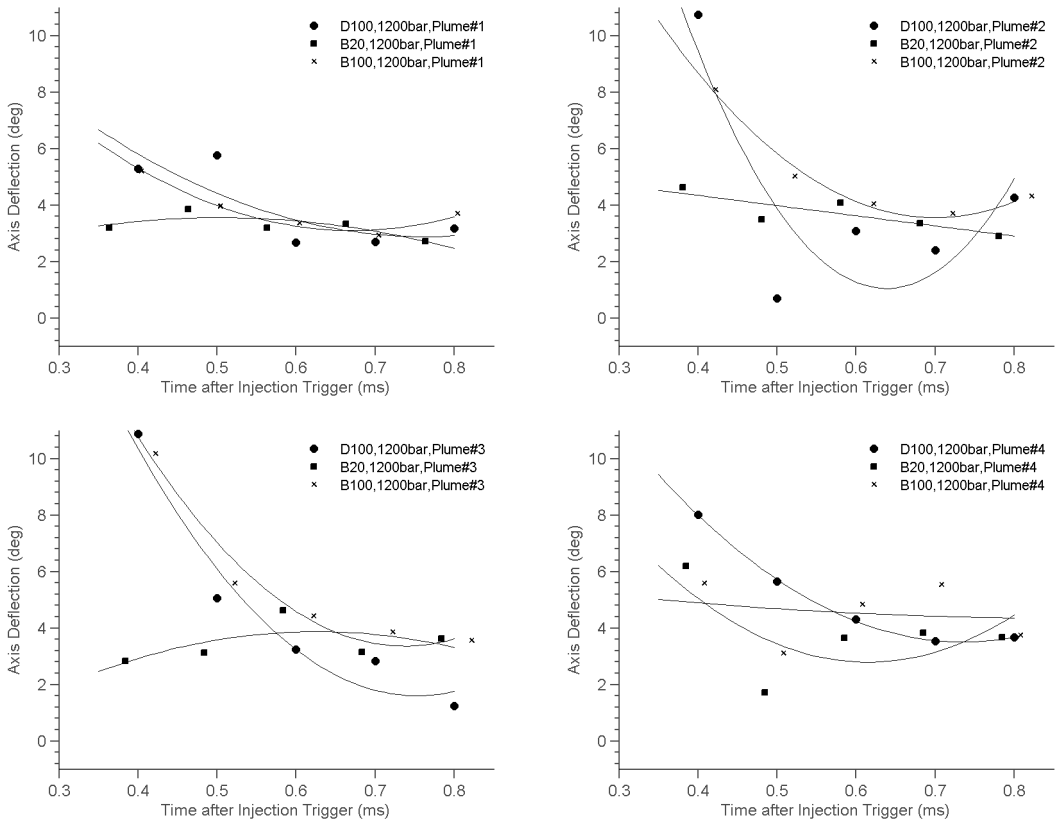

Figure 5.22: Effect of fuel type on axis deflection at x/D=10, V_a=91m/s

Chapter 6

Conclusion and Recommendations

In this study, a wind tunnel enclosure equipped with high pressure fuel injection and high velocity air jet capabilities was constructed. The objective of this study is to qualitatively and quantitatively examine fuel spray characteristics in a cross airflow – an air-fuel interaction similar to that which occurs inside the cylinder of a direct injection engine. These results can provide insight on the applicability and accuracy of existing correlations for spray in cross airflow and the impact of biodiesel on fuel spray develoment.

Diesel, biodiesel, and a biodiesel-diesel blend were tested and compared with respect to spray penetration and axis deflection angles. Photographs of the spray development were captured using particle image velocimetry. Image processing was performed using MATLAB edge detection. The effect of cross airflow velocity, fuel injection pressure, and fuel type were quantified via curves produced for spray penetration and axis deflection versus time after start of injection.

Results show that the increase in fuel injection pressures from 1200bar to 1500bar can increase a spray's penetration length by up to 15% without any observable effect on the axis deflection. For this reason, higher injection pressures have been used as a simple method of improving fuel distribution in automotive engines. It was also observed that with an increase of the cross airflow velocity by a factor of 4.3, spray penetration decreases by up to 44% and axis deflection increases by up to 66 times. In other words, by introducing cross

airflow, spray atomization and fuel combustion should improve. Crossflow correlations were most applicable for plumes that had high perpendicular crossflow components. With co-flow or counter-flow components, the existing correlations did not compare well. It was found that biodiesel's higher visocisty and surface tension increases spray penetration but decreases the rate at which penetration occurs. The larger and heavier biodiesel fuel droplets are less easily dispersed or deflected by the crossflow and have more momentum to penetrate further, but ultimately take longer for the same degree of fuel-air mixing. This utimately hinders spray atomization and is less desirable in combustion.

For future work, it is recommended to repeat the spray experiments where the fuel injector is in the potential core region of the jet but with the same jet centerline velocity as those measured in the fully-developed region. This will allow for an additional study on the effect of flow regime on spray characteristics. Spray correlations in cross flow can also be improved to include the angle of injection with respect to the cross airflow jet axis. This is especially important when dealing with multi-hole fuel injectors because not all injection holes are manufactured perfectly and the interaction between the air and fuel inside an engine cylinder is not always perpendicular. It was observed that the difference in spray penetration for a predominately co-flow spray and predominately cross-flow spray can be up to 20%. Experiments should also be conducted in pure crossflow to more accurately compare with existing correlations. This experimental apparatus can also be used to test new and emerging alternative fuels.

Appendices

Appendix A

Orifice Internal Geometry

The internal geometry of the piezoelectric diesel injector was characterized using X-Ray images taken by Dr. Xianghui Xhao (xhxiao@aps.anl.gov) at the Argonne National Laboratory in Lemont, Illinois. The resolution of these X-Ray images is measured in voxels, also known as volumetric pixels. For these images, the isotropic voxel size is 2.2, such that a 1 voxel x 1 voxel x 1 voxel is equal to a 2.2μm x 2.2 μm by 2.2μm volume. In other words, each image is a "slice" of the injector profile along the axis of the injector. Images were taken at three locations. The first location was the injector tip with the injector pin removed, so that the orifice pattern is captured. Using ImageJ to stitch all the "slices" together, a 3D view of the internal geometry was created, as shown in Fig. A.1.

The orifice inlet and outlet diameters and the radial distance between the two were measured using ImageJ tools on the images that correspond to the centerline "slice" of the orifice, as seen in Fig. A.2. The fillet from the injector sac to the orifice inlet, also called the inlet rounding radius is shown in Fig. A.3. Using ImageJ again, the area of the circle that is tangent to this fillet was calculated to have an area of 6354.92μm^2. Therefore, the inlet rounding radius can be calculated as shown in Eq. A.1.

$$Radius_{inlet,rounding} = \sqrt{\frac{6354.92}{\pi}} = 44.976\mu m \approx 45\mu m \tag{A.1}$$

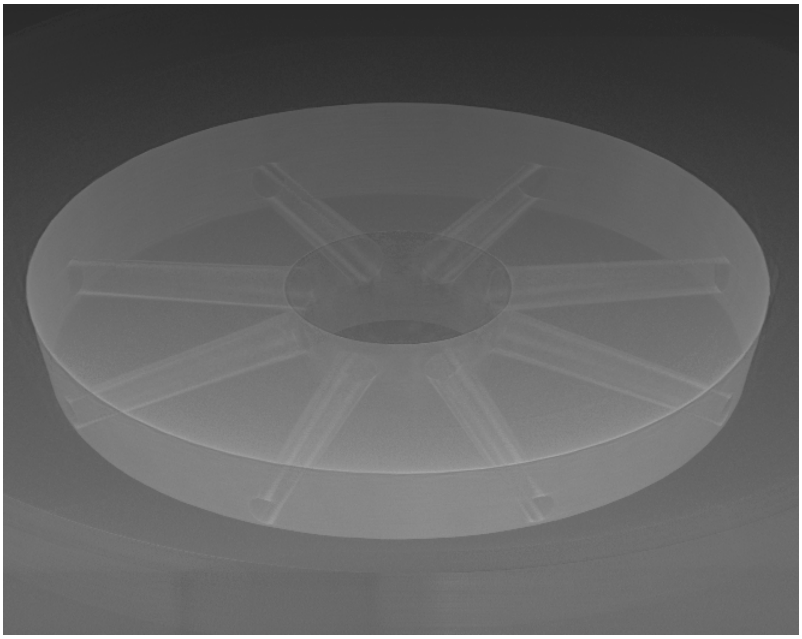

Figure A.1: 3D rendering of injector orifices

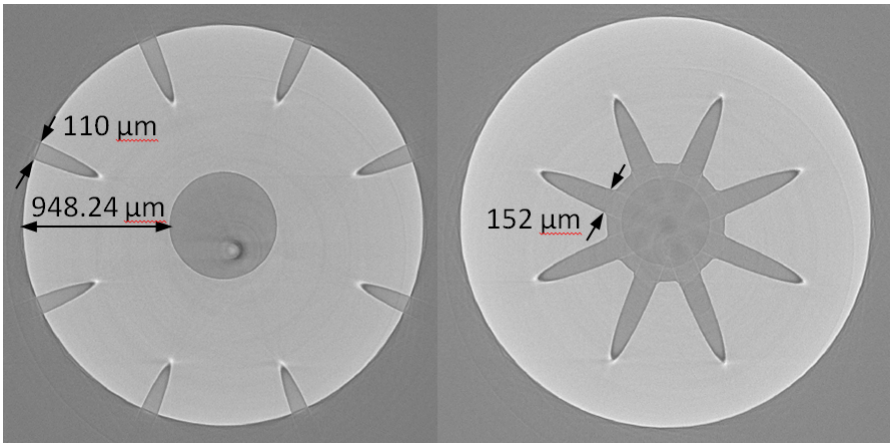

Figure A.2: Measurement of orifice inlet and oulet radii

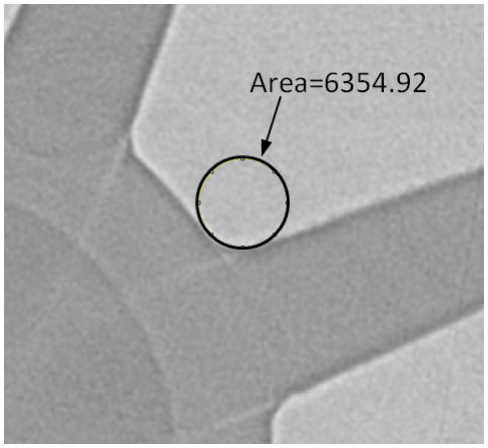

Figure A.3: Measurement of inlet rounding radius

Since there are 61 "slices" between the two images shown in Fig. A.2, the axial distance between the centerpoint of the inlet and centerpoint of the outlet can be calculated as shown in Eq. A.2.

$$\frac{2.2\mu m}{slice} * 61 slices = 134.2\mu m \tag{A.2}$$

Now the orifice tilt angle can be calculated as shown in Eq. A.3:

$$\theta_{o,tilt} = tan^{-1}\left(\frac{134.2\mu m}{948.24\mu m}\right) \approx 8^{\circ} \tag{A.3}$$

The conicity can also be calculated as follows (Eq. A.4):

$$Conicity = \frac{d_i - d_o}{10} = \frac{152\mu m - 110\mu m}{10} = 4.2\mu m \tag{A.4}$$

A schematic of the orifice internal geometry is shown in Fig. A.4.

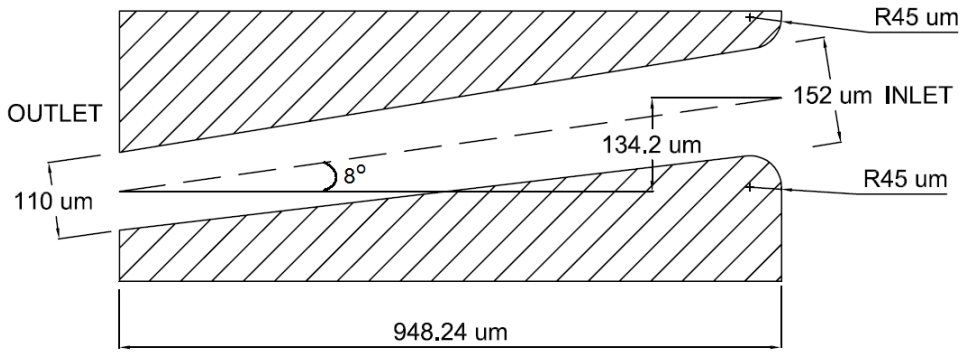

Figure A.4: Schematic of orifice geometry

Appendix B

Air Nozzle Design

The profile of the converging section can be expressed using the relationship shown in Eq. (**??**) and the definitions and parameter values are shown in Table B.1.

$$\frac{D - D_2}{D_1 - D_2} = 1 - \frac{1}{X^2}\left(\frac{x}{L}\right)^3 \qquad \frac{x}{L} \leq X \tag{B.1}$$

$$\frac{D - D_2}{D_1 - D_2} = \frac{1}{(1-x)^2}\left(1 - \frac{x}{L}\right)^3 \qquad \frac{x}{L} > X \tag{B.2}$$

Table B.1: Air Nozzle Dimensions

Parameter	**Value**	**Description**
D_1	9cm	Ø at x=0cm
D_2	2.5cm	Ø at x=7.65cm
X	0.60	Location where curves meet
x	0–7.65cm	Distance from entrance of converging section
L	7.65cm	Total length of converging section

Appendix C

Measurement Systems

C.1 Pressure Hardware Specifications

Table C.1: Kiel Probe Specifications

Specification	**Value**
Serial number	KAC-12
Material	Stainless steel
Supplier	United Sensor Corporation
Probe Diameter	1/8”
Yaw Range	±52°
Pitch Range	+47°,-40°
Time Constant	36s

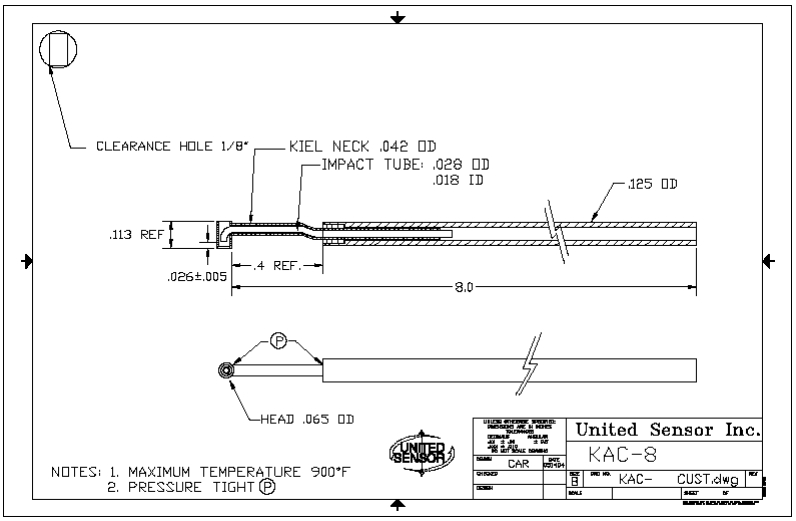

Figure C.1: Kiel Probe Schematic Drawing

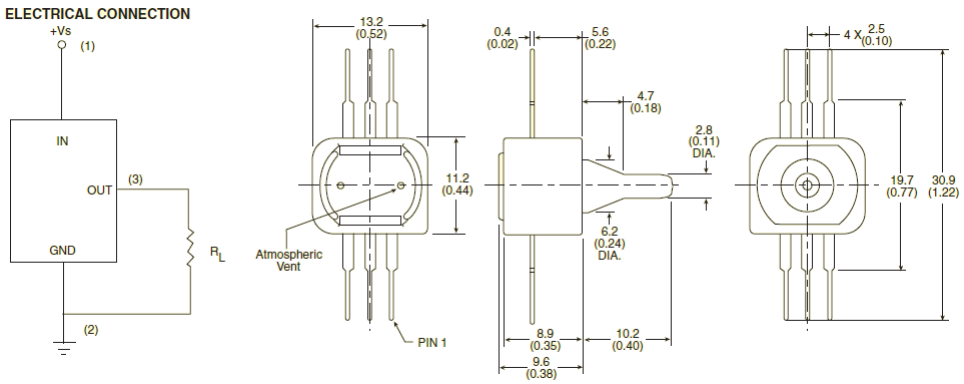

Figure C.2: Pressure Transducer Schematic Drawing. Dimensions: mm (in)

Table C.2: Pressure Transducer Specifications

Specification	**Value, Low Pressure**	**Value, High Pressure**
Serial numbers	PX40-50BHG5V	PX40-15G5V
Range	±6.7kPa	0 to 1 bar
Supplier	Omega	Omega
Output	0.5 to 4 VDC	0.5 to 4 VDC
Linearity	0.80%	0.20%
Repeatability	0.15% FS	0.15% FS
Null	2.50±0.05VDC	0.50±0.11VDC

C.2 Temperature Hardware Specifications

Table C.3: Data Logger Thermometer Specifications

Specification	**Value**
Serial Number	HH506A
Resolution	0.1/1
T Type temperature range	-200 to 400°C
Supplier	OMEGA

Table C.4: Thermocouple Specifications

Specification	**Value**
Serial number	TMQSS-062U-6
Junction type	Ungrounded
Probe length	6in
Thermocouple type	T
Sheath diameter	0.062in
Thermocouple material	Copper-constantan
Sheath meterial	304 SS
Supplier	OMEGA

Appendix D

Biodiesel Specifications

9 . Physical and chemical properties

Physical state	:	Liquid. [Clear.]
Flash point	:	Open cup: >130°C (266°F) (Cleveland./ASTM D93).
Color	:	Transparent.
Odor	:	Mild.
Boiling/condensation point	:	>200°C (>392°F)
Relative density	:	0.883 (Water = 1) at 15°C (59°F)
Solubility	:	Insoluble in the following materials: cold water and hot water.

Figure D.1: Fuel properties as analyzed by Rothsay Biodiesel [100]

CERTIFICATE OF ANALYSIS

Product Name: **Biodiesel B100**	Product meets **ASTM D6751-11b Specification**		
Manufacturer: **Rothsay Biodiesel**	Lot number: **F0378R65**		
	Production date: **March 5, 2012**		
Customer:	Loading date:	**Tank #: 65**	
Order number:	Train #: N/A	Trailer#: N/A	

PROPERTY	METHOD	RESULTS	UNITS	LIMITS	
				Min.	Max.
Water content [2]	ASTM D6304	64.6	ppm	Report to customer	
Flash point(closed cup) [2]	D93	178	°C	93	-
Water and sediment [2]	D2709	0	% vol.	-	0.050
Kinematic Viscosity @ 40 °C [2]	D445	4.5304	mm^2/s	1.9	6.0
Sulphated Ash *	D874	[< 0.001]	%mass.	-	0.020
Sulphur content*	D5453	7.1	ppm	-	15
Phosphorous Content *	D4951	[<2]	ppm	-	10
Copper Corrosion, 3hrs @ 50 °C *	D130	[1a]	-	-	No.3
Cetane number *	D613	[62]	minute	47	-
Cloud point [2]	D2500	12.5	°C	Report to customer	
Distillation @ 90% *	D1160	[357]	°C	-	360
Carbon Residue *	D4530	[0.01]	%mass.	-	0.050
Acid number [2]	D664	0.242	mg KOH/g	-	0.50
Free Glycerin [2]	D6584	0.0096	%mass.	-	0.020
Monodiglycerides [2]	D6584	0.2378	%mass.	-	-
Total Glycerin [2]	D6584	0.0712	%mass.	-	0.240
Calcium and Magnesium, combined *	EN 14538	[<1]	ppm	-	5
Sodium and Potassium, combined *	EN 14538	[<1]	ppm	-	5
Oxidation Stability [2]	EN 15751	9.73	hours	3	-
Cold Soak Filtration*	D7501	90	sec	-	200

Comments: * These tests were subcontracted by Intertek Caleb Brett
[2] These tests were done by Rothsay lab
[ ] Typical result, one time verified per month

Figure D.2: Certificate of Analysis for the B100, analyzed by Rothsay Biodiesel [100]

Appendix E

Test Matrix

E.1 Air Jet PIV

Table E.1 shows the experiments completed for the air jet characterization. These experiments were done in a randomized order to ensure that lurking time-related variables do not influence the calculation of effects of the main variables involved. [101]

E.2 Spray Characteristics

For spray characterstics, a comprehensive set of experiments were repeated in its entirety for each of the three fuels. The experimental set covered all the permutations of injection pressure, cross airflow velocity, and fuel type required to analyze their effects. Table E.2 summarizes the experiment set. Similar to air jet characterization, the run order was randomized so as to maintain the independence of observations. Each experiment captured the spray development from 0.3ms to 1.2ms after the start of the injection trigger at 0.1ms increments. For each increment, 25 individual images were taken.

Table E.1: Air Jet Characterization Experiment Test Matrix

Case	**Crossflow Velocity (m/s)**	**Injection Pressure (bar)**	**Injector x-location (mm)**
1	49.3	N/A	N/A
2	49.3	N/A	50
3	49.3	N/A	250
4	125.0	N/A	N/A
5	125.0	N/A	50
6	125.0	N/A	250
7	213.7	N/A	N/A
8	213.7	N/A	50
9	213.7	N/A	250

Table E.2: Spray Characterization Experiment Test Matrix

Fuel	**Cross Airflow Velocity (m/s)**	**Injection Pressure (bar)**	**Injector location (x/D)**
D100, B20, B100	0	1200	N/A
D100, B20, B100	0	1500	N/A
D100, B20, B100	125.0	1200	1.5
D100, B20, B100	213.7	1200	1.5
D100, B20, B100	125.0	1500	1.5
D100, B20, B100	213.7	1500	1.5
D100, B20, B100	125.0	1200	10
D100, B20, B100	213.7	1200	10
D100, B20, B100	125.0	1500	10
D100, B20, B100	213.7	1500	10
D100, B20, B100	49.3	1200	1.5

Appendix F

Uncertainty and Error Analysis

F.1 Slip Velocity Calculations

The slip velocity can be estimated using an iterative process given in Eq. (F.1) starting with $\phi = 1$ [102]. Final iterations of slip velocity calculations are shown in Table F.1. The calculations are computed using values from Table F.2.

$$v_p - u = \frac{\bar{\rho} - 1}{\rho} g \tau_o / \phi \tag{F.1a}$$

$$Re_p = \frac{|u - v_p| d_p}{\nu_f} \tag{F.1b}$$

$$\phi = \begin{cases} 1 + \frac{3}{16} Re_p, & Re_p \leq 0.01 \\ 1 + 0.131 Re_p^{0.82 - 0.05 log_{10} Re_p}, & 0.01 \leq Re_p \leq 20 \\ 1 + 0.1935 Re_p^{0.6305}, & 20 \leq Re_p \leq 260 \end{cases} \tag{F.1c}$$

where $\tau_o = \frac{\rho_p d_p^2}{18 \nu_f \rho_f}$, $\bar{\rho} = \rho_p / \rho_f$, $g = 9.81\text{m/s}$, $\rho_f = 914\text{kg/m}^3$, and $\nu_f = 25.16\text{mm}^2\text{/s}$.

Table F.1: Slip velocity error calculation values - Final iteration

$\mathbf{V}_x$, **(m/s)**	**Slip Velocity, (m/s)**	$\mathbf{Re}_p$	Φ
49.3	$6.72\text{x}10^{-5}$	$5.3\text{x}10^{-6}$	1.000001002
125.0	$7.02\text{x}10^{-5}$	$5.6\text{x}10^{-6}$	1.000001047
213.7	$7.74\text{x}10^{-5}$	$6.1\text{x}10^{-6}$	1.000001153

Table F.2: Parameter values for slip velocity error calculations

Parameter	**Value**
Gravity (m/s^2)	9.81
DEHS Particle Diamater (m)	$2.00\text{x}10^{-6}$
DEHS Kinematic Viscosity (kg/s·m)	$2.52\text{x}10^{-6}$
DEHS Density (kg/m^3)	914
Air Density @ 49.3m/s (kg/m^3)	1.177
Air Density @ 125.0m/s (kg/m^3)	1.126
Air Density @ 213.7m/s (kg/m^3)	1.022
Density Ratio @ 49.3m/s	777
Density Ratio @ 125.0m/s	811
Density Ratio @ 213.7m/s	894
Time constant @ 49.3m/s	$6.86\text{x}10^{-6}$
Time constant @ 125.0m/s	$7.17\text{x}10^{-6}$
Time constant @ 213.7m/s	$7.90\text{x}10^{-6}$

F.2 PIV Uncertainty Calculations

Perspective error becomes important when there is an out-of-plane component in the velocity flow field. Perspective error increases with distance away from the centre point of the camera lens. The magnitude of the y-component velocity at the jet centerline can be approximated to the z-component of the velocity at the edge of the spray jet at the same x-location. This approximation is based on the assumption that the round jet is symmetrical about the jet centerline. Perspective errors is represented as a non-dimensionalized vector, $\epsilon = \left(\frac{\Delta z}{\Delta x} \cdot tan\Theta_x, \frac{\Delta z}{\Delta y} \cdot tan\Theta_y\right)$. The errors in both directions were computed using Eq.(F.2),

$$\epsilon = (\epsilon_x, \epsilon_z) = \left(\frac{\Delta x^{'}}{\Delta x} - 1, \frac{\Delta z^{'}}{\Delta z} - 1\right) \tag{F.2a}$$

$$= \left(\frac{\Delta y}{\Delta x} tan\theta_x, \frac{\Delta y}{\Delta z} tan\theta_z\right) \tag{F.2b}$$

where "θ_x and θ_z are projections of θ on the x-y and y-z planes, respectively" [103]. The parameters and their values are shown in Fig. F.1 and Table F.3.

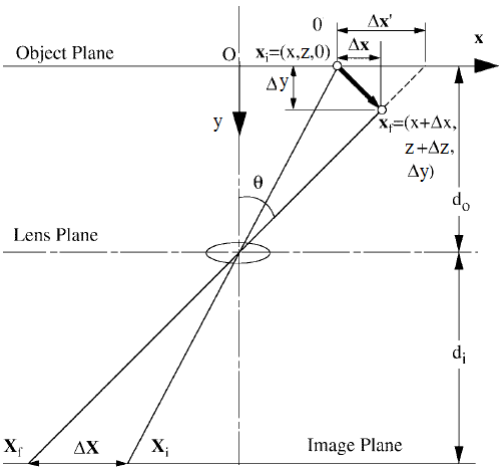

Figure F.1: Error in measurement of in-plane velocity due to out-of-plane velocity component [103]

Table F.3: Parameter values for perspective error calculations at different airflow velocities

Parameter	**V_x=49.3m/s**	**V_x=125.0m/s**	**V_x=213.7m/s**
dt (μs)	20	10	7
d_o* (m)	1.5	1.5	1.5
V_y (m/s)	2.2	1.3	1.5
V_z (m/s)	0.6	0.4	0.0
x_o (mm)	14.0	28.0	32.0
z_o (mm)	-10.0	-2.1	-0.3
Δx' (mm)	15.0	29.3	33.5
Δz' (mm)	-10.0	-2.1	-0.3
θ_x (rad)	0.01	0.02	0.02
θ_z (rad)	-0.01	0.00	0.00
Δx (mm)	15.0	29.3	33.5
Δy (mm)	$4.4x10^{-5}$	$1.3x10^{-5}$	$1.1x10^{-5}$
Δz (mm)	-10.0	-2.1	-0.3
ϵ_x (%)	$2.9x10^{-8}$	$8.7x10^{-9}$	$7.0x10^{-9}$
ϵ_z (%)	$2.9x10^{-8}$	$8.7x10^{-9}$	$7.0x10^{-9}$

*Estimated based on distance from camera to image plane

Appendix G

Canny Edge Detection

MATLAB has several edge detection methods. Of these methods, the one with that performs best with noisy images and more likely to detects true weak edges is the Canny method [104]. This method involves an algorithm with four major steps.

1. Noise reduction is performed by convolving the raw binary image, denoted by $f(x, y)$, with a Gaussian filter, $G(x, y)$, to produce a slightly blurred or smoothed version of the original image, $fs(x, y) = G(x, y) * f(x, y)$. The inputted σ value denotes the standard deviation to be used in the Gaussian filter.

2. Next, the intensity gradient and the edge direction angle are determined. The intensity gradient of the image, $M(x, y) = \sqrt{g_x^2 + g_y^2}$, is computed by taking the first derivative of the smoothed image function in both the horizontal and vertical directions: $g_x = \partial fs/\partial x$ and $g_y = \partial fs/\partial y$. The edge direction angle is found using $\alpha(x, y) = tan^{-1}(g_y/g_x)$.

3. Non-maximal suppression is performed to determine if the gradient magnitude is the local maximum in the gradient direction, such that all the non-edge points are set to zero. This is done by comparing the value of $M(x, y)$ with the edge direction angle rounded to the closest vertical, horizontal, or diagonal degrees ($\pm 45°$). If the value

of $M(x, y)$ is greater than the pixel intensity of the surrounding pixels normal to the rounded edge direction angle, it is considered to be part of the edge.

4. Finally, hysteresis thresholding sets all pixels that are above the high threshold, T_H, to be part of the edge, and all pixels above the lower threshold, T_L to be part of the edges if they are connected to adjacent edge pixels.

Appendix H

Experimental Data Readings

Axisymmetricity

Spray Penetration (mm)								
Time ASOI (ms)	Plume							
	1	2	3	4	5	6	7	8
0.4	15.950	14.266	13.003	9.924	9.403	13.312	14.587	15.429
0.5	40.909	37.166	34.231	32.704	29.386	33.464	38.539	41.188
0.6	61.723	56.870	52.471	56.032	54.295	53.699	57.554	61.913
0.7	83.352	74.150	67.146	67.154	69.916	66.855	74.167	81.181
0.8	100.555	81.152	74.848	84.119	76.544	75.392	82.008	97.075

*D100, Pinj=1200bar, Va=125.0m/s

Symmetric:
Plume 1 ⟷ Plume 8
Plume 2 ⟷ Plume 7
Plume 3 ⟷ Plume 6
Plume 4 ⟷ Plume 5

Effect of Cross Airflow Velocity

			Va=0m/s, Pinj=1200bar, x/D=1.5						Va=49.3m/s, Pinj=1200bar, x/D=1.5						Va=125.0/s, Pinj=1200bar, x/D=1.5						Va=213.7m/s, Pinj=1200bar, x/D=1.5					
		Time ASOI	Plume						Plume						Plume						Plume					
		(ms)	1	2	3	6	7	8	1	2	3	6	7	8	1	2	3	6	7	8	1	2	3	6	7	8
Spray Penetration (mm)	D100	0.4	7.55	7.67	7.76	8.08	12.89	8.49	13.28	14.17	13.26	13.53	13.84	13.88	12.68	11.12	11.27	10.34	11.56	11.86	12.24	12.59	10.18	11.20	12.42	13.15
		0.5	28.53	30.79	30.46	29.64	30.79	29.87	35.98	35.65	34.35	38.20	37.26	37.20	34.24	30.80	29.10	28.87	29.73	32.98	37.28	30.61	27.30	27.97	32.51	38.60
		0.6	56.40	57.25	59.38	62.10	62.42	58.39	61.06	59.87	54.71	60.37	62.19	63.12	58.62	53.14	47.53	47.52	51.11	56.20	61.99	47.41	37.81	42.22	49.11	59.60
		0.7	79.17	78.12	79.45	84.15	84.66	82.27	85.29	74.69	69.67	69.29	82.14	88.64	76.15	69.19	61.24	61.56	66.91	72.48	81.55	59.78	46.12	56.36	63.58	76.76
		0.8	96.86	94.12	90.92	99.99	99.49	101.23	104.94	77.75	72.14	83.28	86.45	111.19	99.97	85.11	76.82	73.99	84.61	91.76	101.48	69.42	55.07	69.29	77.61	90.33
		Time ASOI	Plume						Plume						Plume						Plume					
		(ms)	1	2	3	6	7	8	1	2	3	6	7	8	1	2	3	6	7	8	1	2	3	6	7	8
	B20	0.4	14.10	14.14	12.82	13.20	14.25	14.50	14.33	14.01	14.54	13.85	15.27	14.54	13.83	13.81	10.75	12.36	15.31	15.25	12.59	11.91	11.36	11.58	12.23	12.75
		0.5	35.56	35.05	34.28	35.71	37.08	36.83	40.96	35.19	35.85	34.94	36.25	40.93	37.64	34.28	32.91	31.81	36.32	38.01	37.43	33.03	27.83	27.36	30.85	37.44
		0.6	60.23	58.49	59.18	61.24	59.70	60.66	61.14	57.32	59.75	51.12	60.01	60.94	61.58	54.93	52.57	52.83	57.45	60.78	59.95	50.07	41.40	36.99	50.13	60.14
		0.7	82.41	82.44	84.75	86.38	87.01	86.53	81.87	77.88	78.37	54.43	76.05	81.74	78.94	70.66	67.43	71.11	77.33	78.91	81.26	65.02	53.68	47.41	65.83	79.00
		0.8	112.81	104.21	105.64	109.92	107.88	108.36	102.41	96.67	85.50	59.26	82.78	96.15	91.85	82.97	74.84	79.87	92.22	94.10	99.34	79.45	62.26	59.29	78.43	93.12
		Time ASOI	Plume						Plume						Plume						Plume					
		(ms)	1	2	3	6	7	8	1	2	3	6	7	8	1	2	3	6	7	8	1	2	3	6	7	8
	B100	0.4	14.48	13.91	14.26	14.44	15.11	15.12	15.26	15.42	17.39	15.66	15.32	15.51	13.84	14.14	14.09	13.28	13.98	13.87	12.63	12.20	11.98	12.45	13.20	12.97
		0.5	34.65	34.37	34.12	34.53	36.86	36.18	39.99	39.13	40.03	39.28	38.63	39.02	37.86	34.13	33.90	31.79	33.65	37.79	35.53	32.26	25.93	26.40	32.16	36.72
		0.6	56.93	56.22	55.74	56.29	59.32	58.06	63.32	61.68	62.93	60.73	63.07	63.72	59.87	54.05	50.06	49.81	54.43	59.27	60.21	50.11	37.44	37.97	49.32	59.13
		0.7	78.17	79.35	77.81	81.65	82.87	79.85	84.79	79.89	83.20	80.78	86.07	87.29	80.25	71.27	64.79	63.84	73.55	76.11	78.49	63.80	49.02	48.95	62.41	74.99
		0.8	99.33	100.84	99.17	108.14	106.84	102.68	105.21	101.58	101.35	95.47	99.44	108.49	95.46	85.95	79.24	76.41	84.98	88.56	94.63	73.97	58.54	54.53	74.86	89.28
Axis Deflection (deg)		Time ASOI	Plume						Plume						Plume						Plume					
		(ms)	1	2	3	6	7	8	1	2	3	6	7	8	1	2	3	6	7	8	1	2	3	6	7	8
	D100	0.4	4.67	2.06	-4.07	0.93	-4.55	-4.53	1.91	-0.65	2.53	3.27	1.02	0.62	10.17	5.89	4.61	9.29	3.89	0.36	1.60	8.19	10.63	13.97	6.66	0.51
		0.5	0.35	-1.57	-1.76	-0.49	-2.37	-1.47	0.99	0.93	1.31	1.49	-0.40	-0.72	2.24	1.39	2.82	4.51	1.89	1.62	4.47	7.68	7.16	6.75	3.00	2.72
		0.6	0.40	-0.29	-1.82	-0.65	-1.05	-1.84	1.33	0.82	1.24	1.00	-0.43	-0.81	2.00	0.24	2.80	3.79	1.36	1.31	7.63	5.89	9.81	8.46	3.62	4.15
		0.7	0.59	-1.15	-1.32	-0.27	-1.89	-1.53	1.29	1.66	0.12	1.12	-0.60	-0.79	2.75	1.44	2.63	3.65	1.83	1.42	10.42	6.29	9.33	7.43	3.19	3.77
		0.8	0.37	-0.86	-1.53	-0.39	-1.75	-1.75	1.27	6.68	-1.46	1.70	0.65	-1.01	7.20	2.72	2.20	3.87	1.42	2.71	14.00	6.62	7.85	6.00	3.07	2.74
		Time ASOI	Plume						Plume						Plume						Plume					
		(ms)	1	2	3	6	7	8	1	2	3	6	7	8	1	2	3	6	7	8	1	2	3	6	7	8
	B20	0.4	2.54	0.86	2.51	3.90	-0.21	0.56	2.65	5.75	2.13	4.06	10.30	0.37	3.37	7.66	10.08	14.85	6.69	0.20	1.67	9.68	11.24	10.51	6.33	1.10
		0.5	1.62	0.31	0.02	0.69	-0.89	-0.78	3.63	0.46	0.72	1.86	-0.46	3.34	3.44	2.39	2.32	5.02	1.29	1.05	3.84	5.21	7.66	9.95	3.38	2.94
		0.6	1.07	0.52	0.13	0.07	-1.26	-1.20	1.73	0.16	0.14	1.48	-0.77	-0.55	3.45	2.85	2.33	3.75	1.15	1.41	7.29	4.71	8.89	14.01	5.04	6.57
		0.7	0.90	0.24	-0.31	0.20	-1.18	-1.02	1.20	-0.34	0.01	1.26	-0.52	-0.61	3.34	2.61	2.85	3.54	1.17	0.85	11.57	4.41	7.86	9.39	2.92	8.21
		0.8	0.59	3.01	0.29	-0.25	-0.77	-1.16	1.38	-0.52	1.27	-0.08	-0.96	-0.75	3.30	2.62	2.55	3.73	0.75	0.76	13.10	6.36	7.53	8.84	3.16	8.45
		Time ASOI	Plume						Plume						Plume						Plume					
		(ms)	1	2	3	6	7	8	1	2	3	6	7	8	1	2	3	6	7	8	1	2	3	6	7	8
	B100	0.4	3.90	1.24	0.17	1.56	-1.45	-1.99	1.24	1.15	1.09	0.07	-1.08	0.44	1.33	1.54	4.31	6.27	2.21	-0.38	3.08	8.94	8.56	10.41	5.62	-1.01
		0.5	2.12	0.32	-0.19	1.10	-1.53	-1.74	0.98	-0.25	0.26	0.31	-1.06	-0.13	2.10	1.70	2.47	3.63	0.87	1.04	3.31	9.36	8.81	11.09	3.74	1.53
		0.6	1.60	0.31	-0.35	0.48	-1.42	-1.26	1.18	0.15	0.31	0.56	-1.11	-0.46	2.64	1.90	2.93	3.44	0.91	1.26	5.66	4.80	8.83	11.83	2.74	4.19
		0.7	1.18	0.23	-0.40	0.11	-1.41	-1.48	1.47	0.23	0.21	0.26	-1.09	-0.64	2.68	1.90	3.13	3.40	0.82	1.59	10.18	5.67	8.68	10.49	3.37	7.08
		0.8	1.15	0.13	-0.46	-0.14	0.42	-1.61	0.83	-3.42	-0.02	-0.08	-1.14	-0.53	2.97	1.87	2.17	2.89	0.88	1.44	13.04	4.89	7.02	8.39	3.55	8.14

Effect of Fuel Type

			Pinj = 1200bar, Va=91m/s, x/D=10			
Spray Penetration (mm)	D100	Time ASOI (ms)	Plume			
			1	2	3	4
		0.4	15.95	14.27	13.00	9.92
		0.5	40.91	37.17	34.23	32.70
		0.6	61.72	56.87	52.47	56.03
		0.7	83.35	74.15	67.15	67.15
		0.8	100.56	81.15	74.85	84.12
	B20	Time ASOI (ms)	Plume			
			1	2	3	4
		0.4	9.55	9.68	9.80	8.16
		0.5	26.43	25.84	24.49	24.87
		0.6	61.91	56.28	51.27	54.92
		0.7	84.61	73.24	65.16	68.47
		0.8	104.11	88.01	76.40	81.98
	B100	Time ASOI (ms)	Plume			
			1	2	3	4
		0.4	16.30	15.27	13.40	10.62
		0.5	39.75	36.36	32.24	32.13
		0.6	60.79	54.22	48.97	50.32
		0.7	81.78	69.47	63.82	64.19
		0.8	99.60	84.93	74.13	77.79
Axis Deflection (deg)	D100	Time ASOI (ms)	Plume			
			1	2	3	4
		0.4	5.28	10.75	10.88	8.02
		0.5	5.75	0.69	5.06	5.66
		0.6	2.67	3.07	3.24	4.30
		0.7	2.70	2.39	2.82	3.54
		0.8	3.18	4.25	1.25	3.67
	B20	Time ASOI (ms)	Plume			
			1	2	3	4
		0.4	3.20	4.62	2.83	6.20
		0.5	3.85	3.50	3.13	1.72
		0.6	3.19	4.08	4.62	3.66
		0.7	3.34	3.36	3.14	3.83
		0.8	2.71	2.89	3.62	3.66
	B100	Time ASOI (ms)	Plume			
			1	2	3	4
		0.4	5.20	8.08	10.17	5.59
		0.5	3.96	5.03	5.59	3.12
		0.6	3.36	4.04	4.44	4.84
		0.7	2.93	3.70	3.86	5.53
		0.8	3.70	4.32	3.55	3.74

Effect of Injection Pressure

			Pinj=1200 bar, Va=125.0m/s, x/D=10				Pinj=1500 bar, Va=125.0m/s, x/D=10			
Spray Penetration (mm)	D100	Time ASOI (ms)	Plume				Plume			
			1	2	3	4	1	2	3	4
		0.4	15.95	14.27	13.00	9.92	25.19	25.24	22.45	17.80
		0.5	40.91	37.17	34.23	32.70	50.47	48.96	45.84	45.05
		0.6	61.72	56.87	52.47	56.03	79.73	70.01	63.24	67.82
		0.7	83.35	74.15	67.15	67.15	103.58	83.67	76.13	81.59
		0.8	100.56	81.15	74.85	84.12	-	-	-	-
		0.9	-	-	-	-	-	-	-	-
		1.0	-	-	-	-	-	-	-	-
	B20	Time ASOI (ms)	Plume				Plume			
			1	2	3	4	1	2	3	4
		0.4	9.55	9.68	9.80	8.16	25.86	25.60	22.44	19.08
		0.5	26.43	25.84	24.49	24.87	50.11	47.95	45.40	45.50
		0.6	61.91	56.28	51.27	54.92	76.35	70.05	64.85	66.88
		0.7	84.61	73.24	65.16	68.47	99.79	87.64	81.98	81.76
		0.8	104.11	88.01	76.40	81.98	-	-	-	-
		0.9	-	-	-	-	-	-	-	-
		1.0	-	-	-	-	-	-	-	-
	B100	Time ASOI (ms)	Plume				Plume			
			1	2	3	4	1	2	3	4
		0.4	16.30	15.27	13.40	10.62	28.27	26.21	23.83	22.62
		0.5	39.75	36.36	32.24	32.13	50.07	44.51	42.70	43.38
		0.6	60.79	54.22	48.97	50.32	73.45	66.99	62.89	64.56
		0.7	81.78	69.47	63.82	64.19	94.71	80.81	78.20	81.71
		0.8	99.60	84.93	74.13	77.79	-	-	-	-
		0.9	-	-	-	-	-	-	-	-
		1.0	-	-	-	-	-	-	-	-
Axis Deflection (deg)	D100	Time ASOI (ms)	Plume				Plume			
			1	2	3	4	1	2	3	4
		0.4	15.95	14.27	13.00	9.92	4.91	16.55	6.60	5.14
		0.5	40.91	37.17	34.23	32.70	2.32	2.56	4.03	3.81
		0.6	61.72	56.87	52.47	56.03	3.51	3.90	3.42	2.94
		0.7	83.35	74.15	67.15	67.15	2.86	3.83	1.97	3.49
		0.8	100.56	81.15	74.85	84.12	-	-	-	-
		0.9	-	-	-	-	-	-	-	-
		1.0	-	-	-	-	-	-	-	-
	B20	Time ASOI (ms)	Plume				Plume			
			1	2	3	4	1	2	3	4
		0.4	3.20	4.62	2.83	6.20	3.87	6.99	7.75	6.04
		0.5	3.85	3.50	3.13	1.72	2.77	3.22	3.52	3.29
		0.6	3.19	4.08	4.62	3.66	2.83	2.96	3.50	3.76
		0.7	3.34	3.36	3.14	3.83	2.87	2.97	2.99	3.73
		0.8	2.71	2.89	3.62	3.66	-	-	-	-
		0.9	-	-	-	-	-	-	-	-
		1.0	-	-	-	-	-	-	-	-
	B100	Time ASOI (ms)	Plume				Plume			
			1	2	3	4	1	2	3	4
		0.4	5.20	8.08	10.17	5.59	3.57	10.21	4.86	1.91
		0.5	3.96	5.03	5.59	3.12	3.77	4.68	3.83	3.49
		0.6	3.36	4.04	4.44	4.84	3.07	5.41	3.44	4.18
		0.7	2.93	3.70	3.86	5.53	3.39	5.41	2.75	2.76
		0.8	3.70	4.32	3.55	3.74	-	-	-	-
		0.9	-	-	-	-	-	-	-	-
		1.0	-	-	-	-	-	-	-	-

Fuel Properties

Velocity (m/s)	Air Temp (C)	D100				
		Pinj (Pa)	Pair (Pa)	Density (kg/m3)	Cd	Vf
0	24.3	120000000	101325	836	0.8	428.5
49.3	27.1	120000000	101325	839	0.8	427.7
125.046	40.2	120000000	101325	829	0.8	430.2
213.656	73.3	120000000	101325	811	0.8	435.1
0	24.3	150000000	101325	836	0.8	479.1
49.3	27.1	150000000	101325	839	0.8	478.2
125.046	40.2	150000000	101325	829	0.8	481
213.656	73.3	150000000	101325	811	0.8	486.4

Velocity (m/s)	Air Temp (C)	B20				
		Pinj (Pa)	Pair (Pa)	Density (kg/m3)	Cd	Vf
0	24.3	120000000	101325	833	0.8	429.3
49.3	27.1	120000000	101325	833	0.8	429.1
125.046	40.2	120000000	101325	835	0.8	428.7
213.656	73.3	120000000	101325	815	0.8	433.9
0	24.3	150000000	101325	833	0.8	480
49.3	27.1	150000000	101325	833	0.8	479.8
125.046	40.2	150000000	101325	835	0.8	479.3
213.656	73.3	150000000	101325	815	0.8	485.2

Velocity (m/s)	Air Temp (C)	B100				
		Pinj (Pa)	Pair (Pa)	Density (kg/m3)	Cd	Vf
0	24.3	120000000	101325	867	0.8	420.7
49.3	27.1	120000000	101325	858	0.8	422.9
125.046	40.2	120000000	101325	864	0.8	421.4
213.656	73.3	120000000	101325	847	0.8	425.6
0	24.3	150000000	101325	867	0.8	470.4
49.3	27.1	150000000	101325	858	0.8	472.9
125.046	40.2	150000000	101325	864	0.8	471.2
213.656	73.3	150000000	101325	847	0.8	475.8

Velocity (m/s)	Air Temp (C)	D100										
		Mass (g)	Volume (ml)	Density (kg/m3)	Volume error	Mass Error	Density Error	Error (new)	Error (-)	Error (+)	Dyn Visco (cP)	Error (+/-)
--	21.1	--	--	840							3.36	
0	24.3	18.725	22.4	836	1.12%	0.16%	0.001	9.33	9.23	9.43	3.21	0.06
49.3	27.1	18.965	22.6	839	1.11%	0.16%	0.417	9.283	9.18	9.39	3.02	0.06
125.046	40.2	19.237	23.2	829	1.08%	0.16%	0.391	8.935	8.84	9.03	2.16	0.06
213.656	73.3	19.663	24.25	811	1.03%	0.16%	0.351	8.359	8.27	8.45	1.28	0.06
Velocity (m/s)	Air Temp (C)	B20										
		Mass (g)	Volume (ml)	Density (kg/m3)				Error (new)	Error (-)	Error (+)	Dyn Visco (kg/m.s)	Error (+/-)
--	21.1	--	--	850							3.74	
0	24.3	17.737	21.3	833				9.774	9.66	9.89	3.53	0.06
49.3	27.1	18.336	22	833				9.471	9.36	9.58	3.27	0.06
125.046	40.2	17.121	20.5	835				10.185	10.06	10.31	2.32	0.06
213.656	73.3	17.524	21.5	815				9.478	9.37	9.59	1.45	0.06
Velocity (m/s)	Air Temp (C)	B100										
		Mass (g)	Volume (ml)	Density (kg/m3)				Error (new)	Error (-)	Error (+)	Dyn Visco (kg/m.s)	Error (+/-)
--	21.1	--	--	883							6.01	
0	24.3	19.506	22.5	867				9.633	9.53	9.74	5.65	0.06
49.3	27.1	19.304	22.5	858				9.533	9.43	9.64	5.29	0.06
125.046	40.2	19.444	22.5	864				9.602	9.5	9.71	3.69	0.06
213.656	73.3	19.279	22.75	847				9.312	9.21	9.42	2.05	0.06

Sample Size Uncertainty

Error in Spray Penetration (mm)					
Time ASOI (ms)	Number of Realizations (images)				
	5	10	15	20	25
0.4	0.495	0.118	0.022	0.036	0
0.5	-0.058	0.002	-0.003	-0.071	0
0.6	-1.313	-0.357	-0.141	-0.024	0
0.7	-3.595	-2.067	-1.125	-0.332	0
0.8	-0.563	-0.143	-0.379	-0.160	0

*D100, Pinj=1200bar, x/D=10, Va=125.0m/s, Plume 2

Error in Axis Deflection (deg)					
Time ASOI (ms)	Number of Realizations (images)				
	5	10	15	20	25
0.4	-0.196	0.508	0.140	0.083	0
0.5	0.558	0.244	0.173	0.115	0
0.6	-0.470	0.393	-0.361	-0.107	0
0.7	-1.752	-1.109	0.187	0.299	0
0.8	0.520	-2.962	-1.404	-0.865	0
0.9	-1.702	-0.811	-0.214	-0.185	0
1.0	0.347	-0.108	-0.441	-0.442	0

*B20, Pinj=1200bar, x/D=1.5, Va=213.7m/s, Plume 4

Sensitivity Analyses

Sensitivity of Low Threshold (TL) on Spray Penetration (mm)			
TL	TH		
	0.015	0.03	0.1
0.001	69.548	64.657	57.767
0.005	69.548	64.657	57.767
0.010	69.548	64.657	57.767
0.015	69.548	64.657	57.767
0.020	69.548	64.657	57.767
0.025	69.548	64.657	57.767

*B20, Va=125.0m/s, Pinj=1200bar, t=0.7ms ASOI

Sensitivity of High Threshold (TH) on Spray Penetration (mm)				
TL	TH			
	0.015	0.03	0.1	0.2
0.030	69.548	64.657	57.767	57.7665

*B20, Va=125.0m/s, Pinj=1200bar, t=0.7ms ASOI

Bibliography

[1] Y. Ren, E. Abu-Ramadan, and X. Li. Numerical simulation of biodiesel fuel combustion and emission characteristics in a direct injection diesel engine. *Frontiers of Energy and Power Engineering in China*, 4(2):252–261, 2010.

[2] S. Kim, J. W. Huang, and C. S. Lee. Experiments and modeling on droplet motion and atomization of diesel and bio-diesel fuels in a cross-flowed air stream. *International Journal of Heat and Fluid Flow*, 31:667–679, 2010.

[3] B. Douailler and F. Ravet. Direct injection of CNG on high compression ratio spark ignition engine: Numerical and experimental investigation. SAE paper 2011-01-0923. 2011.

[4] J. Wallesten, A. Lipatnikov, and J. Chomiak. Simulations of fuel/air mixing, combustion, and pollutant formation in a direct injection gasoline engine. SAE paper 2002-01-0835. 2002.

[5] M. C. Drake, T. D. Fansler, and A. M. Lippert. Stratified-charge combustion: modeling and imaging of a spray-guided direct-injection spark-ignition engine. *Proceedings of the Combustion Institute*, pages 2683–2691, 2005.

[6] M. Cardenas, P. Hottenbach, R. Kneer, and G. Grunefeld. Investigations of clustered diesel jets under quiescent high-pressure and high-temperature conditions using Mie, Schlieren and chemiluminescence imaging. SAE paper 2009-01-2771. 2009.

[7] S. Alfuso, L. Allocca, G. Caputo, F. E. Corcione, A. Montanaro, and G. Valentino. Experimental investigation of a spray from a multi-jet common rail injection system for small engines. SAE paper 2005-24-090. 2005.

[8] D. Siebers and B. Higgins. Flame lift-off on direct-injection diesel sprays under quiescent conditions. SAE paper 2001-01-0530. 2001.

[9] J. H. Yoo, S. K. Kim, F. Q. Zhao, and M. C. Lai. Visualization of direct-injection gasoline spray and wall-impingement inside a motoring engine. SAE paper 982702. 1998.

[10] N. A. Chigier. The atomization and burning of liquid fuel sprays. *Progress in Energy and Combustion Science*, 2:97–114, 1976.

[11] S. R. Turns. *An Introduction to Combustion*. Mcgraw-Hill, Singapore, 2006.

[12] A. H. Lefebvre. *Atomization and Sprays*. Hemisphere Publishing Corporation, New York, 1989.

[13] J. B. Heywood. *Internal combustion engine fundamentals*. McGraw-Hill, 1988.

[14] R. van Basshuysen and F. Schafer. *Internal Combustion Engine Handbook: Basics, Components, Systems, and Perspectives*. SAE International, Warrendale, PA, 2004.

[15] L. Araneo, A. Coghe, G. Brunello, and G. E. Cossali. Experimental investigation of gas density effects on diesel spray penetration and entrainment. SAE paper 1999-01-0525. 1999.

[16] S. W. Lee, D. Tanaka, J. Kusaka, and Y. Daisho. Effects of diesel fuel characteristics on spray and combustion in a diesel engine. *JSAE Review*, 23(4):407–414, 2002.

[17] S. Martnez-Martnez, F. Sanchez, V. Bermudez, and J. Riesco-Avila. *Liquid Sprays Characteristics in Diesel Engines*. Fuel Injection. InTech Publishing, 2010.

[18] I. V. Roisman, L. Araneo, and C. Tropea. Effect of ambient pressure on penetration of a diesel spray. *International Journal of Multiphase Flow*, 33(8):904–920, 2007.

[19] H. Hiroyasu and M. Arai. Structures of fuel sprays in diesel engines. *SAE Transactions*, 99(Sect 3):1050–1061, 1990.

[20] C. Baumgarten. *Mixture formation in internal combustion engines*. Springer Berlin Heidelberg, 2006.

[21] S. P. Lin and R. D. Reitz. Drop and spray formation from a liquid jet. *Annu. Rev. Fluid Mech.*, 30:85–105, 1998.

[22] G. M. Faeth. Structure and atomization properties of dense turbulent sprays. *Twenty-Third Symposium (International) on Combustion*, 23:1345–1352, 1990.

[23] J. D. Naber and D. L. Siebers. Effects of gas density and vaporization of penetration and dispersion of diesel sprays. SAE paper 960034. 1996.

[24] T. W. Ryan, L. G. Dodge, and T. J. Callahan. The effects of vegetable oil properties on injection and combustion in two different diesel engines. *Journal of the American Oil Chemists' Society*, 61(10):1610–1619, 1984.

[25] A. H. Lefebvre. *Gas turbine combustion*. Taylor & Francis, Philadelphia, 1999.

[26] A. H. Lefebvre. Properties of sprays. *Particle & Particle Systems Characterization*, 6(14):176–186, 1989.

[27] O. M. I. Nwafor. Emission characteristics of diesel engine running on vegetable oil with elevated fuel inlet temperature. *Biomass and Bioenergy*, 27(5):507–511, 2004.

[28] Y. Wakuri, M. Fujii, T. Amitani, and R. Tsuneya. Studies on the penetration of fuel spray in a diesel engine. *Bulletin of JSME*, 3(9):123–130, 1960.

[29] S. Gupta, R. Poola, and R. Sekar. Injection parameter effects on diesel spray characteristics. SAE paper 2000-01-2787. 2000.

[30] L. Li, X. Zhang, Z. Wu, J. Deng, and C. Huang. Experimental study of biodiesel spray and combustion characteristics. SAE paper 2006-01-3250. 2006.

[31] J. C. Dent. A basis for the comparison of various experimental methods for studying spray penetration. SAE paper 710571. 1971.

[32] N. Hay and P. L. Jones. Comparison of the various correlations for spray penetration. SAE paper 720776.

[33] E. Mancaruso, L. Sequino, and B. M Vaglieco. First and second generation biodiesels spray characterization in a diesel engine. *Fuel*, 90:2870–2883, 2011.

[34] M. Oki, S. Matsumoto, Y. Toyoshima, K. Ishisaka, and N. Tsuzuki. 180mpa piezo common rail system. SAE paper 2006-01-0274.

[35] J. Abraham, A. Khan, and V. Magi. Jet-jet and jet-wall interactions of transient jets from multi-hole injectors. SAE paper 1999-01-0513. 1999.

[36] P. Dahlander and R. Lindgren. Multi-hole injectors for disi engines: Nozzle hole configuration influence on spray formation. SAE paper 2008-01-0136. 2008.

[37] L. M. Malbec and G. Bruneaux. Study of air entrainment of multi-hole diesel injection by particle image velocimetry - effect of neighbouring jets interaction and transient behaviour after end of injection. SAE Paper 2010-01-0342. 2010.

[38] T. F. Fric and A. Roshko. Vortical structure in the wake of a transverse jet. *Journal of Fluid Mechanics*, 279:1–47, 1994.

[39] J. M. Desantes, R. Payri, F. J. Salvador, and A. Gil. Development and validation of a theoretical model for diesel spray penetration. *Fuel*, 85(7-8):910–917, 2006.

[40] S. H. Smith and M. G. Mungal. Mixing, structure and scaling of the jet in crossflow. *Journal of Fluid Mechanics*, 357:83–122, 1998.

[41] L. Cortelezzi and A. R. Karagozian. On the formation of the counter-rotating vortex pair in transverse jets. *Journal of Fluid Mechanics*, 446:347–373, 2001.

[42] M. Leong, V. G. McDonell, and G. S. Samuelsen. Mixing of an airblast-atomized fuel spray injected into a crossflow of air. Technical Report UCI-ARTR-00-05, NASA, 2000.

[43] D. Sedarsky and M. Paciaroni. Model validation image data for breakup of a liquid jet in crossflow: part i. *Experimental Fluids*, 49:391–408, 2010.

[44] S. Lee, W. Kin, and W. Yoon. Spray formation by a swirl spray jet in low speed cross-flow. *J Mech Science and Technology*, 24:559–568, 2010.

[45] K. A. Sallam, C. Aalburg, and G. M. Faeth. Breakup of round nonturbulent liquid jets in gaseous crossflow. *AIAA*, 42:2529–2540, 2004.

[46] M. A. Linne, M. Paciaroni, J. R. Gord, and T. R. Meyer. Ballistic imaging of the liquid core for a steady jet in crossflow. *Applied Optics*, 44:6627–6634, 2005.

[47] P. K. Wu, R. P. Fuller, K. A. Kirdendall, and A. S. Nejad. Breakup processes of liquid jets in subsonic crossflows. *Journal of Propulsion and Power*, 13:64–73, 1997.

[48] A. Mashayek and N. Ashgriz. Atomization of a liquid jet in a crossflow. In N. Ashgriz, editor, *Handbook of Atomization and Sprays: Theory and Applications*, pages 657–683. SpringerLink, 2011.

[49] J. M. Desantes, J. Arrgle, J. J. Lopez, and J. M. Garca. Turbulent gas jets and diesel-like sprays in a crossflow: A study on axis deflection and air entrainment. *Fuel*, 85:2120–2132, 2006.

[50] I. Lee, Y. Kang, and J. Koo. Mixing characteristics of pulsed air-assist liquid jet into an internal subsonic cross-flow. *Journal of Thermal Science*, 19, 2010.

[51] T. Inamura, N. Nagai, T. Watanabe, and N. Yatsuyanagi. Distintegration of liquid and slurry jets traversing subsonic airstreams. *Experimental Heat Transfer, Fluid Mechanics and Thermodynamics*, pages 1522–1529, 1993.

[52] T. Inamura and N. Nagai. Spray characteristics of liquid jet traversing subsonic airstreams. *Journal of Propulsion and Power*, 13:250–256, 1997.

[53] J. N. Stenzler, J. G. Lee, D. A. Santavicca, and W. Lee. Penetration of liquid jets in a cross-flow. *Atomization and Sprays*, 16:1, 2006.

[54] J. Becker and C. Hassa. Breakup and atomization of a kerosene jet in crossflow at elevated pressure. *Atomization and Sprays*, 11:49–67, 2002.

[55] P. K. Wu, K. A. Kirdendall, R. P. Fuller, and A. S. Nejad. Spray structures of liquid jets atomized in subsonic crossflows. *Journal of Propulsion and Power*, 14:173–182, 1998.

[56] S. Ghosh and J. C. R. Hunt. Spray jets in cross flow. *Journal of Fluid Mechanics*, 365:109–136, 1998.

[57] R. Menon and S. R. Gollahalli. Combustion characteristics of interacting multiple jets in cross flow. *Combustion Science and Technology*, 60:375–389, 2007.

[58] P. Ajersch, J. M. Zhou, S. Ketler, M. Salcudean, and I. S. Gartshore. Multiple jets in a crossflow: detailed measurements and numerical simulations. *ASME*, 119:330–342, 1997.

[59] J. D. Holdeman, R. E. Walker, and D. L. Kors. Mixing of multiple dilution jets with a hot primary airstream for gas turbine combustors. Technical Report NASA TM X-71426, NASA, 1973.

[60] M. K. Kim, J. Song, J. Hwang, and Y. Yoon. Effects of canted injection angles on the spray characteristics of liquid jets in subsonic crossflows. *Atomization and sprays*, 20:749–762, 2010.

[61] K. Yamane, A. Ueta, and Y. Shimamoto. Influence of physical and chemical properties of biodiesel fuels on injection, combustion and exhaust emission characteristics in a direct injection compression ignition engine. *International Journal of Engine Research*, 2, 2001.

[62] U.S. Environmental Protection Agency. A comprehensive analysis of biodiesel impacts on exhaust emissions. Technical Report EPA420-P-02-001, 2002.

[63] V. K. Chakravarthy, J. McFarlane, C. S. Daw, Y. Ra, and J. K. Griffin. Physical properties of bio-diesel & implications for use of bio-diesel in diesel engines. SAE paper 2007-01-4030. 2007.

[64] G. Knothe. Biodiesel and renewable diesel: A comparison. *Progress in Energy and Combustion Science*, 36:364–373, 2012.

[65] Y. Ra, R. Reitz, J. McFarlane, and C. S. Daw. Effects of fuel physical properties on diesel engine combustion using diesel and bio-diesel fuels. SAE paper 2008-01-1379. 2008.

[66] A. Demirbas. Characterization of biodiesel fuels. *Energy Sources, Part A: Recovery, Utilization, and Environmental Effects*, 31, 2009.

[67] M. Ahmed, C. E. Ejim, B. A. Fleck, and A. Amirfazli. Effect of biodiesel fuel properties and its blends on atomization. SAE paper 2006-01-0893. 2006.

[68] J. M. Desantes, R. Payri, A. Garcia, and J. Manin. Experimental study of biodiesel blends' effects on diesel injection processes. *Energy and Fuels*, 23:3227–3235, 2009.

[69] J. A. Bittle, B. M. Knight, and T. J. Jacobs. The impact of biodiesel on injection timing and pulsewidth in a common-rail medium-duty diesel engine. SAE paper 2009-01-2782. 2009.

[70] R. K. Pandey, A. Rehman, and R. M. Sarviya. Impact of alternative fuel properties on fuel spray behaviour and atomization. *Renewable and Sustainable Energy Reviews*, pages 1762–1778, 2012.

[71] S. Som, D. E. Longman, A. I Ramirez, and S. K. Aggarawal. A comparison of injector flow and spray characteristics of biodiesel and petrodiesel. *Fuel*, 89:4014–4024, 2010.

[72] P. Pogorevc, B. Kegl, and L. Skerget. Diesel and biodiesel fuel spray simulations. *Energy & Fuels*, 22:1266–1274, 2008.

[73] M. Gongping, W. Zhong, Y. Dianyong, Y. Yingnan, G. Shiqiang, and H. Huilong. Numerical simulation and experimental research on the free spray characteristics of bio-diesel fuel. SAE paper 2008-01-1598. 2008.

[74] X. Wang, Z. Huang, O. A. Kuti, W. Zhang, and K. Nishida. Experimental and analytical study on biodiesel and diesel spray characteristics under ultra-high injection pressure. *International Journal of Heat and Fluid Flow*, 31:659–665, 2010.

[75] J. Deng, C. Li, Z. Hu, Z. Wu, and L. Li. Spray characteristics of biodiesel and diesel fuels under high injection pressure with a common rail system. SAE paper 2010-01-2268. 2010.

[76] A. L. Kastengren, C. F. Powell, K.-S. Im, Y.-J. Wang, and J. Wang. Measurement of biodiesel blend and conventional diesel spray structure using x-ray radiography. *Journal of Engineering for Gas Turbines and Power*, 131(6):062802, 2009.

[77] F. Payri, V. Bermudez, R. Payri, and F. J. Salvador. The influence of cavitation on the internal flow and the spray characteristics in diesel injection nozzles. *Fuels*, 83:419–431, 2008.

[78] S. H. Park, H. K. Suh, and C. S. Lee. Effect of cavitating flow on flow and fuel atomization characteristics of biodiesel and diesel fuels. *Energy & Fuels*, 22(1):605–613, 2008.

[79] Y. Zeng, Y. Ren, F. Shi, and R. Grover. In-cylinder air flow velocities. Personal communication, May 2011.

[80] S. Tavoularis. *Measurement in Fluid Mechanics*. Cambridge University Press, New York, 2005.

[81] I. E. Indelchik. *Handbook of Hydraulic Resistance: 3rd Edition*. Begell House, New York, 2001.

[82] T. Morel. Comprehensive design of axisymmetric wind tunnel contractions. *J. Fluids Eng.*, 97, 1975.

[83] E. G. Tulapurkara and V. V. K. Balla. Experimental investigation of morel's method for wind tunnel contractions. *J. Fluids Eng.*, 110, 1988.

[84] P. Bradshaw and R. C. Pankhurst. The design of low-speed wind tunnels. *Progress in aeronautical sciences*, 5, 1964.

[85] J. H. W. Lee and V. H. Chu. *Turbulent Jets and Plumes - A Lagrangian Approach*. Kluwer Academic, Massachusetts, 2003.

[86] G. N. Abramovich. *The Theory of Turbulent Jets*. MIT Press, Cambridge, MA, 1963.

[87] S. Ashforth-Frost and K. Jambunathan. Effect of nozzle geometry and semi-confinement on the potential core of a turbulent axisymmetric free jet. 23:155–162, 1996.

[88] R. C. Gonzalez, R. E. Woods, and S. L. Eddins. *Digital Image Processing using MATLAB*. Pearson Prentice Hall, Upper Saddle River, NJ, 2004.

[89] B. Ganapathisubramani, E. K. Longmire, I. Marusic, and S. Pothos. Dual-plane PIV technique to determine the complete velocity gradient tensor in a turbulent boundary layer. *Experiments in Fluids*, 39:222–231, 2005.

[90] S. Funatani, N. Fujisawa, and H. Ikeda. Simultaneous measurement of temperature and velocity with with colour CCD camera and its application to the turbulent buoyant plume. *Measurement Science and Technology*, 15:983–990, 2004.

[91] T. D. Nguyen, J. Pelle, and S. Harmand. PIV measurements of an air jet impinging on and open rotor-stator system. *Experiments in Fluids*, 53:401–412, 2012.

[92] T. van Hooff, B. Blocken, T. Defraeye, J. Carmeliet, and G. J. F. van Heijst. PIV measurements of a plane wall jet in a confied space at transitional slot reynolds numbers. *Experiments in Fluids*, 53:499–517, 2012.

[93] G. Cao, M. Sivukari, J. Kurnitski, and M. Ruponen. PIV measurement of the attached plane jet velocity field at a high turbulence intensity level in a room. *International Journal of Heat and Fluid Flow*, 31:897–908, 2010.

[94] S. Gogineni, L. Goss, and M. Roquemore. Manipulation of a jet in a cross flow. *Experimental Thermal and Fluid Science*, 16:209–219, 2010.

[95] A. Pereira. Investigation of direct injection fuel sprays in high velocity air flows. Master's thesis, University of Waterloo, 2013 (In Progress).

[96] N. A. Fuchs. *The mechanics of aerosols*. Dover Publications, New York, 1989.

[97] J. R. Harris. Investigation of relative importance of some error sources in particle image velocimetry. Master's thesis, Utah State University, 2012.

[98] A. J. Yule and S. M. Aval. Cyclic vartions of diesel sprays. *Fuel*, 68:1558–1564, 1989.

[99] A. de Risi, F. Naccarato, and D. Laforgia. Experimental analysis of common rail pressure wave effect on engine emissions. SAE Paper 2005-01-0373,. 2005.

[100] Rothsay Biodiesel, 605 1ere Avenue, Ville Ste-Catharine, QC, Canada. *Rothsay Biodiesel Certificate of Analysis*, 2012.

[101] M. J. Anderson and P. J. Whitcomb. *DOE Simplified: Practical Tools for Effective Experimentation*. Productivity Press, New York, second edition, 2007.

[102] R.J. Adrian and J. Westerweel. *Particle Image Velocimetry*. Cambridge University Press, New York, NY, 2011.

[103] A. K. Prasad. Stereoscopic particle image velocity. *Experiments in Fluids*, 29:103–116, 2000.

[104] J. Canny. A computational approach to edge detection. *IEEE Transactions on Pattern Analysis and Machine Intelligence*, PAMI-8(6):679–698.